IMPERIAL

Reconfigurable Intelligent Surfaces:
Beamforming, Modulation, and Channel Shaping

Yang Zhao

Supervisor: Prof. Bruno Clerckx

Department of Electrical and Electronic Engineering

Imperial College London

This dissertation is submitted for the degree of
Doctor of Philosophy

Declaration

The contents presented in this dissertation are original and have been carried out by myself under the guidance of my supervisor Prof. Bruno Clerckx. Any work from other researchers, scholars, or sources have been properly cited and acknowledged. Figures, tables, and results presented in this dissertation are generated by myself, unless otherwise stated. I would like to acknowledge the use of large language models for assistance in improving the clarity and readability of introduction and background sections of this thesis. The contents have not been submitted in whole or in part for consideration of any other degree or qualification in any academic institution. I am aware of the ethical standards and academic integrity policies of Imperial College London, and I have adhered to these principles throughout the course of study. In signing this declaration, I affirm my commitment to academic honesty, intellectual integrity, and the pursuit of knowledge in the service of truth and understanding.

Any comments, suggestions, or corrections are greatly acknowledged and can be sent to `i@snowztail.com`. The source code of all simulation results in this dissertation are publicly available at `https://github.com/snowztail/`. Finally, I would like to appreciate Bruno, my colleagues, and whoever is reading this dissertation.

Yang Zhao

March 2024

Abstract

Reconfigurable Intelligent Surface (RIS) is the most promising physical-layer technology for 6G. It adopts many low-power scattering elements to customize the propagation environment for improved network performance, unlocking a new potential of *channel design* as never before. In this dissertation, we first provide an overview of its structure, characteristics, applications, principles, and models, then discuss how it addresses the key issues in Simultaneous Wireless Information and Power Transfer (SWIPT) and compare it with Backscatter Communication (BackCom) in terms of functionalities, principles, models, and preferences. The work chapters investigate three typical use cases of RIS: Joint design with transceiver for a particular objective (beamforming); ride its own information over legacy networks (modulation); and manipulate the wireless environment as a stand-alone device (channel shaping). In particular, we address the following topics:

- *RIS-aided SWIPT:* We introduce RIS into multi-antenna, multi-carrier SWIPT systems, investigating joint waveform and beamforming design for maximizing harvested energy under various communication rate constraints. Algorithms, performance trade-offs, and asymptotic behaviors are analyzed.

- *RIScatter:* This novel scatter protocol integrates RIS and BackCom from an input distribution perspective. The reflection pattern is exploited simultaneously for primary-link beamforming and backscatter-link modulation. We propose a practical cooperative receiver, characterize the achievable rate region, and analyze the impact of system parameters.

- *Multiple-Input Multiple-Output (MIMO) channel shaping:* We exploit an advanced Beyond-Diagonal (BD)-RIS architecture for singular value redistribution and power maximization in Point-to-point Channel (PC), and leakage interference minimization in Interference Channel (IC). Their implications on rate-optimal joint designs are also discussed. We highlight the unique features of BD-RIS and propose an efficient design framework.

Table of contents

List of figures

List of tables

Abbreviations

bpcu	bits per channel use
bps/Hz	bits per second per Hertz
AF	Amplify-and-Forward
AI	Artificial Intelligence
AM	Arithmetic Mean
AmBC	Ambient Backscatter Communication
AO	Alternating Optimization
AP	Access Point
AWGN	Additive White Gaussian Noise
BackCom	Backscatter Communication
BBC	Bistatic Backscatter Communication
BCD	Block Coordinate Descent
BD	Beyond-Diagonal
BER	Bit Error Rate
BIBO	Binary-Input Binary-Output
BLE	Bluetooth Low Energy
BLS	Backtracking Line Search
CLT	Central Limit Theorem
CP	Canonical Polyadic
CR	Cognitive Radio
CSCG	Circularly Symmetric Complex Gaussian
CSI	Channel State Information
CSIT	Channel State Information at the Transmitter
CSS	Chirp Spread Spectrum
CW	Continuous Waveform

DC	Direct Current
DCMC	Discrete-input Continuous-output Memoryless Channel
DF	Decode-and-Forward
DMC	Discrete Memoryless Channel
DMMAC	Discrete Memoryless Multiple Access Channel
DMTC	Discrete Memoryless Thresholding Channel
DoF	Degree of Freedom
DP	Dynamic Programming
DSSS	Direct-Sequence Spread Spectrum
EIRP	Effective Isotropic Radiated Power
eMBB	enhanced Mobile Broadband
FDMA	Frequency-Division Multiple Access
FPGA	Field-Programmable Gate Array
FS	Frequency-Selective
FSK	Frequency-Shift Keying
FSSS	Frequency-Hopping Spread Spectrum
GM	Geomtric Mean
GP	Geometric Programming
i.i.d.	independent and identically distributed
IC	Interference Channel
IM	Index Modulation
IoE	Internet of Everything
IoT	Internet of Things
KKT	Karush-Kuhn-Tucker
LC	Low-Complexity
LEH	Linear Energy Harvester
LoRa	Long Range
LoRaWAN	Long Range Wide Area Network
LoS	Line-of-Sight

M2M   Machine-to-Machine
MAC   Multiple Access Channel
MBC   Monostatic Backscatter Communication
MC   Multiplication Coding
MIMO   Multiple-Input Multiple-Output
MISO   Multiple-Input Single-Output
ML   Maximum-Likelihood
MMSE   Minimum Mean-Square-Error
mMTC   massive Machine-Type Communication
MRC   Maximal Ratio Combining
MRT   Maximum Ratio Transmission
MSE   Mean-Square Error

NLoS   Non-Line-of-Sight
NOMA   Non-Orthogonal Multiple Access
NRZ   Non-Return-to-Zero

OFDM   Orthogonal Frequency-Division Multiplexing

PAE   Power-Added Efficiency
PAPR   Peak-to-Average Power Ratio
PC   Point-to-point Channel
PDF   Probability Density Function
PGA   Projected Gradient Ascent
PIN   Positive Intrinsic Negative
PS   Power Splitting
PSK   Phase Shift Keying

QAM   Quadrature Amplitude Modulation
QoS   Quality of Service

R-E   Rate-Energy
RCG   Riemannian Conjugate Gradient
RF   Radio-Frequency
RFID   Radio-Frequency Identification

| RIS | Reconfigurable Intelligent Surface |
| RZ | Return-to-Zero |

SC	Superposition Coding
SCA	Successive Convex Approximation
SDMA	Space-Division Multiple Access
SDP	Semi-Definite Programming
SDR	Semi-Definite Relaxation
SIC	Successive Interference Cancellation
SIMO	Single-Input Multiple-Output
SINR	Signal-to-Interference-plus-Noise Ratio
SISO	Single-Input Single-Output
SMAWK	Shor-Moran-Aggarwal-Wilber-Klawe
SMF	Scaled Matched Filter
SNR	Signal-to-Noise Ratio
SR	Symbiotic Radio
STAR	Simultaneous Transmission and Reflection
SVD	Singular Value Decomposition
SWIPT	Simultaneous Wireless Information and Power Transfer

| TDMA | Time-Division Multiple Access |
| TS | Time Switching |

| UE | User Equipment |
| URLLC | Ultra-Reliable Low-Latency Communication |

WF	Water-Filling
WIT	Wireless Information Transfer
WPCN	Wireless Powered Communication Network
WPT	Wireless Power Transfer
WSN	Wireless Sensor Network
WSR	Weighted Sum-Rate

| ZF | Zero-Forcing |

Notation

Constants

e	Euler's number $\simeq 2.71828\ldots$
$\jmath$	Imaginary unit $= \sqrt{-1}$
π	Archimedes' constant $\simeq 3.14159\ldots$

Objects

a, A	Scalar
$\mathbf{a}$	Column vector
$\mathbf{A}$	Matrix
$\mathcal{A}$	Finite set
$\mathbf{0}$	All-zero matrix
$\mathbf{1}$	All-one matrix
$\mathbf{I}$	Identity matrix

Sets

$\mathbb{N}$	Natural numbers (excluding 0)
$\mathbb{R}$	Real numbers
$\mathbb{R}_+$	Real nonnegative numbers
$\mathbb{C}$	Complex numbers
$\mathbb{I}$	Probability domain $[0, 1]$
$\mathbb{H}_+^{n \times n}$	Positive semi-definite matrices of dimension $n \times n$
$\mathbb{U}^{n \times n}$	Unitary matrices of dimension $n \times n$

Operations

$(\cdot)^*$	Complex conjugate
$(\cdot)^\mathsf{T}$	Transpose
$(\cdot)^\mathsf{H}$	Hermitian (conjugate transpose)

$(\cdot)^{\dagger}$	Moore-Penrose inverse
$(\cdot)^{+}$	Ramp function $\max(0, \cdot)$
$|\cdot|$	Absolute value of a complex number
$\|\cdot\|$	Euclidean norm of a vector
$\|\cdot\|_{\mathrm{F}}$	Frobenius norm of a matrix
$\arg(\cdot)$	Argument of a complex number
$\mathrm{card}(\cdot)$	Cardinality of a finite set
$\log(\cdot)$	Natural logarithm of a real number
$\exp(\cdot)$	Exponential of a scalar or square matrix
$\mathrm{tr}(\cdot)$	Trace of a square matrix
$\det(\cdot)$	Determinant of a square matrix
$\mathrm{sv}(\cdot)$	Singular values sorted from largest to smallest
$\mathrm{diag}(\cdot)$	Constructs a square matrix with inputs on the main diagonal
$\mathrm{diag}^{-1}(\cdot)$	Retrieves the main diagonal of a square matrix
$\Re(\cdot)$	Retrieves the real part of a complex number
$\Im(\cdot)$	Retrieves the imaginary part of a complex number
$\mathbb{E}(\cdot)$	Expectation operator
$\mathbb{A}(\cdot)$	Extracts the Direct Current component of a signal
$\odot$	Hadamard product
$\otimes$	Kronecker product
$(\cdot)_{[x:y]}$	Shortcut for $(\cdot)_x, (\cdot)_{x+1}, \ldots, (\cdot)_y$

Distributions

$\sim$	Follows a distribution
$\mathcal{CN}(\mathbf{0}, \boldsymbol{\Sigma})$	Multivariate Circularly Symmetric Complex Gaussian with covariance $\boldsymbol{\Sigma}$

Subscripts

$(\cdot)_{\mathrm{D}}$	Direct
$(\cdot)_{\mathrm{F}}$	Forward
$(\cdot)_{\mathrm{B}}$	Backward
$(\cdot)_{\mathrm{I}}$	Information
$(\cdot)_{\mathrm{P}}$	Power
$(\cdot)_{\mathrm{T}}$	Transmit
$(\cdot)_{\mathrm{S}}$	Scatter
$(\cdot)_{\mathrm{R}}$	Receive

Superscripts

$(\cdot)^{(r)}$ r-th iterated value

$(\cdot)^{\star}$ Stationary point

Chapter 1

Introduction

1.1 Motivation

The quest for better wireless connectivity has been long-standing since Marconi's illuminating radio in 1895. Great successes have been made at the transmitter and receiver sides over the past century, and the communications society is unprecedentedly close to the Shannon limit [3]. By 2025, global mobile data traffic is expected to reach 607 exabytes per year [4] while the number of connected devices may exceed 75 billion [5]. At the same time, wireless applications are also evolving in various forms to address world-changing incidents like COVID-19, climate change, geopolitical tensions, and Artificial Intelligence (AI) revolution. An initial attempt was made in 5G where the network prioritizes among high-throughput, ubiquitous-coverage, high-reliability, low-latency, massive-connectivity, and energy-efficient services [6]. However, the desire of human and machine for better communication shows no signs of slowing down. Emerging applications such as smart cities, autonomous driving, telemedicine, extended reality, federated learning, and generative intelligence are calling for a stronger and smarter wireless infrastructure. It is envisioned that 6G will be designed to meet the following requirements [7–9]:

- *Throughput:* The network would be able to provide a peak data rate of 1 Tbps and an average data rate of 100 Gbps per user.

- *Latency:* Sub-millisecond end-to-end latency would be achieved for low-latency applications like autonomous driving and remote surgery.

- *Reliability:* A success rate of 99.9999% would be guaranteed for ultra-reliable applications like industrial automation and cooperative robotics.

- *Connectivity:* The number of connected devices per kilometer square would be increased to 10 million for supporting Internet of Everything (IoE).

- *Mobility:* Commercial airlines with a maximal velocity of 1000 km/h would be the target application scenario.

- *Energy efficiency:* Power consumption has been a major criticism for 5G. It is expected that energy per bit would be reduced by over 90% in 6G to reduce carbon footprints.

- *Positioning accuracy:* Thanks to THz base stations, a 3D positioning accuracy of centimeter level may be achieved for indoor and outdoor environments.

- *Coverage:* Poor coverage has been another bottleneck for 5G. A terrestrial-satellite-aerial integrated network would provide a ubiquitous and uniform coverage for urban, rural, and remote areas.

- *Security and privacy:* Physical-layer security can be improved with narrower beams at higher frequencies and destructive scattering at the environment. Privacy can be enhanced with federated learning and homomorphic encryption.

Beyond the statistical requirements above, the next-generation wireless network is desired to integrate human, machine, environment, and AI seamlessly for a harmonic ecosphere. This paradigm shift from *connectivity* to *intelligence* is fueled by the latest advances in machine learning (theory) and programmable metamaterials (hardware). The former enables the network to understand the environment while the latter evolves the environment from a chaotic medium to a conscious agent that can serve on demand. Together, they form a symbiotic relationship with the potential to revolutionize how the world energize, sense, communicate, and interact.

One promising candidate within this 6G vision is Reconfigurable Intelligent Surface (RIS), a programmable metasurface that recycles and redistributes the electromagnetic waves in the air for improved wireless performance. It could be incorporated into the transmitter and receiver for *beamforming*, employed as a free-rider information source for *modulation*, or simply placed in space as a standalone device for *channel shaping*. These applications have distinctive requirements and trade-offs, but the operation principles are the same and those roles are not mutually exclusive. Imagine a future where everything can be "smartened" by coating with a metamaterial layer and attaching a microcontroller tag. Only a few active radiating sources (like the sun) are needed, while most objects (like the universe) can exploit the surrounding waves to energize themselves, sense the environment, communicate with others, and help those in need when idle. This vision motivates three research questions to be addressed in this thesis:

- *How does RIS impact different wireless applications such as communication and far-field power transfer?*

- *Is it possible to integrate RIS with other scattering applications into a versatile tool that blurs the boundary between the network and environment?*

- *What is the ultimate limit of channel reshaping through passive RIS and what are the implications on transceiver designs?*

Before delving into these questions, we first provide a short overview of RIS and introduce some potential applications. A detailed literature review and technical discussion on RIS and other technologies will be reserved for Chapter 2.

1.2   Overview on Reconfigurable Intelligent Surface (RIS)

1.2.1   Concept

RIS is commonly known as a planar surface involving numerous wave scattering elements (a.k.a. unit cells, reflective patches), whose amplitude and phase responses can be engineered in real-time to achieve a desired radiation pattern. It behaves like a delicate Radio-Frequency (RF) mirror with adjustable curvature and orientation, which allows the incident signals to be focused and redirected in a particular direction. As shown in Fig. 1.1, its typical architecture consists of three stacked layers and a controller [1]. The top layer is a two-dimensional array of scattering elements printed on a dielectric substrate. The elements directly interact with the impinging waves, which are usually fabricated from metamaterial or patch/dipole antennas with sub-wavelength dimension and spacing. The middle layer is a copper ground plate that provides voltage reference and avoids signal leakage. The bottom later is a circuit board that associate each element with adjustable components, such as varactor and Positive Intrinsic Negative (PIN) diodes [10]. It also hosts a Field-Programmable Gate Array (FPGA) controller that controls the circuit and coordinate with transceivers in the network. By adjusting the scatter response of all elements, the RIS can effectively manipulate the wavefront for a constructive or destructive superposition and thus improve the ambient wireless environment.

1.2.2   Characteristics

The key characteristics of RIS are summarized as follows:
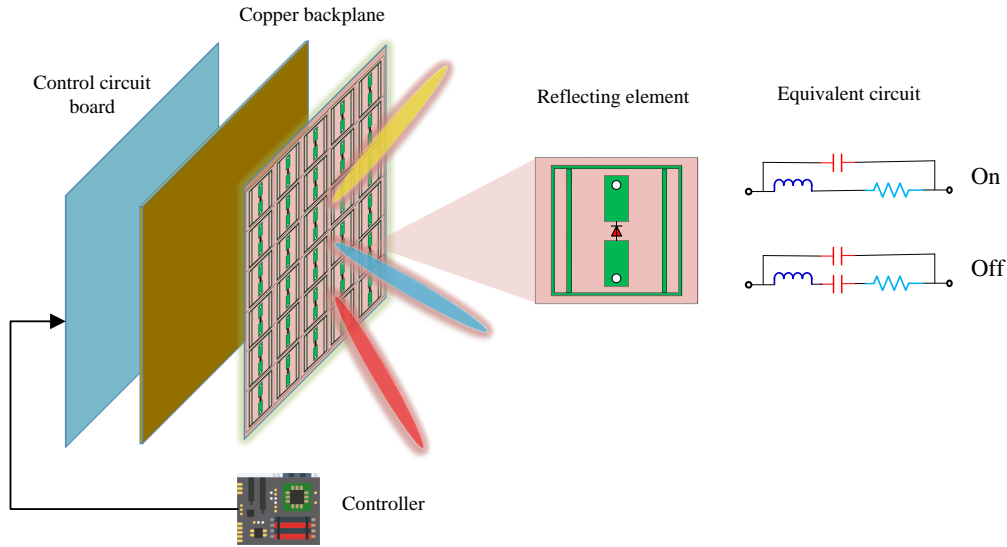
Fig. 1.1 A typical architecture of RIS. Source: Modified from [1].

- *Passive and environmental-friendly:* RIS reflects the incident waves in a passive manner and does not require dedicated RF chains.[1] This is different from Amplify-and-Forward (AF) relays that require power-hungry oscillators and introduces additional thermal noise.

- *Flexible:* It provides a software configurable environment that can be adapted for different applications and scenarios. This is different from conventional reflectarray [11] and frequency selective surfaces [12] with predefined radiation patterns and frequency response.

- *Full-duplex and universal:* This physical-layer solution can simultaneously support communication, sensing, and power transfer without self-interference. Thanks to channel reciprocity, the optimal configuration for downlink and uplink coincide with each other [13]. This is different from Decode-and-Forward (DF) relays that are designed for a specific communication link and suffers from packet delays.

- *Low-cost and conformal:* It can be manufactured from low-cost materials and deployed in various forms (e.g., walls, windows, ceilings, tables) to provide seamless coverage and powerful customization for indoor and outdoor environments. This is different from conventional multi-antenna systems that features complex hardware and bulky structures.

---

[1]The controller may be implemented with low-power components and powered by ambient energy.

1.2.3 Applications

The channel manipulation capability of RIS unlocks a wide range of unprecedented applications, such as signal enhancement [14], interference suppression [15], blockage bypassing [16], coverage extension [17], and security control [18]. It also has the potential to convey additional information [19], compensate for the Doppler effect [20], transform frequency-selective channels into frequency-flat [21], improve the spatial diversity for multi-antenna systems [22], and create artificial time diversity for multi-user orthogonal [23] and non-orthogonal [24] multiple accesses.

Those fancy characteristics and applications of RIS have also attracted significant attention from the industry. The first public testing attempt was made in 2018 by NTT Docomo and Metawave, which demonstrated a metasurface reflectarray in the FR2 band of 5G can boost a downlink data rate from $60\,\mathrm{Mbps}$ to $560\,\mathrm{Mbps}$ [25]. Later in 2020, NTT Docomo developed a transparent dynamic RIS that can allows 28GHz signals to reflect or pass through with negligible power loss. A regional "RIS alliance" was formed in 2021 by Chinese companies and institutes including ZTE, China Mobile, and CAICT, which soon released a white paper [26] to promote the technology and standardization. In December 2022, ITU-R drafted a recommendation report for IMT-2030 (6G) [27] that marks RIS as a key technology to enhance the radio interface for multiple physical dimension transmission. These developments showcase the rapid progress of RIS from theoretical concept to practical implementation, paving the way for its integration into the next-generation network.

1.3 Outline and Contributions

The thesis is outlined as follows:

- Chapter 1 provides an overview of the thesis. It introduces the motivation and objectives, raise critical research questions, discusses the characteristics and applications of RIS, and summarizes the contributions of each research chapter. A list of publications is also provided.

- Chapter 2 provides necessary background knowledge for RIS, Wireless Power Transfer (WPT), Simultaneous Wireless Information and Power Transfer (SWIPT), and Backscatter Communication (BackCom). It covers fundamental principles, hardware implementation, signal and system models, performance metrics, design challenges, and state-of-the-art research.

- Chapter 3 investigate the impact of RIS on wireless information and power transfer. The key contributions include:

  – Introduce RIS to a multi-antenna multi-carrier SWIPT system with different receiver architectures;

  – Consider joint waveform and beamforming design for the proposed system under a practical energy harvester model;

  – Characterize the Rate-Energy (R-E) performance trade-off by maximizing harvested energy subject to different communication rate constraints;

  – Propose local-optimal and low-complexity algorithms and evaluate their narrow and wideband performance through numerical simulations;

  – Discuss the array gain for communication and the scaling order for power transfer in terms of the number of transmit antennas and RIS elements.

- Chapter **??** develops a novel scatter protocol that integrates beamforming and modulation. The key contributions include:

  – Provide an in-depth comparison of RIS with state-of-the-art BackCom technologies and discuss the key properties of active and passive transmissions coexisting systems;

  – Unify RIS and BackCom as one battery-free cognitive radio called RIScatter, where dispersed or co-located scatter nodes ride over an active primary link to modulate their own information and engineering the legacy channel simultaneously;

  – Integrate backscatter modulation and passive beamforming seamlessly into the input distribution design that allows arbitrary trade-off in between;

  – Propose a low-complexity cooperative receiver that sequentially decodes both coexisting links and exploits backscatter detection as part of channel training;

  – Characterize the achievable primary-backscatter rate region over different designs of input distribution at the scatter nodes, active beamforming at the Access Point (AP), and energy detector at the receiver;

  – Discuss the impact of practical factors such as the number of scatter nodes and states, transmit antenna size, backscatter symbol duration, and Signal-to-Noise Ratio (SNR) on the system performance.

- Chapter **??** explores the ultimate channel shaping capabilities of RIS in Multiple-Input Multiple-Output (MIMO) systems. The key contributions include:

– Quantify the capability of a passive RIS to reshape the MIMO Point-to-point Channel (PC) in terms of singular values via analytical bounds and numerical optimization;

– Focus on a general Beyond-Diagonal (BD)-RIS architecture featuring element-wise connections and demonstrate its superior signal processing performance (subspace alignment and subchannel rearrangement) over the widely-adopted diagonal model;

– Propose an efficient Riemannian Conjugate Gradient (RCG) algorithm for general BD-RIS optimization and provide low-complexity solutions for quadratic problems;

– Characterize the Pareto frontiers of channel singular values and obtain power- and rate-optimal BD-RIS configurations in MIMO PC;

– Investigate the impact of BD-RIS on leakage interference suppression and Weighted Sum-Rate (WSR) maximization in MIMO Interference Channel (IC);

– Discuss how channel shaping helps to decouple joint RIS-transceiver designs with comparable performance and significantly reduced complexity.

1.4 Publications

- Y. Zhao, B. Clerckx, and Z. Feng, "IRS-aided SWIPT: Joint waveform, active and passive beamforming design under nonlinear harvester model," *IEEE Transactions on Communications*, vol. 70, pp. 1345–1359, 2022

- Y. Zhao and B. Clerckx, "Riscatter: Unifying backscatter communication and reconfigurable intelligent surface," 12 2022

- ——, *RIS in Wireless Information and Power Transfer*.   John Wiley & Sons, Ltd, 2023, pp. 271–295

- Y. Zhao, H. Li, M. Franceschetti, and B. Clerckx, "Channel shaping using reconfigurable intelligent surfaces: From diagonal to beyond," *To be submitted to IEEE Transactions on Wireless Communications*

Chapter 2

Background

This chapter provides essential background for topics covered in the thesis. A detailed literature review will be presented within each research chapter.

2.1 Reconfigurable Intelligent Surface (RIS)

2.1.1 Programmable Metamaterials

Metamaterials refer to artificial structures engineered for unusual properties that may not be found in nature. The concept was initially proposed by Victor Veselago in 1967, who conjectured the existence of mediums with negative dielectric constant $\epsilon < 0$ and negative permeability $\mu < 0$ [32]. Such metamaterials are known as "negative-index" because the refraction index is defined as the *negative* square root $n = -\sqrt{\epsilon\mu} < 0$, in order to be consistent with Maxwell's equations. It was not until 1999 that their feasibility was experimentally demonstrated by John Pendry at Imperial College using split-ring resonators [33]. Since then, metamaterials have attracted significant interests due to their counterintuitive properties, to name a few:

- *Negative refraction:* As shown in Fig. 2.1a, the incident and refracted rays stay at the same side of the normal axis [32]. This phenomenon is in contrast to the usual refraction but can still be predicted from Snell's law

$$\frac{\sin\theta_1}{\sin\theta_2} = n. \tag{2.1}$$

It is worth mentioning that a generalized law of refraction and refraction has been proposed in [34], which has become a standard reference for the design and analysis of metamaterials.

(a) Negative-index material   (b) Positive-index material
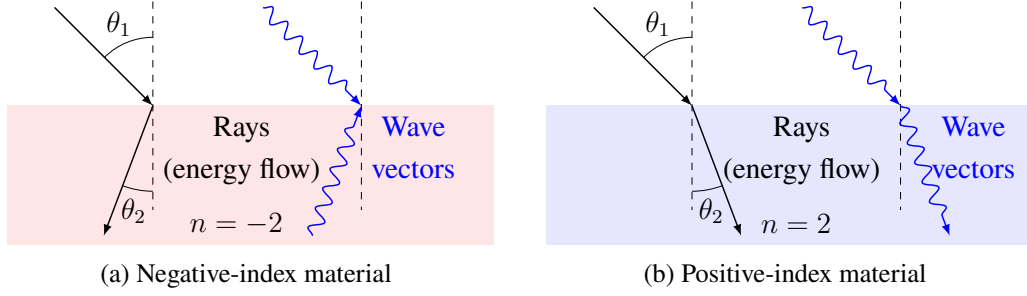
Fig. 2.1 Refraction in negative and positive-index materials. Incident and refracted rays stay at the same side of the normal axis in a negative-index material.

- *Opposite wave direction:* As shown in Fig. 2.2a, the wave vector and energy flow (indicated by the Poynting vector) are opposite to each other in a negative-index material [35]. This can be inferred from the electric field equation

$$\vec{E} = \vec{E}_0 \exp(\jmath k z - \jmath \omega t) \tag{2.2}$$

where $k = k_0 n < 0$ is the wavenumber, $\vec{E}_0$ and k_0 are the free-space electric field and wavenumber reference, z is the propagation distance, ω is the angular frequency, and t is the time. Negative-index materials are thus also called "left-hand" because the propagation direction of the electric and magnetic fields can be determined by a left-hand rule.

(a) Negative-index material   (b) Positive-index material
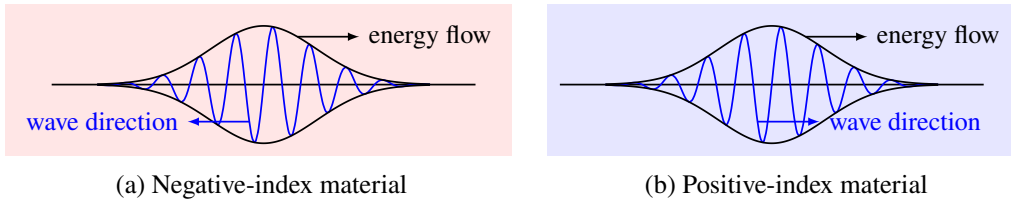
Fig. 2.2 Wave and energy have opposite directions in a negative-index material.

Conventional metamaterials have fixed properties that depend on the geometry and arrangement of their constituent elements. Once fabricated, these properties cannot be easily changed unless the structure is physically altered. This limits their early usage to military and defense, with applications such as invisibility cloaks and optical illusions. In 2014, the concept of "coding" and "programmable" metamaterials was validated by researchers at Southeast University [36], who realized digital control of radar cross-section using biased diodes and FPGA. With a proper model of the target properties and external citation, the

metamaterial can be reconfigured in real-time for desired behaviors. For example, a self-adaptive metasurface equipped with motion and light sensors have been developed in [37] for single- and multi-beam steering.

Next, we discuss the principles of electromagnetic wave redirection via refraction and reflection:

- *Refraction:* As shown in Fig. 2.3a, the negative-index material can re-focus the beams diverging from a point source to another point behind the material [38]. This could be helpful for wireless applications where the transmitter and receiver are at different sides of the material.

- *Reflection:* As shown in Fig. 2.4b, the scattering elements cooperatively alter the phase of the incident wave for a constructive (or destructive) superposition of the reflected waves in the target direction [39]. This could be helpful for wireless applications where the transmitter and receiver are at the same side of the material.

$n = -2/3$

$n = 2$

(a) Negative-index material

(b) Positive-index material
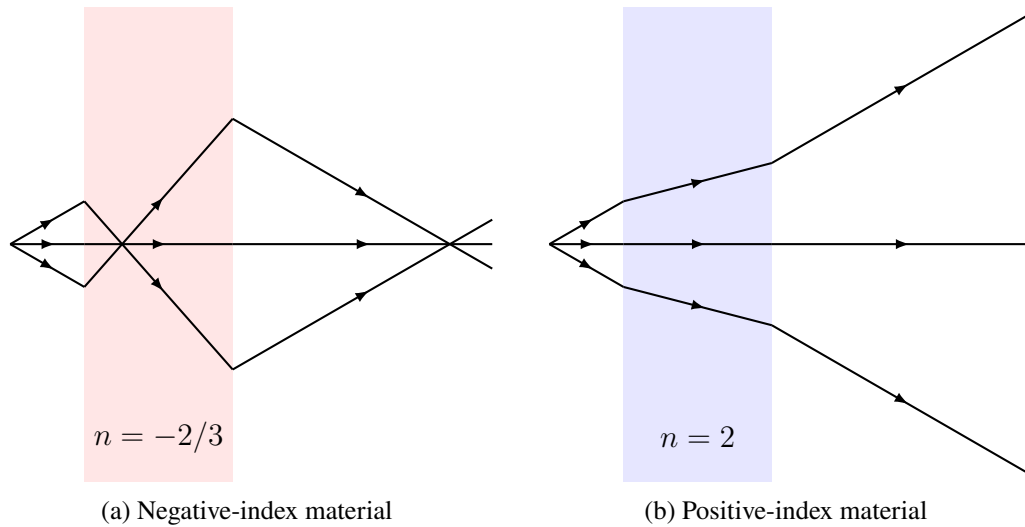
Fig. 2.3 Refraction through metamaterials. For negative-index material, beams diverging from a point source is set in reverse and converges back to another point.

(a) Incident wave   (b) Reflected wave
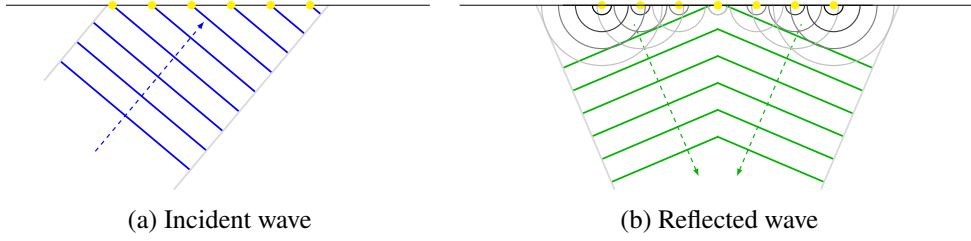
Fig. 2.4 Reflection through metamaterials. Yellow dots represent scattering elements. Solid and dashed lines denote wavefronts and rays, respectively. The scattering elements work together to manipulate the phases of incident waves, resulting in a focused beam steered in the intended direction.

It is worth noticing that refraction and reflection are different implementations of *passive beamforming* where the phase and amplitude of the ambient signal are altered by the metamaterial for a desired net effect. In the next subsection, we will some typical RIS scattering models and their physical architecture.

2.1.2 Wave Scattering Models

2.1.2.1 Principles

RF wave can be manipulated by scattering elements made from *programmable metamaterials* or *passive antennas* [40]. As discussed above, the former refracts or reflects the incident signals at the air-cell boundary and mainly applies a phase shift. In contrast, the latter allows the wave to feed into and collect from the antenna port such that some energy can be absorbed by the circuit and the rest is reradiated to the space. An interesting observation is that when excited by an external wave, a scattering element can simultaneously function as an object and a radiator. The corresponding scattered field is [41]

$$\vec{E}_{\text{scatter}}(Z_{\text{L}}) = \underbrace{\vec{E}_{\text{structural}}}_{\text{structural component}} + \underbrace{\Gamma I_{\text{M}} \vec{E}_{\text{antenna}}}_{\text{antenna component}}, \tag{2.3}$$

where Z_{L} is the load impedance, $\vec{E}_{\text{structural}}$ is the residual field under perfect matching (i.e., modelling as an object), $\vec{E}_{\text{antenna}}$ is the radiated field with unit current at the terminal and no external excitation (i.e., modelling as a radiator), I_{M} is the current under perfect matching, and Γ is the reflection coefficient

$$\Gamma = \frac{Z_{\text{L}} - Z_0^*}{Z_{\text{L}} + Z_0}, \tag{2.4}$$

and Z_0 is the characteristic impedance for programmable metamaterials or the input impedance for passive antennas. It is worth mentioning that

- *Structural component:* Depends on the geometry and material of the scatterer. It is usually modelled as part of the environment multipath [42, 43] or simply regarded a Direct Current (DC) offset when the impinging signal is Continuous Waveform (CW) [44].

- *Antenna component:* Depends on the reflection coefficient that can be altered by load impedance. This is widely exploited for various scattering applications, such as backscatter modulation in BackCom and passive beamforming in RIS [29].

We then introduce two canonical RIS models that will be adopted in the work chapters. More accurate models based on field equations (e.g., [45, 46]) and measurement fitting (e.g., [47]) are also available in the literature.

2.1.2.2 Diagonal Phase Shift Model

A straightforward way to model the RIS scattering effect is to consider independent scattering elements with purely reactive load impedance [48]. The reflection coefficient of the n-th element is thus

$$\theta_n = \frac{\jmath X_n - Z^*}{\jmath X_n + Z} = \exp(\jmath\phi_n), \tag{2.5}$$

where X_n is the reactance and ϕ_n is the phase shift on the scattered wave. For a total of N_{S} elements, the RIS scattering matrix is *diagonal with complex unit-magnitude entries*

$$\boldsymbol{\Theta} = \mathrm{diag}(\theta_1, \ldots, \theta_{N_{\mathrm{S}}}) = \begin{bmatrix} \theta_1 & 0 & \cdots & 0 \\ 0 & \theta_2 & \cdots & 0 \\ \vdots & \vdots & \ddots & \vdots \\ 0 & 0 & \cdots & \theta_{N_{\mathrm{S}}} \end{bmatrix}. \tag{2.6}$$

Despite the strong assumptions, this diagonal phase shift model is widely used for the analysis of RIS systems due to its simplicity and analytical tractability.

2.1.2.3 Beyond-Diagonal (BD) Model

How to model the RIS response if the passive scattering elements can be cooperative instead of independent? This question has been answered by [2] where a BD model was proposed. From a network theory perspective [49], the interaction between the scattering elements can be modelled as lossless (but not necessarily symmetric) in-group connections in an N_{S}-port

circuit network, as shown in Figs. 2.5 and 2.6 [2]. This architecture allows wave impinging on any element to propagate within the circuit and depart partially from other elements in the same group.
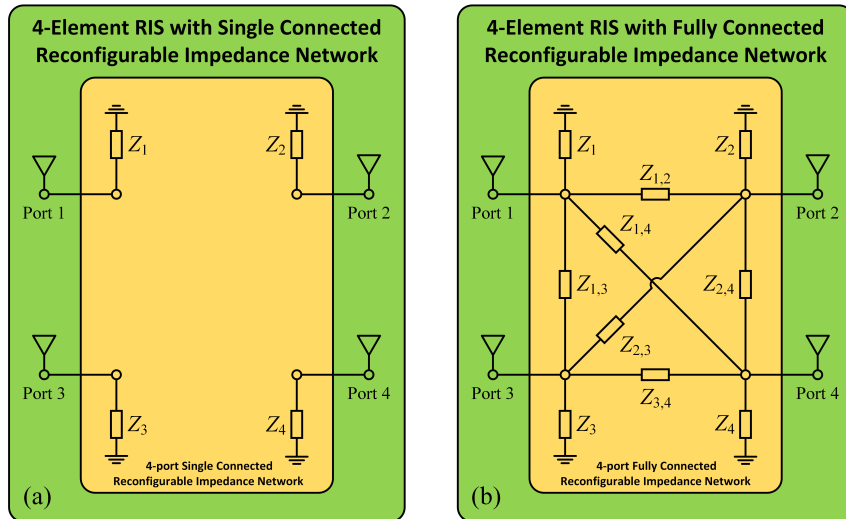
Fig. 2.5 Network model of a 4-element RIS with (a) independent scattering and (b) fully cooperative scattering with all elements interconnected. Source: Modified from [2].
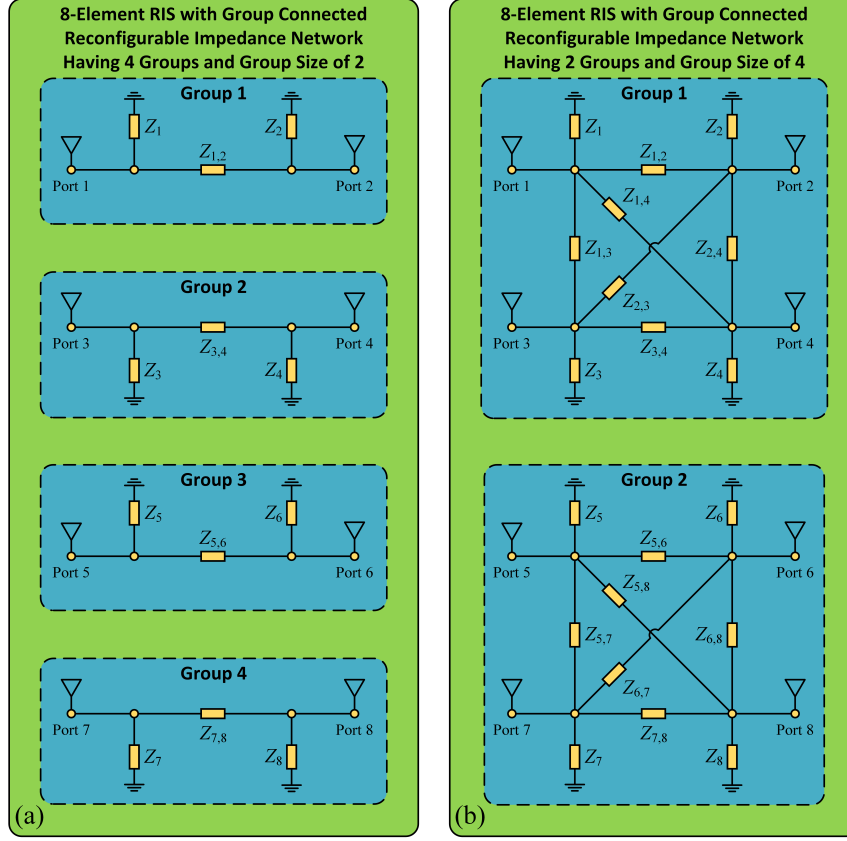
Fig. 2.6 Network model of an 8-element RIS with group-wise cooperative scattering of group size (a) 2 and (b) 4. The group size is a design parameter to balance the circuit complexity and scattering performance. Source: Modified from [2].

A general BD-RIS can be modeled as an N_S-port network that divides into G individual groups, each containing $L \triangleq N_S/G$ elements interconnected by real-time reconfigurable connections. With symmetric components (e.g., capacitors and inductors), the scattering matrix of group $g \in \mathcal{G} \triangleq \{1, \ldots, G\}$ is [2]

$$\mathbf{\Theta}_g = (\jmath\mathbf{X}_g + Z_0\mathbf{I})^{-1}(\jmath\mathbf{X}_g - Z_0\mathbf{I}), \tag{2.7}$$

which satisfies both *symmetric* and *unitary* properties

$$\mathbf{\Theta}_g = \mathbf{\Theta}_g^\mathsf{T}, \tag{2.8a}$$

$$\mathbf{\Theta}_g^\mathsf{H}\mathbf{\Theta}_g = \mathbf{I}. \tag{2.8b}$$

On the other hand, lossless networks may also be built over asymmetric passive components (e.g., ring hybrids and branch-line hybrids) [50] such that the symmetric constraint (2.8a)

can be relaxed. This corresponds to the ultimate passive model where energy conservation
(2.8b) is the only constraint for each group, as widely considered in quantum physics. The
overall scattering matrix of asymmetric BD-RIS is thus *block-diagonal with unitary blocks*

$$\boldsymbol{\Theta} = \mathrm{diag}(\boldsymbol{\Theta}_1, \ldots, \boldsymbol{\Theta}_G) = \begin{bmatrix} \boldsymbol{\Theta}_1 & \mathbf{0} & \cdots & \mathbf{0} \\ \mathbf{0} & \boldsymbol{\Theta}_2 & \cdots & \mathbf{0} \\ \vdots & \vdots & \ddots & \vdots \\ \mathbf{0} & \mathbf{0} & \cdots & \boldsymbol{\Theta}_G \end{bmatrix}, \tag{2.9}$$

where (2.8b) is equivalently denoted as $\boldsymbol{\Theta}_g \in \mathbb{U}^{L \times L}$. The group size L is a design parameter
to balance the circuit complexity and scattering performance. Diagonal (single-connected)
and unitary (fully-connected) RIS can be viewed as extreme cases with group size $L = 1$ and
$L = N_\mathrm{S}$, respectively. Therefore, the BD model (2.9) is envisioned to be the next-generation
theoretical foundation for passive RIS, which grants more design freedom and stronger signal
processing capability.

It is also worth mentioning that each group can be abstracted as a mathematical graph
with L vertices and a variable number of edges [51]. One element is in the same group
with another if and only if there is at least one path (via edges) between them. It implies
that instead of connecting every pair of elements, the practical circuit can be designed to
have a sparse graph with only a few connections, which is beneficial for reducing the circuit
complexity and power loss from non-ideal components. Antenna directivity and radiation
pattern should also be modelled in the scattering matrix, especially when the locations of
users or RIS are not fixed. This has motivated the concept of Simultaneous Transmission and
Reflection (STAR)-RIS [52, 53] and multi-sector RIS [54] where incident wave is partially
steered to various directions for different users.

2.2 Wireless Power Transfer (WPT)

2.2.1 Introduction

Wireless devices are becoming smarter as well as more energy-efficient and eco-friendly.
Koomey's law [55] predicts the computing efficiency roughly doubles every 19 months and
the amount of power needed for the same operation decreases to 1% in a decade. Over the
past 15 years, the rise of low-power technologies like Wireless Sensor Network (WSN) and
Internet of Things (IoT) have hatched life-changing applications including smart homes,
digital healthcare, and industrial automation. Today, Radio-Frequency Identification (RFID)
tags and basic sensors (e.g., thermometer and proximeter) can operate on microwatts of power

[56, 57], while communication protocols like Bluetooth Low Energy (BLE) and Long Range Wide Area Network (LoRaWAN) only consume tens of milliwatts [58]. This low-power trend together with the upsurge of mobile devices is calling for a *truly wireless* energy solution that eliminates the need for periodic cable plugging or battery replacement. While great successes have been witnessed for candidates like solar and piezoelectric, their prospects in wireless systems remain unclear due to the bulky converter, unpredictable source, and limited operation range. One promising solution on the horizon is WPT through electromagnetic waves. It can be classified into two categories based on the operation principle [59]:

- *Non-radiative near-field:* Power is transferred over a short distance (typically a few centimeters) by inductive coupling between coils or capacitive coupling between electrodes in a field-to-field manner. The former has been widely standardized (e.g., Qi 2.0) and commercialized (e.g., wireless charging pads), while the latter is still in the research stage.

- *Radiative far-field:* Power is transferred over a long distance (typically a few meters) by directional microwave or laser beams between antennas in a point-to-point manner. It shares many similarities with RF communication (e.g., infrastructure and wireless environment) but suffers from lower energy efficiency than non-radiative WPT due to pathloss.

Radiative WPT[1] brings numerous opportunities to future wireless networks. First, it completely eliminates wired connections and can be integrated into existing wireless systems with minimum modifications. Those properties translate to simple deployment, high scalability, and low maintenance cost. Second, the power can be simultaneously radiated to multiple devices on demand in a predictable, sustainable and reliable manner. This supports our initial vision and is different from other uncontrollable and intermittent energy sources. Third and most importantly, radio waves carries power and information simultaneously. WPT can therefore be jointly designed with Wireless Information Transfer (WIT) to make the most of radiation, spectrum and infrastructures. However, energy efficiency and safety concerns have been two major obstacles that limit the practical development of WPT. In Section 2.3, we will discuss how RIS can help address these issues.

---

[1]In the following part of the thesis, WPT refers to radiative WPT.

2.2.2   Modules and Coupling Effect
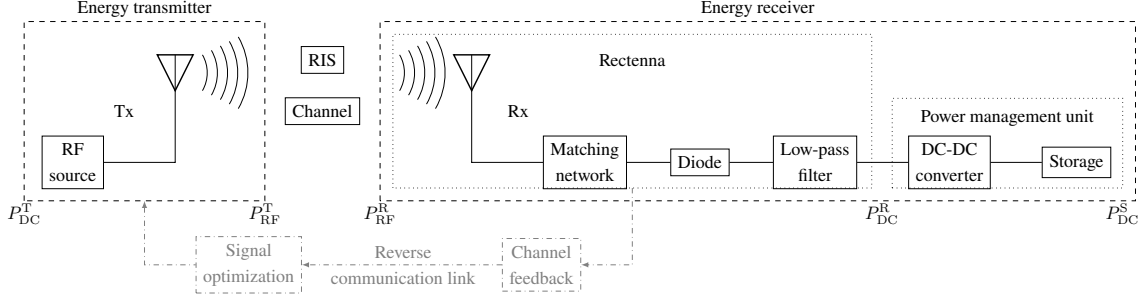
Fig. 2.7 Block diagram of a closed-loop RIS-aided WPT.

The block diagram a closed-loop RIS-aided WPT system is illustrated in Fig. 2.7. The RF signal is generated and radiated by the energy transmitter, propagated through a wireless channel in the presence of a RIS, captured by the antenna(s) at the receiver, converted to DC power by rectifier(s), then passed to the power management unit. Upon successful harvesting, the DC power is either delivered directly to the device or stored in a battery/super capacitor for future operations. When a feedback link is available, one can acquire Channel State Information (CSI) at the energy transmitter and exploit it for signal optimization. Such a closed-loop RIS-aided WPT system can provide a complete control of transmitter, channel, and receiver, which is essential for maximizing the end-to-end power transfer efficiency

$$\eta = \frac{P_{\mathrm{DC}}^{\mathrm{S}}}{P_{\mathrm{DC}}^{\mathrm{T}}} = \underbrace{\frac{P_{\mathrm{RF}}^{\mathrm{T}}}{P_{\mathrm{DC}}^{\mathrm{T}}}}_{\eta_1} \underbrace{\frac{P_{\mathrm{RF}}^{\mathrm{R}}}{P_{\mathrm{RF}}^{\mathrm{T}}}}_{\eta_2} \underbrace{\frac{P_{\mathrm{DC}}^{\mathrm{R}}}{P_{\mathrm{RF}}^{\mathrm{R}}}}_{\eta_3} \underbrace{\frac{P_{\mathrm{DC}}^{\mathrm{S}}}{P_{\mathrm{DC}}^{\mathrm{R}}}}_{\eta_4}, \tag{2.10}$$

where $P_{\mathrm{DC}}^{\mathrm{T}}$ is the transmitted DC power, $P_{\mathrm{RF}}^{\mathrm{T}}$ is the transmitted RF power, $P_{\mathrm{RF}}^{\mathrm{R}}$ is the received RF power, $P_{\mathrm{DC}}^{\mathrm{R}}$ is the received DC power, and $P_{\mathrm{DC}}^{\mathrm{S}}$ is the stored DC power. The power conversion efficiencies are specified below:

- η_1: Transmitter DC-to-RF conversion efficiency[2] that depends on the RF power amplifier and transmit antenna. It is also called "drain efficiency" and state-of-the-art designs can achieve $\eta_1 \geq 70\%$ [61].

- η_2: Channel RF-to-RF conversion efficiency that depends on the wireless environment and RIS configuration. This is the major bottleneck of WPT since the radiated power is inversely proportional to the propagation distance squared.

---

[2]This is different from Power-Added Efficiency (PAE) used in amplifier rating, which takes into account both DC power and input waveform power [60].

- η_3: Receiver RF-to-DC conversion efficiency that depends on the impedance matching and rectifier design. We will discuss its behavior and modelling in the next subsection.

- η_4: Storage DC-to-DC conversion efficiency that depends on the converter circuit and battery characteristics. Modern power management units can achieve a charging efficiency $\eta_4 \geq 90\%$ [62].

It is worth mentioning that η_1 and η_3 also depend on the characteristics of input waveform like power level, carrier frequency, and Peak-to-Average Power Ratio (PAPR) [63]. Extensive efforts have been contributed from RF, wireless communications, and power electronic communities to improve the conversion efficiency of individual modules. However, it is often overlooked in the literature that a practical WPT system is highly *non-linear* since the amplifier and rectifier are very sensitive to the input waveform. This non-linear behavior can lead to a *coupling effect* between the modules, such that optimizing η_1 to η_4 independently does not necessarily maximize the end-to-end power efficiency η [63]. Besides, the system modeling and analysis are subject to practical constraints like diode threshold and reverse-breakdown voltages, device parasitics, impedance mismatch, and harmonic generation [64].

2.2.3 Non-Linear Harvester Behavior

2.2.3.1 Equivalent Circuits

(a) Rectenna (b) Half-wave rectifier
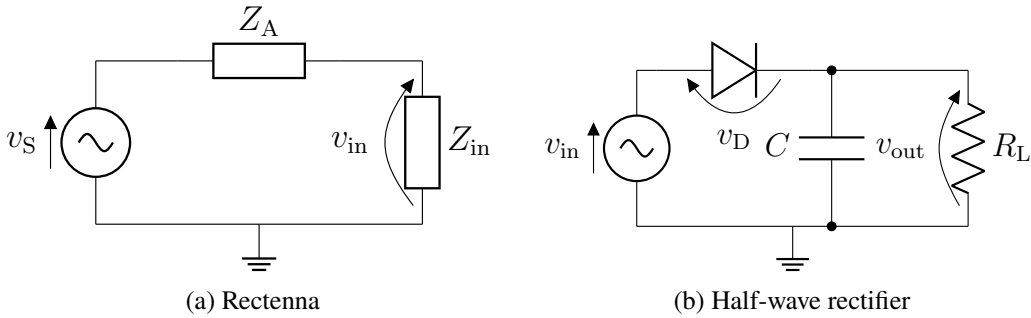
Fig. 2.8 Equivalent circuit of (a) rectenna and (b) single-diode half-wave rectifier.

The rectifier is a nonlinear circuit that converts the RF signal to DC power by rectifying and filtering the input signal. Figs. 2.8 illustrates the equivalent circuits of a rectenna (antenna and rectifier) and a single-diode half-wave rectifier, where v_S is the source voltage on the receive antenna, $Z_A = R_A + \jmath X_A$ is the antenna impedance, $Z_{in} = R_{in} + \jmath X_{in}$ is the total impedance of the matching network and rectifier, v_{in} is input voltage on the matching network and rectifier, v_D is the diode voltage, C is the buffer capacitance, R_L is the rectifier

load resistance, and v_{out} is the output voltage. It is worth mentioning that the half-wave rectifier is the most popular choice in WPT literature due to its simple behavior and low cost. Other rectifier topologies like full-wave, bridge, and voltage doubler can potentially improve the RF-to-DC conversion efficiency [65], but their modeling and analysis are much more complicated.

2.2.3.2 Operation Regions and Signal Models

The diode is the key non-linear component that determines to the harvested energy. Generally speaking, the behavior of any rectenna can be separated into three operation regions [63]:

- *Linear region:* When the input power level is relatively low, the output power is proportional to the input and the RF-to-DC conversion efficiency η_3 is a constant. Most early WPT research (especially from communications society) assume the rectenna works in this region. For a received signal $y(t)$, the harvested DC power in this region can be modelled as

$$P_{\text{DC}}^{\text{R}} = \eta_3 P_{\text{RF}}^{\text{R}} = \eta_3 \mathbb{A}\big\{|y(t)|^2\big\}, \tag{2.11}$$

  which suggests that maximizing the received RF signal power is sufficient to maximize the harvested DC power.

- *Non-linear (transition) region:* When the input power level is moderate, the output power increases *exponentially* with the input and η_3 is significantly higher than the linear region. This is the most interesting region that can be exploited to improve the overall power efficiency. For a tractable model, consider a perfectly matched ($Z_{\text{in}} = Z_{\text{A}}^*$) half-wave rectifier in Fig. 2.8(b) and assume the voltage across the matching network is negligible. The received RF power is totally transferred to the rectifier input $P_{\text{RF}}^{\text{R}} = \mathbb{E}\big\{|y(t)|^2\big\} = \mathbb{E}\big\{|v_{\text{in}}(t)|^2/R_{\text{in}}\big\} = \mathbb{E}\big\{|v_{\text{in}}(t)|^2/R_{\text{A}}\big\}$ such that the voltage sources can be expressed in terms of the received signal [63]

$$v_{\text{in}}(t) = y(t)\sqrt{R_{\text{A}}}, \quad v_{\text{S}}(t) = 2y(t)\sqrt{R_{\text{A}}}. \tag{2.12}$$

  The current passing through the diode is given by the characteristic equation $i_{\text{D}}(t) = I_{\text{S}}\big(\exp(v_{\text{D}}(t)/nv_{\text{T}}) - 1\big)$, where I_{S} is the reverse bias saturation current, v_{T} is the thermal voltage, and n is the ideality factor. Its Taylor expansion around the steady point $-v_{\text{out}}$ is [63]

$$i_{\text{D}}(t) = \sum_{i=0}^{\infty} k_i\big(v_{\text{D}}(t) + v_{\text{out}}\big)^i = \sum_{i=0}^{\infty} k_i v_{\text{in}}^i(t) = \sum_{i=0}^{\infty} k_i R_{\text{A}}^{i/2} y^i(t), \tag{2.13}$$

where $k_0 = I_S\big(\exp(-v_{\mathrm{out}}/nv_{\mathrm{T}}) - 1\big)$, $k_i = I_S \frac{\exp(-v_{\mathrm{out}}/nv_{\mathrm{T}})}{i!(nv_{\mathrm{T}})^i}$ for $k \in \mathbb{N}$. The rectifier output DC current can be written as a function of the received signal

$$i_{\mathrm{out}} = \sum_{i=0}^{\infty} k_i R_{\mathrm{A}}^{i/2} \mathbb{A}\big\{y^i(t)\big\} = \sum_{i=0,\mathrm{even}}^{\infty} k_i R_{\mathrm{A}}^{i/2} \mathbb{A}\big\{y^i(t)\big\} \qquad (2.14)$$

where the second equality is because $\mathbb{A}\big\{y^i(t)\big\} = 0$ for odd i. Note that the dependency of k_i on $-v_{\mathrm{out}} = -i_{\mathrm{out}} R_{\mathrm{L}}$ makes it nontrivial to formulate a closed-form expression for the harvested DC power. Fortunately, it is shown in [63] that maximizing the harvested DC power is equivalent to maximizing the quantity

$$z \triangleq \sum_{i=2,\mathrm{even}}^{n_0} \beta_i \mathbb{A}\big\{y^i(t)\big\}, \qquad (2.15)$$

where $\beta_i = I_S \frac{R_{\mathrm{A}}^{i/2}}{i!(nv_{\mathrm{T}})^i}$ is a constant and n_0 is the truncation order. Selecting $n_0 = 2$ yields the same result as (2.11), which suggests that the linear model is a special case of the more accurate non-linear model. For a moderate excitation, the contribution of higher-order terms is significant and should be modelled in the harvested DC power.

- *Saturation region:* When the input power level is too high, the diode works in the reverse breakdown region, the rectifier is saturated, and the output power is a constant. This is the region where the η_3 significantly drops and should be avoided by circuit design. For a fixed rectenna with Gaussian input signal, a parametric model was proposed in [66]

$$P_{\mathrm{DC}}^{\mathrm{R}} = \frac{\Psi_{\mathrm{DC}} - P_{\mathrm{sat}}\Omega}{1 - \Omega}, \quad \Psi_{\mathrm{DC}} = \frac{P_{\mathrm{sat}}}{1 + \exp\big(-a(P_{\mathrm{RF}}^{\mathrm{R}} - b)\big)}, \quad \Omega = \frac{1}{1 + \exp(ab)}, \qquad (2.16)$$

where the constant P_{sat} denotes the maximum harvested power when the rectifier is saturated, and the constants a and b model the nonlinear charging rate with respect to input power and the minimum turn-on voltage of the rectifier, respectively. Parameters P_{sat}, a, and b can be obtained by curve fitting over measurement results.

The exact boundaries between those regions depend on the rectifier circuit and input waveform [67]. Signals with a higher PAPR usually exhibit the nonlinear and saturation effects at lower input power levels. For example, the nonlinear region is typically $[-20, 0]$ dBm for a CW and $[-30, -10]$ dBm for a multisine [68]. This not only motivates adaptive multi-carrier waveform designs [63, 67, 69, 70] but also calls for a joint optimization of the transmitter, channel (via RIS), and receiver to improve the end-to-end power efficiency.

2.3 Simultaneous Wireless Information and Power Transfer (SWIPT)

2.3.1 Introduction

WIT and WPT have been treated separately over the past century and have made significant progress in their respective fields. Interestingly, electromagnetic waves carry information and energy simultaneously and the same signal can be used for communication and power transfer. The idea of SWIPT was first proposed in 2008 [71] and has since attracted significant attention from both academia and industry. It is a promising solution to connect and energize trillions of low-power mobile devices, providing power at microwatt level and coverage up to tens of meters in a unified manner [72]. SWIPT can also smoothly shift between the two extreme cases to fully exploit the RF spectrum and network infrastructure. It is envisioned that future network providers will be able to offer a complete wireless solution including data and power services, which is essential for the upcoming intelligent era.

One of the most important issues in SWIPT is that the energy harvester requires a much higher received signal power (several orders of magnitude) than the information decoder [73]. Since the channel RF-to-RF efficiency η_2 is the primary constraint on the overall power efficiency, how to combat the pathloss and fading effects has been recognized as a crucial research topic for WPT SWIPT. Fortunately, this issue can be effectively mitigated by introducing a RIS to the environment. By carefully tuning the scatter response of the RIS elements, one can potentially achieve the following benefits:

- *Energy focusing:* The scattered waves can be steered towards the receivers or focused on a dedicated "hotspot zone" to increase the harvester input power level. This is also helpful to extend the coverage and improve the reliability of the energy link.

- *Beam splitting:* Instead of transmitting one strong beam towards each user, the energy signal can be split into multiple weaker beams rerouted by the RIS to even out the spatial power distribution. This is useful to bypass physical obstacles (especially in high-frequency and large-scale networks) and reduce the health risk of radiation.

RIS can also be used to assist the information link by SNR enhancement and interference suppression, as mentioned in subsection 1.2.3.

2.3.2   Rate-Energy (R-E) Tradeoff

Despite WIT and WPT share many similarities, their difference in design objectives, system architectures, and practical constraints make a joint implementation of SWIPT particularly challenging. Some preference of WIT and WPT are inherently conflicting, for example:

- *Waveform and modulation:* Under an average power constraint, WIT favors Gaussian signaling with maximum entropy distribution [74] while WPT prefers deterministic (unmodulated) multisine with higher PAPR [75].

- *Channel:* In a MIMO scenario, WIT favors full-rank Non-Line-of-Sight (NLoS) with high spatial diversity while WPT prefers rank-deficient Line-of-Sight (LoS) with high spatial correlation [76].

- *Receiver:* The power sensitivity is usually in the range of -40 to -80 dBm for information receivers and -10 to -30 dBm for energy harvesters [77].

Those disparities translate to a fundamental trade-off between information and power transfer in SWIPT systems, which is often quantified by a *R-E region*.

$$\mathcal{C}_{\mathrm{R-E}}(P) \triangleq \left\{ (r, e) : 0 \leq r \leq \log(1 + \gamma),\ 0 \leq e \leq z \right\}, \tag{2.17}$$

where P is the average transmit power, γ is the SNR at the information decoder, and z defined in (2.15) is uniquely mapped to the harvested DC power. Each point in this region corresponds to a *rate-energy pair* achieved by a particular *resource allocation scheme*. It is worth mentioning that different transceive strategies (e.g., waveform and receiver design) can lead to totally different R-E regions (instead of different points in the same region), which motivates a joint optimization of the transmitter, channel, and receiver.

2.3.3   Modules and Operation Modes

2.3.3.1   Information and Energy Flows

In SWIPT, the information and energy are always transmitted from the same source while their receivers can be either co-located or separated, as shown in Figs. 2.9(a) and 2.9(b). This is different from BackCom where the energy is delivered in the downlink and the information is sent in the uplink, as shown in Figs. 2.9(c) and 2.9(d).

(a) SWIPT with co-located receiver

(b) SWIPT with separated receivers

(c) Monostatic backscatter

(d) Bistatic backscatter
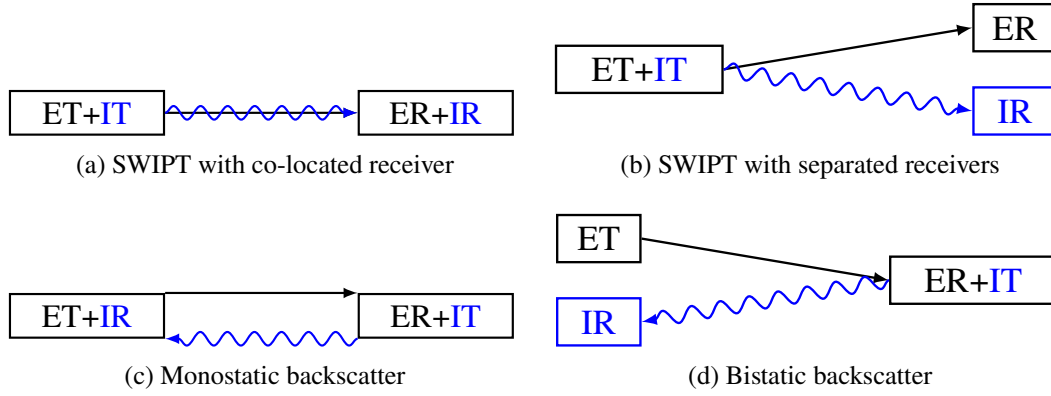
Fig. 2.9 Information and energy flows in SWIPT and BackCom systems. The blue and black parts denote information and power subsystems, respectively.

From a design perspective, co-located SWIPT receiver is a more general model since it can exploit the received signal for either purpose or a mixture in between. We thus focus on this model in the following context.

2.3.3.2 Receiver Architectures

Figure 2.10 illustrates four potential architectures for a co-located SWIPT receiver [78]:
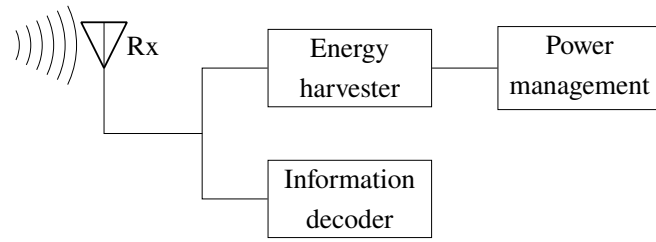
(a) Ideal receiver
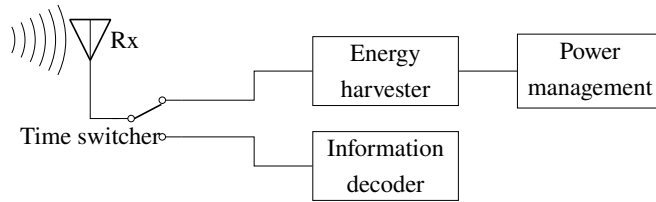
(b) Time switching receiver
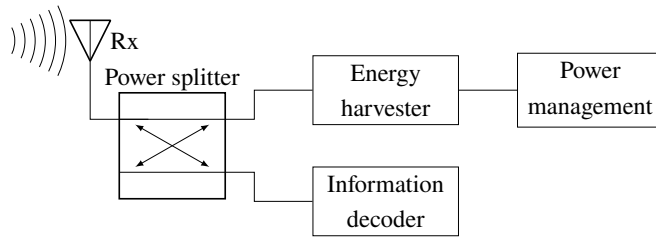
(c) Power splitting receiver
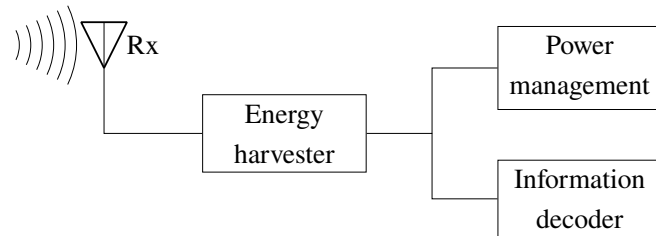
(d) Integrated receiver

Fig. 2.10 Architectures of a co-located SWIPT receiver.

- *Ideal receiver:* The received signal is used for both information decoding and energy harvesting. This is theoretically the most efficient design with a rectangle R-E region but is unimplementable in practice due to hardware constraints.

- *Time Switching (TS) receiver:* Each time block is divided into individual WIT and WPT phases, where the receiver switches between information decoder and energy harvester, respectively. The transmitted waveform and RIS response are optimized independently for each phase, and the resulting R-E region is a triangle with two vertices corresponding to WIT-only and WPT-only.

- *Power Splitting (PS) receiver:* The received signal is split into two parts with power ratio ρ and $1-\rho$. The former is fed into the energy harvester and the latter is used for information decoding. The transmitter and RIS are jointly optimized for both purposes with the knowledge of splitting ratio, and the resulting R-E region may be non-convex.

- *Integrated receiver [79]:* The transmit signal is modulated in properties that can be well-preserved after rectification (e.g., pulse position) such that information can be decoded from the energy harvester output.

The most popular architectures in the literature are TS and PS due to their practicality and tractability. The R-E region of the former can be inferred from that of the latter, since the WIT-only and WPT-only vertices in TS correspond to $\rho = 1$ and $\rho = 0$ in PS, respectively. Integrated receiver eliminates the need of RF chains and advanced architectures, but experiences information degradation and works better for low-throughput applications.

2.4   Backscatter Communication (BackCom)

2.4.1   Introduction

The scattered waves from any object inherently contain some information about the object. This contributed to the great success of radar in the World War II, where the "objective" information about the target (e.g., size, speed, and position) can be extracted from the reflected signal. Soon after the war in 1948, Stockman demonstrated the concept of BackCom where the target is no longer a dumb wave scatterer but part of the communication system that is willing to modulates its "subjective" information over the reflected signal [80]. The communication society quickly realized its potential to separate the power-hungry RF carrier emitter with the low-power information modulator, which is essential for miniaturizing wireless devices and increasing the network scale. As shown in Figs. 2.9(c) and 2.9(d) on Page 24, the backscatter node (a.k.a. tag) is activated by an energy signal (also functions as carrier) in the downlink and modulates over the scattered signal in the uplink. The energy transmitter (a.k.a. carrier emitter) and information receiver (a.k.a. reader) can be either co-located or separated, known respectively as monostatic and bistatic BackCom.

One of the most well-known BackCom applications is RFID which made its debut in the 1970s [81]. RFID readers sends a query signal and exploit the reflected signal from nodes (attached to objects) to identify and track them. The nodes can be powered wirelessly by the impinging wave and does not have to be in the vicinity of the reader. It has been standardized in ISO/IEC 18000 and EPC Gen2 [82] and widely used in supply chain management, access

control, and asset tracking. On the other hand, BackCom also plays an important role in emerging applications like IoT, WSN, and Machine-to-Machine (M2M) communications. Their main difference to RFID is that the message is no longer a static identifier but can be dynamically sensed from the environment or generated on demand. This enables a new paradigm of self-sustainable, intelligent, and pervasive sensing and communication, which is a key building block for our initial vision.

Nevertheless, low throughput and limited coverage are acknowledged as two critical problems for conventional BackCom systems. Those are inevitably inherited from the nature of wave scattering — the radiated signal has to travel a round trip (emitter-node-reader) with double pathloss, while the scatter response is frequency-dependent and usually results in a narrow bandwidth. Monostatic BackCom is also subject to a strong self-interference that further degrades the error performance and achievable rate. Finally, the nodes are idle most of the time and only respond when externally inquired. This is in sharp contrast to RIS where the elements are contributing for channel enhancement all the time. To mitigate those issues, multi-antenna techniques and special modulation schemes are two promising solutions in the literature. For example, a multi-antenna carrier emitter can perform energy beamforming [83], a multi-antenna node can perform energy combining with spatial modulation [84, 85] or space-time coding [86], and a multi-antenna reader can perform coherent [87, 88] or non-coherent [89] detection. We will discuss some popular modulation and coding techniques for BackCom in the following subsection.

2.4.2   Modulation and Coding Schemes

BackCom and RIS share the same wave scattering model in Section 2.1.2.1, but the reflection coefficient Γ in (2.4) is exploited in different manners. The difference is two-fold:

- *Modulation requires variation:* BackCom relies on dynamically changing the reflection coefficient over time to encode information. This is different from RIS where the optimal configuration (and reflection coefficient) is fixed for a given channel realization.

- *Harvesting requires absorption:* Part of the impinging wave should be fed into the node to power its operation. This is different from RIS where a full reflection is desired to maximize its channel control capability.

Denote the amplitude scattering ratio of the BackCom node as α, i.e., the power absorption ratio is $(1 - \alpha)^2$. Some popular modulation schemes are summarized below:

- *Quadrature Amplitude Modulation (QAM) [90]:* The reflection coefficient corresponding to the m-th symbol is

$$\Gamma_m = \alpha \frac{c_m}{\max_{m'} |c_{m'}|} \tag{2.18}$$

where c_m is the corresponding constellation point. This scheme is simple but exhibits a low detection SNR especially when the constellation size is large.

- *Frequency-Shift Keying (FSK) [82]:* For 2-FSK, the reflection coefficient is

$$\Gamma(t) = \begin{cases} \alpha, & t \in \left[\frac{n}{\Delta f}, \frac{2n+1}{2\Delta f}\right) \\ -\alpha, & t \in \left[\frac{2n+1}{2\Delta f}, \frac{n+1}{\Delta f}\right) \end{cases} = \frac{\pi}{4} \sum_{m=1,\text{odd}}^{\infty} \frac{\alpha}{m} \sin(2\pi m \Delta f t), \tag{2.19}$$

where $n \in \mathbb{N}$. If the incident wave is a CW at frequency f_0, the reflected signal is dominated by its first harmonic

$$s_1(t) = \frac{\alpha \pi}{2} \Big(\sin\big(2\pi(f_0 + \Delta f)t\big) - \sin\big(2\pi(f_0 - \Delta f)t\big) \Big). \tag{2.20}$$

That is, periodically switching the reflection coefficient at rate Δf results in a frequency shift $\pm \Delta f$ on the reflected signal. Practical implementations have been demonstrated on a variety of license-free protocols (e.g., HitchHike [91], Inter-Technology [92], Passive Wi-Fi [93], BLE-Backscatter [94]) where the mirror copy can be suppressed.

- *Chirp Spread Spectrum (CSS) [95]:* A chirp is a signal whose frequency increases or decreases over time. CSS uses wideband linear-frequency modulated chirps to encode information, which is from Direct-Sequence Spread Spectrum (DSSS) and Frequency-Hopping Spread Spectrum (FSSS) with pseudo-random sequences and FSK with discrete frequencies. In particular, $N + 1$ reflection coefficients of the same envelope are sequentially selected at a regular rate Δf, given by

$$\Gamma_n = \alpha \exp(\jmath \phi_n), \quad n \in \{0, 1, \ldots, N\}, \tag{2.21}$$

where $\phi_n = \frac{2\pi}{\Delta f}(An^2 + Bn)$ and A, B are constants. As the core modulation scheme in Long Range (LoRa), it is more robust to noise and interference (with a reception sensitivity of -149 dBm), harder to be detected by eavesdroppers, and can be used for ranging and localization [82].

Common BackCom channel coding schemes include unipolar Return-to-Zero (RZ) and Non-Return-to-Zero (NRZ), Manchester, differential, pulse-pause and FM0. They are not the focus of the thesis and the readers are referred to [96, Chapter 2.3] for details.
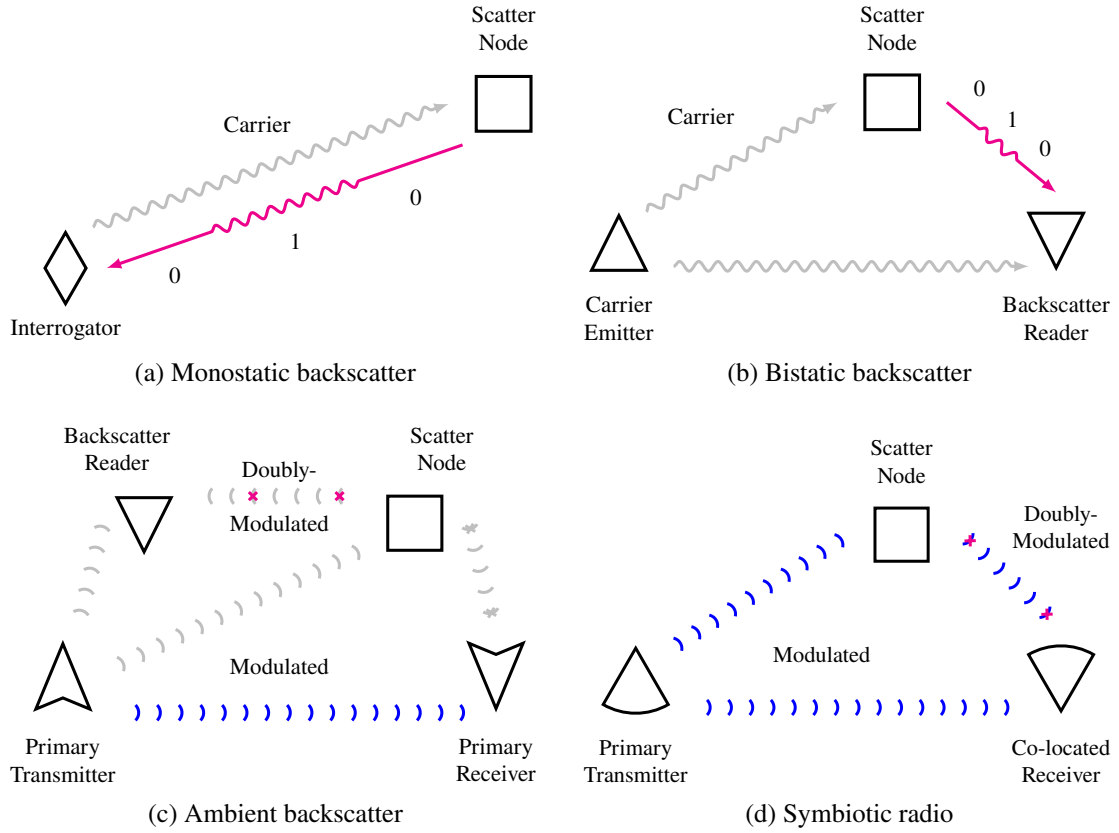
Fig. 2.11 Illustration of scattering applications. The blue flows denote the primary link while the magenta flows denote the backscatter link.

2.4.3 Applications

2.4.3.1 Monostatic Backscatter Communication (MBC)

Monostatic Backscatter Communication (MBC) is the most common architecture where the carrier emitter and reader are integrated into one device called interrogator. As shown in 2.9(c) and 2.11(a), the interrogator transmits a CW in the downlink and receives the reflected information-bearing signal in the uplink. The node varies its load impedance over time to switch between two states. Ideally, a full absorption (perfect matching, $\Gamma_0 = 0$) maps to bit "0" where energy is harvested, and a full reflection (perfect mismatch, $|\Gamma_1| = 1$) maps to bit "1" where SNR is determined. MBC is widely used in RFID systems. The integrated transceiver design reduces the hardware cost but suffers from strong self-interference and limited coverage.

2.4.3.2   Bistatic Backscatter Communication (BBC)

Bistatic Backscatter Communication (BBC) separates the carrier emitter and reader into two individual devices, as illustrated in 2.9(d) and 2.11(b). This helps to combat self-interference and extend the operation range, but the system involves three devices and requires more complex coordination and synchronization. It is more popular in more complicated scenarios like WSN and IoT with potentially moving nodes.

2.4.3.3   Ambient Backscatter Communication (AmBC)

Ambient Backscatter Communication (AmBC) has been recognized as a revolutionary technology since its debut in 2013 [97]. As shown in 2.11(c), it gets rid of dedicated RF sources and relies on ambient signals (e.g., TV, FM, and Wi-Fi) for both energy harvesting and information transfer. Compared with MBC and BBC, its carrier waveform is no longer a CW but a mixture of already modulated signals with different frequencies and amplitudes, which makes the detection more challenging. Therefore, it often employs FSK modulation to shift the scattered signals to a different band for reduced interference on both coexisting systems. AmBC is a plug-and-play and environmental-friendly IoT solution, but its practical deployment is limited by the availability and quality of ambient signals.

2.4.3.4   Symbiotic Radio (SR)

Symbiotic Radio (SR) is a relatively new concept proposed in 2019 that introduced itself as "cooperative AmBC" [98]. As shown in 2.11(d), it shares not only the transmitter, RF source, but also the receiver with a primary transmission. This is different from traditional AmBC where the legacy system can be unaware of the backscatter link and the node wants to minimize its footprint. Such a symbiotic interaction can improve the reliability of the backscatter link as well as the energy efficiency of the primary link, but unavoidably challenges the system design. For example, the acquisition of backscatter CSI can be difficult due to its passive characteristic, the detection of node message may involve complicated signal processing like Successive Interference Cancellation (SIC), and the synchronization of both links can be nontrivial due to the load-switching constraints. If those issues can be mitigated, SR would be a win-win solution that supercharges resource-constrained devices by leveraging the existing network infrastructure.

Chapter 3

RIS-Aided SWIPT: Joint Waveform and Beamforming Design

3.1 Introduction

3.1.1 Simultaneous Wireless Information and Power Transfer

With the great advance in communication performance, a bottleneck of wireless networks has come to energy supply. SWIPT is a promising solution to connect and power mobile devices via RF waves. It provides low power at milliwatt level but broad coverage up to hundreds of meters in a sustainable and controllable manner, bringing more opportunities to the IoT and M2M networks. The upsurge in wireless devices, together with the decrease of electronics power consumption, calls for a re-thinking of future wireless networks based on WPT and SWIPT [73].

The concept of SWIPT was first cast in [71], where the authors investigated the R-E trade-off for a flat Gaussian channel and typical discrete channels. [99] proposed two practical co-located information and power receivers, i.e., TS and PS. Dedicated information and energy beamforming were then investigated in [100, 101] to characterize the R-E region for multi-antenna broadcast and interference channels. On the other hand, [75] pointed out that the RF-to-DC conversion efficiency of rectifiers depends on the input power and waveform shape. It implies that the modeling of the energy harvester, particularly its nonlinearity, has a crucial impact on the waveform preference, resource allocation, and system design of any wireless-powered systems [75, 102, 73]. Motivated by this, [63] derived a tractable nonlinear harvester model based on the Taylor expansion of diode I-V characteristics, and performed joint waveform and beamforming design for WPT. Simulation and experiments showed the benefit of modeling energy harvester nonlinearity in real system design [103, 104]

and demonstrated the joint waveform and beamforming strategy as a key technique to expand the operation range [105]. A low-complexity adaptive waveform design by Scaled Matched Filter (SMF) was proposed in [106] to exploit the rectifier nonlinearity, whose advantage was then demonstrated in a prototype with channel acquisition [107]. Beyond WPT, [72] uniquely showed that the rectifier nonlinearity brings radical changes to SWIPT design, namely:

- Modulated and unmodulated waveforms are not equally suitable for wireless power delivery;

- A multi-carrier unmodulated waveform superposed to a multi-carrier modulated waveform can enlarge the R-E region;

- A combination of PS and TS is generally the best strategy;

- The optimal input distribution is not the conventional Circularly Symmetric Complex Gaussian (CSCG);

- Modeling rectifier nonlinearity is beneficial to system performance and essential to efficient SWIPT design.

Those observations, validated experimentally in [103], led to the question: *What is the optimal input distribution for SWIPT under nonlinearity?* This question was answered in [108] for single-carrier SWIPT, and some attempts were further made in [109] for multi-carrier SWIPT. The answers shed new light to the fundamental limits of SWIPT and practical signaling (e.g., modulation and waveform) strategies. It is now well understood from [72, 108, 109] that, due to harvester nonlinearity, a combination of CSCG and on-off keying in single-carrier setting and non-zero mean asymmetric inputs in multi-carrier setting lead to significantly larger R-E region compared to conventional CSCG. Recently, [110] used machine learning techniques to design SWIPT signaling under nonlinearity to complement the information-theoretic results of [108], and new modulation schemes were subsequently invented.

3.1.2   Reconfigurable Intelligent Surface

RIS has recently emerged as a promising technique that adapts the propagation environment to enhance the spectrum and energy efficiency. In practice, a RIS consists of multiple individual sub-wavelength reflecting elements to adjust the amplitude and phase of the incoming signal (i.e., passive beamforming). Different from the relay, backscatter and frequency-selective surface [12], the RIS assists the primary transmission using passive components with negligible thermal noise but is limited to frequency-dependent reflection.

Inspired by the development of real-time reconfigurable metamaterials [36], the authors of [111] introduced a programmable metasurface that steers or polarizes the electromagnetic wave at a specific frequency to mitigate signal attenuation. [48] proposed a RIS-assisted Multiple-Input Single-Output (MISO) system and jointly optimized the precoder at the AP and the phase shifts at the RIS to minimize the transmit power. The active and passive beamforming problem was then extended to the discrete phase shift case [112] and the multi-user case [14]. In [47], the authors investigated the impact of non-zero resistance on the reflection pattern and emphasized the coupling between reflection amplitude and phase shift in practice. To estimate the cascaded AP-RIS-User Equipment (UE) link without RF-chains at the RIS, practical protocols were developed based on element-wise on/off switching [113], training sequence and reflection pattern design [114, 115], and compressed sensing [116]. The hardware architecture, design challenges, and application opportunities of practical RIS were covered in [1]. In [10], a prototype RIS with 256 2-bit elements based on PIN diodes was developed to support real-time video transmission at gigahertz and mmWave frequency.

3.1.3   RIS-Aided SWIPT

By integrating RIS with SWIPT, the constructive reflection can boost the end-to-end power efficiency and improve the R-E trade-off. In multi-user cases, dedicated energy beams were proved unnecessary for the weighted sum-power maximization [117] but essential when fairness issue is considered [118]. It was also claimed that LoS links could boost the power efficiency since rank-deficient channels require fewer energy beams [119]. However, [117–119] were based on a linear energy harvester model that is known in both the RF and the communication literature to be inefficient and inaccurate [73, 75, 102, 63, 103–107, 72, 108–110]. Based on practical RIS and harvester models, [120] introduced a scalable resource allocation framework for a large-scale tile-based RIS-assisted SWIPT system, where the optimization consists of a reflection design stage and a joint reflection selection and precoder design stage. The proposed framework provides a flexible trade-off between performance and complexity. To the best of our knowledge, all existing papers considered resource allocation and beamforming design for dedicated information and energy users in a single-carrier network. In this chapter, we instead build our design based on a proper nonlinear harvester model that captures the dependency of the output DC power on both the power and shape of the input waveform, and marry the benefits of joint multi-carrier waveform and active beamforming optimization for SWIPT with the passive beamforming capability of RIS, to investigate the R-E trade-off for one SWIPT user with co-located information decoder and energy harvester. We ask ourselves the important question: *How to jointly exploit the spatial domain and the frequency domain efficiently through joint waveform and beamforming*

design to enlarge the R-E region of RIS-aided SWIPT? The contributions of this chapter are summarized as follows.

First, we propose a novel RIS-aided SWIPT architecture based on joint waveform, active and passive beamforming design under the diode nonlinear model (2.15) [63]. Although this tractable harvester model accurately reveals how the input power level and waveform shape influence the output DC power, it also introduces design challenges such as frequency coupling (i.e., components of different frequencies compensate and produce DC), waveform coupling (i.e., different waveforms jointly contribute to DC), and high-order objective function. To make an efficient use of the rectifier nonlinearity, we superpose a multi-carrier unmodulated power waveform (deterministic multisine) to a multi-carrier modulated information waveform and evaluate the performance under the TS and PS receiving modes. The proposed joint waveform, active and passive beamforming architecture exploits the rectifier nonlinearity, the channel selectivity, and a beamforming gain across frequency and spatial domains to enlarge the achievable R-E region. This is the first work to propose a joint waveform, active and passive beamforming architecture for RIS-aided SWIPT.

Second, we characterize each R-E boundary point by energy maximization under a rate constraint. The problem is solved by a Block Coordinate Descent (BCD) algorithm based on the Channel State Information at the Transmitter (CSIT). For active beamforming, we prove that the global optimal active information and power precoders coincide at Maximum Ratio Transmission (MRT) even with rectifier nonlinearity. For passive beamforming, we propose a Successive Convex Approximation (SCA) algorithm and retrieve the RIS phase shift by eigen decomposition with optimality proof. Finally, the superposed waveform and the splitting ratio are optimized by the Geometric Programming (GP) technique. The RIS phase shift, active precoder, and waveform amplitude are updated iteratively until convergence. This is the first work to jointly optimize waveform and active/passive beamforming in RIS-aided SWIPT.

Third, we introduce two closed-form adaptive waveform schemes to avoid the exponential complexity of the GP algorithm. To facilitate practical SWIPT implementation, the Water-Filling (WF) strategy for modulated waveform and the SMF strategy for multisine waveform are combined in time and power domains, respectively. The passive beamforming design is also adapted to accommodate the low-complexity waveform schemes. The proposed low-complexity BCD algorithm achieves a good balance between performance and complexity.

Fourth, we provide numerical results to evaluate the proposed algorithms. It is concluded that:

- RIS enables constructive reflection and flexible subchannel design in the frequency domain that is essential for SWIPT systems;

- RIS mainly affects the effective channel instead of the waveform design;

- Multisine waveform is beneficial to energy transfer especially when the number of subbands is large;

- TS is preferred at low SNR while PS is preferred at high SNR;

- There exist two optimal RIS development locations, one close to the AP and one close to the UE;

- The output SNR scales linearly with the number of transmit antennas and quadratically with the number of RIS elements;

- Due to the rectifier nonlinearity, the output DC scales quadratically with the number of transmit antennas and quartically with the number of RIS elements;

- For narrowband SWIPT, the optimal active and passive beamforming for any R-E point are also optimal for the whole R-E region;

- For broadband SWIPT, the optimal active and passive beamforming depend on specific R-E point and require adaptive designs;

- The proposed algorithms are robust to practical impairments such as inaccurate cascaded CSIT and finite RIS reflection states.

3.2   System Model
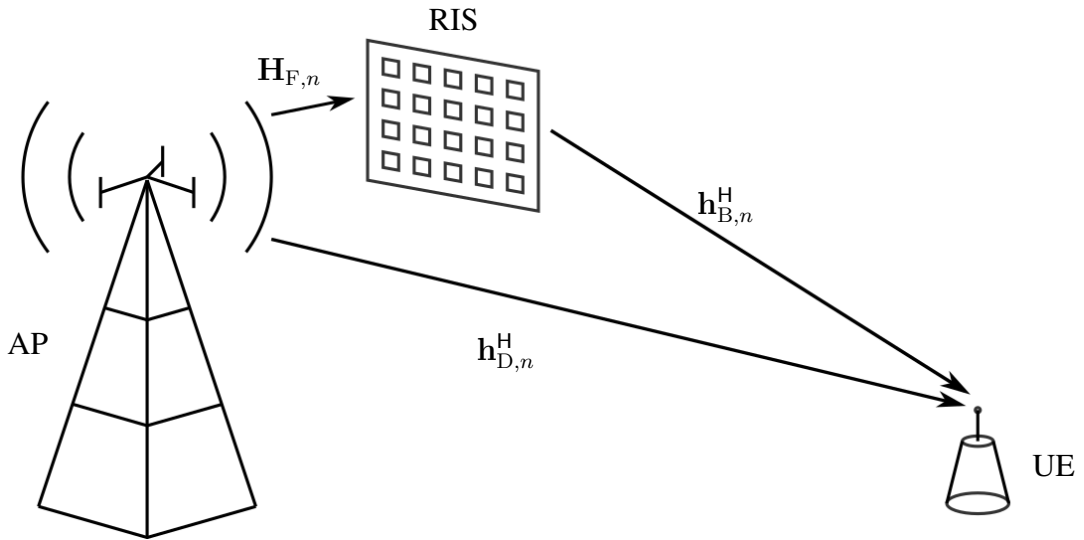
Fig. 3.1 An RIS-aided multi-carrier MISO SWIPT system.

As shown in Fig. 3.1, we propose a RIS-aided SWIPT system where an M-antenna AP delivers information and power simultaneously, through an L-element RIS, to a single-antenna UE over N orthogonal evenly-spaced subbands. We consider a quasi-static block fading model and assume the CSIT of direct and cascaded channels (defined in Section 3.2.2) can be acquired. The signals reflected by two or more times are omitted, and the noise power is assumed too small to be harvested. We assume that the time difference of signal arrival via direct and reflected paths is negligible compared to the symbol period.

3.2.1   Transmitted Signal

Following [72], we superpose a multi-carrier modulated information-bearing waveform to a multi-carrier unmodulated power-dedicated deterministic multisine to boost the spectrum and energy efficiency. The information signal transmitted over subband $n \in \mathcal{N} \triangleq \{1, \dots, N\}$ at time t is

$$\mathbf{x}_{\mathrm{I},n}(t) = \Re\left\{ \mathbf{w}_{\mathrm{I},n}\tilde{x}_{\mathrm{I},n}(t)e^{\jmath 2\pi f_n t} \right\}, \tag{3.1}$$

where $\mathbf{w}_{\mathrm{I},n} \in \mathbb{C}^{M\times 1}$ is the information precoder at subband n, $\tilde{x}_{\mathrm{I},n} \sim \mathcal{CN}(0,1)$ is the information symbol at subband n, and f_n is the frequency of subband n. On the other hand, the power signal transmitted over subband n at time t is

$$\mathbf{x}_{\mathrm{P},n}(t) = \Re\left\{ \mathbf{w}_{\mathrm{P},n}e^{\jmath 2\pi f_n t} \right\}, \tag{3.2}$$

where $\mathbf{w}_{\mathrm{P},n} \in \mathbb{C}^{M\times 1}$ is the power precoder at subband n. Therefore, the superposed signal transmitted over all subbands at time t is

$$\mathbf{x}(t) = \Re\left\{ \sum_{n=1}^{N}(\mathbf{w}_{\mathrm{I},n}\tilde{x}_{\mathrm{I},n}(t) + \mathbf{w}_{\mathrm{P},n})e^{\jmath 2\pi f_n t} \right\}. \tag{3.3}$$

We also define $\mathbf{w}_{\mathrm{I/P}} \triangleq [\mathbf{w}_{\mathrm{I/P},1}^{\mathsf{T}}, \dots, \mathbf{w}_{\mathrm{I/P},N}^{\mathsf{T}}]^{\mathsf{T}} \in \mathbb{C}^{MN\times 1}$.

3.2.2   Reflection Pattern and Composite Channel

As discussed in Section 2.1.2.1, RIS element $l \in \mathcal{L} \triangleq \{1, \dots, L\}$ varies its load impedance Z_l to manipulate the reflection coefficient θ_l (2.5). In the ideal scenario, this corresponds to a full reflection $|\theta_l| = 1$ with phase shift $\phi_l \in [0, 2\pi)$.

Remark 1. *Since the reactance X_l is a function of frequency, the reflection coefficient θ_l cannot be designed independently at different subbands. In this chapter, we assume the*

bandwidth is small compared to the operating frequency, such that the reflection coefficient at different subbands is approximately the same.

At subband n, we denote the AP-UE direct channel as $\mathbf{h}_{\mathrm{D},n}^{\mathsf{H}} \in \mathbb{C}^{1 \times M}$, the AP-RIS forward channel as $\mathbf{H}_{\mathrm{F},n} \in \mathbb{C}^{L \times M}$, and the RIS-UE backward channel as $\mathbf{h}_{\mathrm{B},n}^{\mathsf{H}} \in \mathbb{C}^{1 \times L}$. The auxiliary AP-RIS-UE link can be modeled as a concatenation of the backward channel, the RIS reflection, and the forward channel. Hence, the equivalent channel is given by

$$\mathbf{h}_n^{\mathsf{H}} = \mathbf{h}_{\mathrm{D},n}^{\mathsf{H}} + \mathbf{h}_{\mathrm{B},n}^{\mathsf{H}}\boldsymbol{\Theta}\mathbf{H}_{\mathrm{F},n} = \mathbf{h}_{\mathrm{D},n}^{\mathsf{H}} + \boldsymbol{\theta}^{\mathsf{H}}\mathbf{V}_n, \tag{3.4}$$

where $\boldsymbol{\theta} \triangleq [\theta_1, \ldots, \theta_L]^{\mathsf{H}} \in \mathbb{C}^{L \times 1}$ and $\mathbf{V}_n \triangleq \mathrm{diag}(\mathbf{h}_{\mathrm{B},n}^{\mathsf{H}})\mathbf{H}_{\mathrm{F},n} \in \mathbb{C}^{L \times M}$ is the cascaded RIS channel.

Remark 2. *The cascaded channel $\mathbf{V}_n$ varies at different subbands and there exists a trade-off for passive beamforming design in the frequency domain. Therefore, the equivalent subchannels should be carefully designed to meet specific requirements of multi-carrier SWIPT. For example, one can design the reflection pattern to either enhance the strongest subband (e.g., $\max_{\boldsymbol{\theta},n} \|\mathbf{h}_n\|$), or improve the fairness among subbands (e.g., $\max_{\boldsymbol{\theta}} \min_n \|\mathbf{h}_n\|$). That is to say, RIS enables a flexible subchannel design in multi-carrier transmissions. A similar effect also exists in the spatial domain for multi-antenna scenarios. In total, each reflection coefficient is indeed shared by M antennas over N subbands.*

3.2.3 Received Signal

The received superposed signal at the single-antenna UE is

$$y(t) = \Re\left\{\sum_{n=1}^{N}\left(\mathbf{h}_n^{\mathsf{H}}(\mathbf{w}_{\mathrm{I},n}\tilde{x}_{\mathrm{I},n}(t) + \mathbf{w}_{\mathrm{P},n}) + v_n(t)\right)e^{j2\pi f_n t}\right\}, \tag{3.5}$$

where $v_n(t)$ is the noise at RF band n. Please note that the modulated component can be used for energy harvesting if necessary, but the multisine component carries no information and cannot be used for information decoding.

3.2.4 Receiving Modes

Following the discussion in Section 2.3.3.2, we investigate the performance of TS and PS receivers in this work. The TS receiver divides each transmission block into orthogonal data and energy sessions with duration $1 - \eta$ and η, respectively. During each session, the transmitter optimizes the waveform for either WIT or WPT, while the receiver activates

the information decoder or the energy harvester correspondingly. The duration ratio η thus controls the R-E trade-off and is independent from the waveform and beamforming design. On the other hand, the PS receiver splits the incoming signal into individual data and energy streams with power ratio $1 - \rho$ and ρ, respectively. The data stream is fed into the information decoder while the energy stream is fed into the energy harvester. During each transmission block, the superposed waveform and splitting ratio are jointly designed to achieve different performance trade-offs. Since the R-E region of the TS receiver can be inferred from that of the PS receiver, we focus on the optimization with the PS receiver in the following context.

3.2.5 Information Decoder

A major benefit of the superposed waveform is that the multisine is deterministic and its impact on WIT can be completely eliminated by waveform cancellation or translated demodulation [72]. Therefore, the achievable rate is

$$R(\boldsymbol{\theta}, \mathbf{w}_{\mathrm{I}}, \rho) = \sum_{n=1}^{N} \log_2 \left(1 + \frac{(1 - \rho)|\mathbf{h}_n^{\mathsf{H}} \mathbf{w}_{\mathrm{I},n}|^2}{\sigma_n^2} \right), \tag{3.6}$$

where σ_n^2 is the variance of the total noise (at the RF-band and during the RF-to-baseband conversion) on tone n.

3.2.6 Energy Harvester

As discussed in Section 2.2.3.2, the output DC power of the energy harvester is a nonlinear function of the input power and waveform shape. When the diode is forward-biased and unsaturated, a truncated Taylor expansion of the diode I-V characteristic equation suggests that maximizing the average output DC is equivalent to maximizing a monotonic function [72]

$$z(\boldsymbol{\theta}, \mathbf{w}_{\mathrm{I}}, \mathbf{w}_{\mathrm{P}}, \rho) = \sum_{i=2,\mathrm{even}}^{n_0} \beta_i \rho^{i/2} \mathbb{E} \left\{ \mathbb{A} \left\{ y^i(t) \right\} \right\}, \tag{3.7}$$

which is slightly different from (2.15) in that (i) only a power ratio ρ of the received signal is used for energy harvesting and (ii) part of the received waveform is modulated such that expectation has to be taken. With a slight abuse of notation, we refer to z as the average output DC in this chapter. It can be observed that the conventional linear harvester model, where the output DC power equals the sum of the power harvested on each frequency, is a special case of (3.7) with $n_0 = 2$. However, due to the coupling effect among different frequencies, some high-order frequency components compensate each other in frequency

and further contribute to the output DC power. In other words, even-order terms with $i \geq 4$ account for the nonlinear diode behavior. For simplicity, we choose $n_0 = 4$ to investigate the fundamental rectifier nonlinearity. The average output DC power is then

$$
z(\boldsymbol{\theta}, \mathbf{w}_\text{I}, \mathbf{w}_\text{P}, \rho) = \beta_2 \rho \Big(\mathbb{E}\left\{ \mathbb{A}\left\{ y_\text{I}^2(t) \right\} \right\} + \mathbb{A}\left\{ y_\text{P}^2(t) \right\} \Big)
$$
$$
+ \beta_4 \rho^2 \Big(\mathbb{E}\left\{ \mathbb{A}\left\{ y_\text{I}^4(t) \right\} \right\} + \mathbb{A}\left\{ y_\text{P}^4(t) \right\} + 6\mathbb{E}\left\{ \mathbb{A}\left\{ y_\text{I}^2(t) \right\} \right\} \mathbb{A}\left\{ y_\text{P}^2(t) \right\} \Big),
$$
$$\tag{3.8}$$

and the components can be further rewritten as (note that $\mathbb{E}\left\{ |\tilde{x}_{\text{I},n}|^4 \right\} = 2$ applies a modulation gain on the fourth-order DC terms)

$$
\mathbb{E}\left\{ \mathbb{A}\left\{ y_\text{I}^2(t) \right\} \right\} = \frac{1}{2} \sum_{n=1}^{N} (\mathbf{h}_n^\mathsf{H} \mathbf{w}_{\text{I},n})(\mathbf{h}_n^\mathsf{H} \mathbf{w}_{\text{I},n})^* = \frac{1}{2} \mathbf{h}^\mathsf{H} \mathbf{W}_{\text{I},0} \mathbf{h}, \tag{3.9a}
$$

$$
\mathbb{E}\left\{ \mathbb{A}\left\{ y_\text{I}^4(t) \right\} \right\} = \frac{3}{4} \left(\sum_{n=1}^{N} (\mathbf{h}_n^\mathsf{H} \mathbf{w}_{\text{I},n})(\mathbf{h}_n^\mathsf{H} \mathbf{w}_{\text{I},n})^* \right)^2 = \frac{3}{4} (\mathbf{h}^\mathsf{H} \mathbf{W}_{\text{I},0} \mathbf{h})^2, \tag{3.9b}
$$

$$
\mathbb{A}\left\{ y_\text{P}^2(t) \right\} = \frac{1}{2} \sum_{n=1}^{N} (\mathbf{h}_n^\mathsf{H} \mathbf{w}_{\text{P},n})(\mathbf{h}_n^\mathsf{H} \mathbf{w}_{\text{P},n})^* = \frac{1}{2} \mathbf{h}^\mathsf{H} \mathbf{W}_{\text{P},0} \mathbf{h}, \tag{3.9c}
$$

$$
\mathbb{A}\left\{ y_\text{P}^4(t) \right\} = \frac{3}{8} \sum_{\substack{n_1,n_2,n_3,n_4 \\ n_1+n_2=n_3+n_4}} (\mathbf{h}_{n_1}^\mathsf{H} \mathbf{w}_{\text{P},n_1})(\mathbf{h}_{n_2}^\mathsf{H} \mathbf{w}_{\text{P},n_2})(\mathbf{h}_{n_3}^\mathsf{H} \mathbf{w}_{\text{P},n_3})^*(\mathbf{h}_{n_4}^\mathsf{H} \mathbf{w}_{\text{P},n_4})^*
$$
$$
= \frac{3}{8} \sum_{k=-N+1}^{N-1} (\mathbf{h}^\mathsf{H} \mathbf{W}_{\text{P},k} \mathbf{h})(\mathbf{h}^\mathsf{H} \mathbf{W}_{\text{P},k} \mathbf{h})^*, \tag{3.9d}
$$

where we define $\mathbf{h} \triangleq [\mathbf{h}_1^\mathsf{T}, \ldots, \mathbf{h}_N^\mathsf{T}]^\mathsf{T} \in \mathbb{C}^{MN \times 1}$ and $\mathbf{W}_{\text{I/P}} \triangleq \mathbf{w}_{\text{I/P}} \mathbf{w}_{\text{I/P}}^\mathsf{H} \in \mathbb{H}_+^{MN \times MN}$. As illustrated by Fig. 3.2, $\mathbf{W}_{\text{I/P}}$ can be divided into $N \times N$ blocks of size $M \times M$. Let $\mathbf{W}_{\text{I/P},k}$ keep its block diagonal $k \in \{-N+1, \ldots, N-1\}$ and set all other blocks to $\mathbf{0}$.

$$\mathbf{W}_{\mathrm{I/P}} = \begin{pmatrix} \mathbf{w}_{\mathrm{I/P},1}\mathbf{w}_{\mathrm{I/P},1}^{\mathsf{H}} & \mathbf{w}_{\mathrm{I/P},1}\mathbf{w}_{\mathrm{I/P},2}^{\mathsf{H}} & \cdots & \mathbf{w}_{\mathrm{I/P},1}\mathbf{w}_{\mathrm{I/P},n}^{\mathsf{H}} \\ \mathbf{w}_{\mathrm{I/P},2}\mathbf{w}_{\mathrm{I/P},1}^{\mathsf{H}} & \mathbf{w}_{\mathrm{I/P},2}\mathbf{w}_{\mathrm{I/P},2}^{\mathsf{H}} & \ddots & \vdots \\ \vdots & \ddots & \ddots & \mathbf{w}_{\mathrm{I/P},N-1}\mathbf{w}_{\mathrm{I/P},n}^{\mathsf{H}} \\ \mathbf{w}_{\mathrm{I/P},N}\mathbf{w}_{\mathrm{I/P},1}^{\mathsf{H}} & \cdots & \mathbf{w}_{\mathrm{I/P},N}\mathbf{w}_{\mathrm{I/P},N-1}^{\mathsf{H}} & \mathbf{w}_{\mathrm{I/P},N}\mathbf{w}_{\mathrm{I/P},n}^{\mathsf{H}} \end{pmatrix} \begin{matrix} \\ \\ \leftharpoondown\ k=1 \\ \\ \leftharpoondown\ k=0 \end{matrix}$$

$$k=-1$$

Fig. 3.2 $\mathbf{W}_{\mathrm{I/P}}$ consists of $N \times N$ blocks of size $M \times M$. $\mathbf{W}_{\mathrm{I/P},k}$ keeps the k-th block diagonal of $\mathbf{W}_{\mathrm{I/P}}$ and nulls all remaining blocks. Solid, dashed and dotted blocks correspond to $k > 0$, $k = 0$ and $k < 0$, respectively. For $\mathbf{w}_{\mathrm{I/P},n_1}\mathbf{w}_{\mathrm{I/P},n_2}^{\mathsf{H}}$, the k-th block diagonal satisfies $k = n_2 - n_1$.

3.2.7   Rate-Energy Region

The achievable R-E region for the PS receiver is explicitly defined as

$$\mathcal{C}_{\mathrm{R-E}}(P) \triangleq \Big\{ (r,e) : 0 \le r \le R(\boldsymbol{\theta}, \mathbf{w}_{\mathrm{I}}, \rho),\ 0 \le e \le z(\boldsymbol{\theta}, \mathbf{w}_{\mathrm{I}}, \mathbf{w}_{\mathrm{P}}, \rho),$$
$$\left(\|\mathbf{w}_{\mathrm{I}}\|^2 + \|\mathbf{w}_{\mathrm{P}}\|^2 \right)/2 \le P \Big\}, \tag{3.10}$$

where P is the average transmit power budget and the 1/2 converts the peak to average.

3.3   Problem Formulation

We characterize each R-E boundary point through a DC maximization problem subject to sum rate, transmit power, and reflection amplitude constraints as

$$\max_{\boldsymbol{\theta}, \mathbf{w}_{\mathrm{I}}, \mathbf{w}_{\mathrm{P}}, \rho} \quad z(\boldsymbol{\theta}, \mathbf{w}_{\mathrm{I}}, \mathbf{w}_{\mathrm{P}}, \rho) \tag{3.11a}$$

$$\text{s.t.} \quad R(\boldsymbol{\theta}, \mathbf{w}_{\mathrm{I}}, \rho) \ge \bar{R}, \tag{3.11b}$$

$$\frac{1}{2}\left(\|\mathbf{w}_{\mathrm{I}}\|^2 + \|\mathbf{w}_{\mathrm{P}}\|^2 \right) \le P, \tag{3.11c}$$

$$|\boldsymbol{\theta}| = \mathbf{1}, \tag{3.11d}$$

$$0 \le \rho \le 1. \tag{3.11e}$$

Problem (3.11) is intricate because of the coupled variables in (3.11a), (3.11b) and the non-convex constraint (3.11d). To obtain a feasible solution, we propose a BCD algorithm that iteratively updates (i) the RIS phase shift; (ii) the active precoder; (iii) the waveform amplitude and splitting ratio, until convergence.

3.3.1   Passive Beamforming

In this section, we optimize the RIS phase shift $\boldsymbol{\theta}$ for any given waveform $\mathbf{w}_{\mathrm{I/P}}$ and splitting ratio ρ. Note that

$$
\begin{aligned}
|\mathbf{h}_n^{\mathsf{H}}\mathbf{w}_{\mathrm{I},n}|^2 &= \mathbf{w}_{a\mathrm{I},n}^{\mathsf{H}}\mathbf{h}_n\mathbf{h}_n^{\mathsf{H}}\mathbf{w}_{\mathrm{I},n} \\
&= \mathbf{w}_{\mathrm{I},n}^{\mathsf{H}}(\mathbf{h}_{\mathrm{D},n}+\mathbf{V}_n^{\mathsf{H}}\boldsymbol{\theta})(\mathbf{h}_{\mathrm{D},n}^{\mathsf{H}}+\boldsymbol{\theta}^{\mathsf{H}}\mathbf{V}_n)\mathbf{w}_{\mathrm{I},n} \\
&= \mathbf{w}_{\mathrm{I},n}^{\mathsf{H}}\mathbf{M}_n^{\mathsf{H}}\bar{\boldsymbol{\Theta}}\mathbf{M}_n\mathbf{w}_{\mathrm{I},n} \\
&= \mathrm{tr}(\mathbf{M}_n\mathbf{w}_{\mathrm{I},n}\mathbf{w}_{\mathrm{I},n}^{\mathsf{H}}\mathbf{M}_n^{\mathsf{H}}\bar{\boldsymbol{\Theta}}) \\
&= \mathrm{tr}(\mathbf{C}_n\bar{\boldsymbol{\Theta}}),
\end{aligned}
\tag{3.12}
$$

where $\mathbf{M}_n \triangleq [\mathbf{V}_n^{\mathsf{H}},\mathbf{h}_{\mathrm{D},n}]^{\mathsf{H}} \in \mathbb{C}^{(L+1)\times M}$, t' is an auxiliary variable with unit modulus, $\bar{\boldsymbol{\theta}} \triangleq [\boldsymbol{\theta}^{\mathsf{H}},t']^{\mathsf{H}} \in \mathbb{C}^{(L+1)\times 1}$, $\bar{\boldsymbol{\Theta}} \triangleq \bar{\boldsymbol{\theta}}\bar{\boldsymbol{\theta}}^{\mathsf{H}} \in \mathbb{H}_+^{(L+1)\times(L+1)}$, $\mathbf{C}_n \triangleq \mathbf{M}_n\mathbf{w}_{\mathrm{I},n}\mathbf{w}_{\mathrm{I},n}^{\mathsf{H}}\mathbf{M}_n^{\mathsf{H}} \in \mathbb{H}_+^{(L+1)\times(L+1)}$. On the other hand, we define $t_{\mathrm{I/P},k}$ as

$$
\begin{aligned}
t_{\mathrm{I/P},k} &\triangleq \mathbf{h}^{\mathsf{H}}\mathbf{W}_{\mathrm{I/P},k}\mathbf{h} \\
&= \mathrm{tr}(\mathbf{h}\mathbf{h}^{\mathsf{H}}\mathbf{W}_{\mathrm{I/P},k}) \\
&= \mathrm{tr}\left((\mathbf{h}_D+\mathbf{V}^{\mathsf{H}}\boldsymbol{\theta})(\mathbf{h}_D^{\mathsf{H}}+\boldsymbol{\theta}^{\mathsf{H}}\mathbf{V})\mathbf{W}_{\mathrm{I/P},k}\right) \\
&= \mathrm{tr}(\mathbf{M}^{\mathsf{H}}\bar{\boldsymbol{\Theta}}\mathbf{M}\mathbf{W}_{\mathrm{I/P},k}) \\
&= \mathrm{tr}(\mathbf{M}\mathbf{W}_{\mathrm{I/P},k}\mathbf{M}^{\mathsf{H}}\bar{\boldsymbol{\Theta}}) \\
&= \mathrm{tr}(\mathbf{C}_{\mathrm{I/P},k}\bar{\boldsymbol{\Theta}}),
\end{aligned}
\tag{3.13}
$$

where $\mathbf{V} \triangleq [\mathbf{V}_1,\ldots,\mathbf{V}_N] \in \mathbb{C}^{L\times MN}$, $\mathbf{M} \triangleq [\mathbf{V}^{\mathsf{H}},\mathbf{h}_D]^{\mathsf{H}} \in \mathbb{C}^{(L+1)\times MN}$, $\mathbf{C}_{\mathrm{I/P},k} \triangleq \mathbf{M}\mathbf{W}_{\mathrm{I/P},k}\mathbf{M}^{\mathsf{H}} \in \mathbb{C}^{(L+1)\times(L+1)}$. On top of this, (3.6) and (3.8) reduce respectively to

$$
R(\bar{\boldsymbol{\Theta}}) = \sum_{n=1}^{N}\log_2\left(1+\frac{(1-\rho)\mathrm{tr}(\mathbf{C}_n\bar{\boldsymbol{\Theta}})}{\sigma_n^2}\right),
\tag{3.14}
$$

$$
z(\bar{\boldsymbol{\Theta}}) = \frac{1}{2}\beta_2\rho(t_{\mathrm{I},0}+t_{\mathrm{P},0})+\frac{3}{8}\beta_4\rho^2\left(2t_{\mathrm{I},0}^2+\sum_{k=-N+1}^{N-1}t_{\mathrm{P},k}t_{\mathrm{P},k}^*\right)+\frac{3}{2}\beta_4\rho^2t_{\mathrm{I},0}t_{\mathrm{P},0}.
\tag{3.15}
$$

To maximize the non-concave expression (3.15), we successively lower bound the second-order terms by their first-order Taylor expansions [121]. Based on the solution at iteration $r-1$, the approximations at iteration r are

$$(t_{\mathrm{I},0}^{(r)})^2 \geq 2t_{\mathrm{I},0}^{(r)}t_{\mathrm{I},0}^{(r-1)} - (t_{\mathrm{I},0}^{(r-1)})^2, \tag{3.16}$$

$$t_{\mathrm{P},k}^{(r)}(t_{\mathrm{P},k}^{(r)})^* \geq 2\Re\left\{t_{\mathrm{P},k}^{(r)}(t_{\mathrm{P},k}^{(r-1)})^*\right\} - t_{\mathrm{P},k}^{(r-1)}(t_{\mathrm{P},k}^{(r-1)})^*, \tag{3.17}$$

$$t_{\mathrm{I},0}^{(r)}t_{\mathrm{P},0}^{(r)} \geq t_{\mathrm{I},0}^{(r)}t_{\mathrm{P},0}^{(r-1)} + t_{\mathrm{P},0}^{(r)}t_{\mathrm{I},0}^{(r-1)} - t_{\mathrm{I},0}^{(r-1)}t_{\mathrm{P},0}^{(r-1)}. \tag{3.18}$$

Note that $t_{\mathrm{I/P},0} = \mathrm{tr}(\mathbf{C}_{\mathrm{I/P},0}\bar{\mathbf{\Theta}})$ is real-valued because $\mathbf{C}_{\mathrm{I/P},0}$ and $\bar{\mathbf{\Theta}}$ are Hermitian matrices. Due to symmetry [122], we have

$$\sum_{k=-N+1}^{N-1} \Re\left\{t_{\mathrm{P},k}^{(r)}(t_{\mathrm{P},k}^{(r-1)})^*\right\} = \sum_{k=-N+1}^{N-1} t_{\mathrm{P},k}^{(r)}(t_{\mathrm{P},k}^{(r-1)})^*. \tag{3.19}$$

Plugging (3.16)–(3.19) into (3.15), we obtain the DC approximation $\tilde{z}$ as

$$\begin{aligned} \tilde{z}(\bar{\mathbf{\Theta}}^{(r)}) = &\frac{1}{2}\beta_2\rho(t_{\mathrm{I},0}^{(r)} + t_{\mathrm{P},0}^{(r)}) + \frac{3}{2}\beta_4\rho^2\left(t_{\mathrm{I},0}^{(r)}t_{\mathrm{P},0}^{(r-1)} + t_{\mathrm{P},0}^{(r)}t_{\mathrm{I},0}^{(r-1)} - t_{\mathrm{I},0}^{(r-1)}t_{\mathrm{P},0}^{(r-1)}\right) \\ &+ \frac{3}{8}\beta_4\rho^2\left(4t_{\mathrm{I},0}^{(r)}t_{\mathrm{I},0}^{(r-1)} - 2(t_{\mathrm{I},0}^{(r-1)})^2 + \sum_{k=-N+1}^{N-1} 2t_{\mathrm{P},k}^{(r)}(t_{\mathrm{P},k}^{(r-1)})^* - t_{\mathrm{P},k}^{(r-1)}(t_{\mathrm{P},k}^{(r-1)})^*\right), \end{aligned} \tag{3.20}$$

and transform problem (3.11) to

$$\max_{\bar{\mathbf{\Theta}}} \quad \tilde{z}(\bar{\mathbf{\Theta}}) \tag{3.21a}$$

$$\text{s.t.} \quad R(\bar{\mathbf{\Theta}}) \geq \bar{R}, \tag{3.21b}$$

$$\mathrm{diag}^{-1}(\bar{\mathbf{\Theta}}) = \mathbf{1}, \tag{3.21c}$$

$$\bar{\mathbf{\Theta}} \succeq \mathbf{0}, \tag{3.21d}$$

$$\mathrm{rank}(\bar{\mathbf{\Theta}}) = 1. \tag{3.21e}$$

The unit-rank constraint (3.21e) can be relaxed to formulate a Semi-Definite Programming (SDP) with approximation accuracy no greater than $\pi/4$ [123]. The resulting problem can be solved efficiently by `CVX toolbox` [124].

Proposition 1. *Any optimal solution $\bar{\mathbf{\Theta}}^\star$ to the relaxed passive beamforming problem* (3.21a)–(3.21d) *is strictly rank-1. That is to say,* (3.21e) *is redundant and no loss is introduced by Semi-Definite Relaxation (SDR).*

Algorithm 1 SCA: RIS Phase Shift.

 1: **Input** β_2, β_4, $\mathbf{h}_{\mathrm{D},n}$, $\mathbf{V}_n$, σ_n, $\mathbf{w}_{\mathrm{I/P},n}$, ρ, $\bar{R}$, ϵ, $\forall n$
 2: Construct $\mathbf{V}$, $\mathbf{M}$, $\mathbf{M}_n$, $\mathbf{C}_n$, $\mathbf{C}_{\mathrm{I/P},k}$, $\forall n, k$
 3: **Initialize** $i \leftarrow 0$, $\bar{\mathbf{\Theta}}^{(0)}$
 4: Set $t^{(0)}_{\mathrm{I/P},k}$, $\forall k$ by (3.13)
 5: Compute $z^{(0)}$ by (3.15)
 6: **Repeat**
 7:       $i \leftarrow i + 1$
 8:       Get $\bar{\mathbf{\Theta}}^{(r)}$ by solving (3.21a)–(3.21d)
 9:       Update $t^{(r)}_{\mathrm{I/P},k}$, $\forall k$ by (3.13)
10:       Compute $z^{(r)}$ by (3.15)
11: **Until** $\left| z^{(r)} - z^{(r-1)} \right| \leq \epsilon$
12: Set $\bar{\mathbf{\Theta}}^{\star} \leftarrow \bar{\mathbf{\Theta}}^{(r)}$
13: Get $\hat{\boldsymbol{\theta}}^{\star}$ by eigen decomposition, $\bar{\mathbf{\Theta}}^{\star} = \hat{\boldsymbol{\theta}}^{\star}(\hat{\boldsymbol{\theta}}^{\star})^{\mathsf{H}}$
14: Set $\boldsymbol{\theta}^{\star} \leftarrow e^{j \arg\left([\hat{\boldsymbol{\theta}}^{\star}]_{(1:L)} / [\hat{\boldsymbol{\theta}}^{\star}]_{(L+1)} \right)}$
15: **Output** $\boldsymbol{\theta}^{\star}$

Proof. Please refer to Appendix 4.1.1.   □

In summary, we update $\bar{\mathbf{\Theta}}^{(r)}$ by iteratively solving (3.21a)–(3.21d) until convergence, extract $\hat{\boldsymbol{\theta}}^{\star}$ by eigen decomposition, and retrieve the RIS vector by $\boldsymbol{\theta}^{\star} = e^{j \arg\left([\hat{\boldsymbol{\theta}}^{\star}]_{(1:L)} / [\hat{\boldsymbol{\theta}}^{\star}]_{(L+1)} \right)}$. The passive beamforming design is summarized in the SCA Algorithm 1, where the relaxed problem (3.21a)–(3.21d) involves a $(L + 1)$-order positive semi-definite matrix variable and $(L + 2)$ linear constraints. Given a solution accuracy ϵ_{IPM} for the interior-point method, the computational complexity of Algorithm 1 is $\mathcal{O}\left(I_{\mathrm{SCA}}(L + 2)^4 (L + 1)^{0.5} \log(\epsilon_{\mathrm{IPM}}^{-1}) \right)$, where I_{SCA} denotes the number of SCA iterations [123].

Proposition 2. *For any feasible initial point with given waveform and splitting ratio, the SCA Algorithm 1 is guaranteed to converge to local optimal points of the original problem* (3.11).

Proof. Please refer to Appendix 4.1.2.   □

3.3.2   Active Beamforming

The original waveform and active beamforming problem (3.11) is over complex-valued vectors $\mathbf{w}_{\mathrm{I/P}}$ of size $MN \times 1$. The weight on subband n can be decomposed in spatial and frequency domains as

$$\mathbf{w}_{\mathrm{I/P},n} = s_{\mathrm{I/P},n} \mathbf{p}_{\mathrm{I/P},n}, \tag{3.22}$$

where $s_{\mathrm{I/P},n}$ denotes the amplitude of the modulated/multisine waveform at tone n, and $\mathbf{p}_{\mathrm{I/P},n}$ denotes the corresponding information/power precoder. This decoupling allows independent spatial and frequency optimizations, reducing the size of variables from $2MN$ to $2(M+N)$.

Proposition 3. *For single-user SWIPT, the global optimal information and power precoders coincide at the MRT*

$$\mathbf{p}_{\mathrm{I/P},n}^{\star} = \frac{\mathbf{h}_n}{\|\mathbf{h}_n\|}. \tag{3.23}$$

Proof. Please refer to Appendix 4.1.3. □

3.3.3 Waveform and Splitting Ratio

Next, we jointly optimize the waveform amplitude $\mathbf{s}_{\mathrm{I/P}} \triangleq [s_{\mathrm{I/P},1}, \ldots, s_{\mathrm{I/P},N}]^{\mathsf{T}} \in \mathbb{R}_+^{N \times 1}$ and the splitting ratio $\rho \in \mathbb{I}$ for any given RIS phase shift $\boldsymbol{\theta}$ and active precoder $\mathbf{p}_{\mathrm{I/P},n}, \forall n$. With MRT precoder (3.23), the equivalent channel strength at subband n is $\|\mathbf{h}_n\|$, such that the achievable rate (3.6) reduces to

$$R(\mathbf{s}_{\mathrm{I}}, \rho) = \log_2 \prod_{n=1}^{N} \left(1 + \frac{(1-\rho)\|\mathbf{h}_n\|^2 s_{\mathrm{I},n}^2}{\sigma_n^2} \right), \tag{3.24}$$

and the DC (3.8) rewrites as

$$
\begin{aligned}
z(\mathbf{s}_{\mathrm{I}}, \mathbf{s}_{\mathrm{P}}, \rho) = {} & \frac{1}{2}\beta_2\rho \sum_{n=1}^{N} \|\mathbf{h}_n\|^2 (s_{\mathrm{I},n}^2 + s_{\mathrm{P},n}^2) \\
& + \frac{3}{8}\beta_4\rho^2 \left(2 \sum_{n_1,n_2} \prod_{j=1}^{2} \|\mathbf{h}_{n_j}\|^2 s_{\mathrm{I},n_j}^2 + \sum_{\substack{n_1,n_2,n_3,n_4 \\ n_1+n_2=n_3+n_4}} \prod_{j=1}^{4} \|\mathbf{h}_{n_j}\| s_{\mathrm{P},n_j} \right) \\
& + \frac{3}{2}\beta_4\rho^2 \left(\sum_{n_1,n_2} \|\mathbf{h}_{n_1}\|^2 \|\mathbf{h}_{n_2}\|^2 s_{\mathrm{I},n_1}^2 s_{\mathrm{P},n_2}^2 \right).
\end{aligned} \tag{3.25}
$$

Problem (3.11) boils down to

$$\max_{\mathbf{s}_{\mathrm{I}},\mathbf{s}_{\mathrm{P}},\rho} \quad z(\mathbf{s}_{\mathrm{I}}, \mathbf{s}_{\mathrm{P}}, \rho) \tag{3.26a}$$

$$\text{s.t.} \quad R(\mathbf{s}_{\mathrm{I}}, \rho) \geq \bar{R}, \tag{3.26b}$$

$$\frac{1}{2} \left(\|\mathbf{s}_{\mathrm{I}}\|^2 + \|\mathbf{s}_{\mathrm{P}}\|^2 \right) \leq P. \tag{3.26c}$$

Following [72], we introduce auxiliary variables t'', $\bar{\rho}$ and transform problem (3.26) into a reversed GP

$$\min_{\mathbf{s}_\mathrm{I}, \mathbf{s}_\mathrm{P}, \rho, \bar{\rho}, t''} \quad \frac{1}{t''} \tag{3.27a}$$

$$\text{s.t.} \quad \frac{t''}{z(\mathbf{s}_\mathrm{I}, \mathbf{s}_\mathrm{P}, \rho)} \leq 1, \tag{3.27b}$$

$$\frac{2^{\bar{R}}}{\prod_{n=1}^{N} \left(1 + \bar{\rho}\|\mathbf{h}_n\|^2 s_{\mathrm{I},n}^2 / \sigma_n^2\right)} \leq 1, \tag{3.27c}$$

$$\frac{1}{2}\left(\|\mathbf{s}_\mathrm{I}\|^2 + \|\mathbf{s}_\mathrm{P}\|^2\right) \leq P, \tag{3.27d}$$

$$\rho + \bar{\rho} \leq 1. \tag{3.27e}$$

Apparently, $\bar{\rho}^\star = 1 - \rho^\star$ as no power should be wasted at the receiver. The denominators of (3.27c) and (3.27b) consist of posynomials [125] that can be decomposed as sums of monomials

$$1 + \frac{\bar{\rho}\|\mathbf{h}_n\|^2 s_{\mathrm{I},n}^2}{\sigma_n^2} \triangleq \sum_{m_{\mathrm{I},n}} g_{m_{\mathrm{I},n}}(s_{\mathrm{I},n}, \bar{\rho}), \tag{3.28}$$

$$z(\mathbf{s}_\mathrm{I}, \mathbf{s}_\mathrm{P}, \rho) \triangleq \sum_{m_\mathrm{P}} g_{m_\mathrm{P}}(\mathbf{s}_\mathrm{I}, \mathbf{s}_\mathrm{P}, \rho). \tag{3.29}$$

We upper bound (3.28) and (3.29) by the Geomtric Mean (GM)-Arithmetic Mean (AM) inequality [126] and transform problem (3.27) to

$$\min_{\mathbf{s}_\mathrm{I}, \mathbf{s}_\mathrm{P}, \rho, \bar{\rho}, t''} \quad \frac{1}{t''} \tag{3.30a}$$

$$\text{s.t.} \quad t'' \prod_{m_\mathrm{P}} \left(\frac{g_{m_\mathrm{P}}(\mathbf{s}_\mathrm{I}, \mathbf{s}_\mathrm{P}, \rho)}{\gamma_{m_\mathrm{P}}}\right)^{-\gamma_{m_\mathrm{P}}} \leq 1, \tag{3.30b}$$

$$2^{\bar{R}} \prod_{n} \prod_{m_{\mathrm{I},n}} \left(\frac{g_{m_{\mathrm{I},n}}(s_{\mathrm{I},n}, \bar{\rho})}{\gamma_{m_{\mathrm{I},n}}}\right)^{-\gamma_{m_{\mathrm{I},n}}} \leq 1, \tag{3.30c}$$

$$\frac{1}{2}\left(\|\mathbf{s}_\mathrm{I}\|^2 + \|\mathbf{s}_\mathrm{P}\|^2\right) \leq P, \tag{3.30d}$$

$$\rho + \bar{\rho} \leq 1, \tag{3.30e}$$

Algorithm 2 GP: Waveform Amplitude and Splitting Ratio.

1: **Input** β_2, β_4, $\mathbf{h}_n$, P, σ_n, $\bar{R}$, ϵ, $\forall n$
2: **Initialize** $i \leftarrow 0$, $\mathbf{s}_{\mathrm{I/P}}^{(0)}$, $\rho^{(0)}$
3: Compute $R^{(0)}$, $z^{(0)}$ by (3.24), (3.25)
4: Set $g_{m_{\mathrm{I},n}}^{(0)}$, $g_{m_{\mathrm{P}}}^{(0)}$, $\forall n$ by (3.28), (3.29)
5: **Repeat**
6:     $i \leftarrow i + 1$
7:     Update $\gamma_{m_{\mathrm{I},n}}^{(r)}$, $\gamma_{m_{\mathrm{P}}}^{(r)}$, $\forall n$ by (3.31), (3.32)
8:     Get $\mathbf{s}_{\mathrm{I/P}}^{(r)}$, $\rho^{(r)}$ by solving problem (3.30)
9:     Compute $R^{(r)}$, $z^{(r)}$ by (3.24), (3.25)
10:    Update $g_{m_{\mathrm{I},n}}^{(r)}$, $g_{m_{\mathrm{P}}}^{(r)}$, $\forall n$ by (3.28), (3.29)
11: **Until** $|z^{(r)} - z^{(r-1)}| \leq \epsilon$
12: Set $\mathbf{s}_{\mathrm{I/P}}^{\star} \leftarrow \mathbf{s}_{\mathrm{I/P}}^{(r)}$, $\rho^{\star} \leftarrow \rho^{(r)}$
13: **Output** $\mathbf{s}_{\mathrm{I}}^{\star}$, $\mathbf{s}_{\mathrm{P}}^{\star}$, $\rho^{\star}$

---

where $\gamma_{m_{\mathrm{I},n}}, \gamma_{m_{\mathrm{P}}} \geq 0$ and $\sum_{m_{\mathrm{I},n}} \gamma_{m_{\mathrm{I},n}} = \sum_{m_{\mathrm{P}}} \gamma_{m_{\mathrm{P}}} = 1$. The tightness of the AM-GM inequality depends on the selection of $\{\gamma_{m_{\mathrm{I},n}}, \gamma_{m_{\mathrm{P}}}\}$, and a feasible choice at iteration r is

$$\gamma_{m_{\mathrm{I},n}}^{(r)} = \frac{g_{m_{\mathrm{I},n}}(s_{\mathrm{I},n}^{(r-1)}, \bar{\rho}^{(r-1)})}{1 + \bar{\rho}^{(r-1)}\|\mathbf{h}_n\|^2 (s_{\mathrm{I},n}^{(r-1)})^2 / \sigma_n^2}, \tag{3.31}$$

$$\gamma_{m_{\mathrm{P}}}^{(r)} = \frac{g_{m_{\mathrm{P}}}(\mathbf{s}_{\mathrm{I}}^{(r-1)}, \mathbf{s}_{\mathrm{P}}^{(r-1)}, \rho^{(r-1)})}{z(\mathbf{s}_{\mathrm{I}}^{(r-1)}, \mathbf{s}_{\mathrm{P}}^{(r-1)}, \rho^{(r-1)})}. \tag{3.32}$$

With (3.31) and (3.32), problem (3.30) becomes convex and can be solved by `CVX toolbox` [124]. We update $\mathbf{s}_{\mathrm{I}}^{(r)}, \mathbf{s}_{\mathrm{P}}^{(r)}, \rho^{(r)}$ iteratively until convergence. The joint waveform amplitude and splitting ratio design is summarized in the GP Algorithm 2, which achieves local optimality at the cost of exponential computational complexity [126].

Proposition 4. *For any feasible initial point, the GP Algorithm 2 is guaranteed to converge to local optimal points of the waveform amplitude and splitting ratio design problem* (3.26).

Proof. The proof is similar to [63, 72] and is omitted here. □

3.3.4 Low-Complexity Adaptive Design

To facilitate practical SWIPT implementation, we propose two closed-form waveform schemes for TS and PS receivers, respectively.

- *TS:* As discussed Section 2.3.3.2, each time block is divided into orthogonal phases and there is no waveform superposition. For the WIT phase, the optimal modulated

waveform amplitude is given by the WF strategy [127]

$$s_{\mathrm{I},n} = \sqrt{2\left(\lambda - \frac{\sigma_n^2}{P\|\mathbf{h}_n\|^2}\right)^+}, \tag{3.33}$$

where λ is chosen to satisfy the power constraint $\|\mathbf{s}_I\|^2/2 \leq P$ and can be obtained by iterative methods [128]. For the WPT phase, a reasonable multisine waveform amplitude is given by the SMF strategy [106]

$$s_{\mathrm{P},n} = \sqrt{\frac{2P}{\sum_{n=1}^N \|\mathbf{h}_n\|^{2\alpha}}} \|\mathbf{h}_n\|^\alpha, \tag{3.34}$$

where the scaling ratio $\alpha \geq 1$ is a design parameter that exploits the rectifier nonlinearity and frequency selectivity.

- *PS:* When the receiver works in PS mode, the modulated and multisine components in the superposed waveform are respectively

$$s_{\mathrm{I},n} = \sqrt{2(1-\delta)\left(\lambda - \frac{\sigma_n^2}{P\|\mathbf{h}_n\|^2}\right)^+}, \tag{3.35}$$

$$s_{\mathrm{P},n} = \sqrt{\frac{2\delta P}{\sum_{n=1}^N \|\mathbf{h}_n\|^{2\alpha}}} \|\mathbf{h}_n\|^\alpha, \tag{3.36}$$

where the $\delta \in \mathbb{I}$ determines the power ratio of multisine waveform at the transmitter, and $\rho \in \mathbb{I}$ determines the power ratio of the energy harvester at the receiver.[1]

To accommodate the low-complexity waveform schemes, minor modifications should be made for the passive beamforming design. Specifically, the rate constraint (3.21b) should be dropped, since the achievable rate is controlled by η in TS or $\{\delta, \rho\}$ in PS. To achieve the WIT point, the rate (3.14) should be maximized and the DC expression (3.20) can be dropped. The Modified-SCA (M-SCA) Algorithm 3 summarizes the modified passive beamforming design when the receiver works in PS mode. Similar to propositions 1 and 2, no loss is introduced by SDR and local optimality is guaranteed. Since each SDP involves $(L+1)$ linear constraints, the computational complexity of Algorithm 3 is $\mathcal{O}\left(I_{\mathrm{M-SCA}}(L+1)^{4.5}\log(\epsilon_{\mathrm{IPM}}^{-1})\right)$, where $I_{\mathrm{M-SCA}}$ denotes the number of M-SCA iterations [123].

---

[1]We notice that $\delta^\star = \rho^\star = 0$ at the WIT point and $\delta^\star = \rho^\star = 1$ at the WPT point. Intuitively, $\delta^\star$ and $\rho^\star$ should be positively correlated to improve the R-E trade-off.

Algorithm 3 M-SCA: RIS Phase Shift.
___
 1: **Input** β_2, β_4, $\mathbf{h}_{\mathrm{D},n}$, $\mathbf{V}_n$, σ_n, $\mathbf{w}_{\mathrm{I/P},n}$, ρ, ϵ, $\forall n$
 2: Construct $\mathbf{V}$, $\mathbf{M}$, $\mathbf{M}_n$, $\mathbf{C}_n$, $\mathbf{C}_{\mathrm{I/P},k}$, $\forall n, k$
 3: **Initialize** $i \leftarrow 0$, $\bar{\mathbf{\Theta}}^{(0)}$
 4: **If** $\rho = 0$
 5:     Get $\bar{\mathbf{\Theta}}^{\star}$ by maximizing (3.14) s.t. (3.21c), (3.21d)
 6: **Else**
 7:     Set $t_{\mathrm{I/P},k}^{(0)}$, $\forall k$ by (3.13)
 8:     Compute $z^{(0)}$ by (3.15)
 9:     **Repeat**
10:         $i \leftarrow i + 1$
11:         Get $\bar{\mathbf{\Theta}}^{(r)}$ by maximizing (3.20) s.t. (3.21c), (3.21d)
12:         Update $t_{\mathrm{I/P},k}^{(r)}$, $\forall k$ by (3.13)
13:         Compute $z^{(r)}$ by (3.15)
14:     **Until** $|z^{(r)} - z^{(r-1)}| \leq \epsilon$
15:     Set $\bar{\mathbf{\Theta}}^{\star} \leftarrow \bar{\mathbf{\Theta}}^{(r)}$
16: **End If**
17: Get $\hat{\boldsymbol{\theta}}^{\star}$ by eigen decomposition, $\bar{\mathbf{\Theta}}^{\star} = \hat{\boldsymbol{\theta}}^{\star}(\hat{\boldsymbol{\theta}}^{\star})^{\mathsf{H}}$
18: Set $\boldsymbol{\theta}^{\star} \leftarrow e^{\jmath \arg\left([\hat{\boldsymbol{\theta}}^{\star}]_{(1:L)}/[\hat{\boldsymbol{\theta}}^{\star}]_{(L+1)}\right)}$
19: **Output** $\boldsymbol{\theta}^{\star}$

3.3.5 Block Coordinate Descent

Based on the direct and cascaded CSIT, we iteratively update the passive beamforming $\boldsymbol{\theta}$ by Algorithm 1, the active precoder $\mathbf{p}_{\mathrm{I/P},n}$, $\forall n$ by equation (3.23), and the waveform amplitude $\mathbf{s}_{\mathrm{I/P}}$ and splitting ratio ρ by Algorithm 2, until convergence. The steps are summarized in the BCD Algorithm 4, whose computational complexity is exponential as inherited from Algorithm 2. It is guaranteed to converge, but may end up with a suboptimal solution because variables are coupled in constraint (3.11b) [129]. The R-E region is obtained by varying the rate constraint from 0 to $C_{\max}$.

For the Low-Complexity (LC) design under PS mode, we obtain the phase shift by Algorithm 3, the active precoder $\mathbf{p}_{\mathrm{I/P},n}$, $\forall n$ by equation (3.23), and the waveform amplitude by (3.35) and (3.36). The R-E region is obtained by performing a two-dimensional search over (δ, ρ) from $(0, 0)$ to $(1, 1)$. The steps are summarized in Algorithm 5. The computational complexity of Algorithm 5 is $\mathcal{O}\left(I_{\mathrm{LC-BCD}} I_{\mathrm{M-SCA}}(L+1)^{4.5} \log(\epsilon_{\mathrm{IPM}}^{-1})\right)$, where $I_{\mathrm{LC-BCD}}$ denotes the number of LC-BCD iterations [123].

Algorithm 4 BCD: Waveform, Beamforming and Splitting Ratio.

1: **Input** β_2, β_4, $\mathbf{h}_{\mathrm{D},n}$, $\mathbf{V}_n$, P, σ_n, $\bar{R}$, ϵ, $\forall n$
2: **Initialize** $i \leftarrow 0$, $\boldsymbol{\theta}^{(0)}$, $\mathbf{p}_{\mathrm{I/P},n}^{(0)}$, $\mathbf{s}_{\mathrm{I/P}}^{(0)}$, $\rho^{(0)}$, $\forall n$
3: Set $\mathbf{w}_{\mathrm{I/P},n}^{(0)}$, $\forall n$ by (3.22)
4: Compute $z^{(0)}$ by (3.25)
5: **Repeat**
6:      $i \leftarrow i + 1$
7:      Get $\boldsymbol{\theta}^{(r)}$ based on $\mathbf{w}_{\mathrm{I/P}}^{(r-1)}$, $\rho^{(r-1)}$ by Algorithm 1
8:      Update $\mathbf{h}_n^{(r)}$, $\mathbf{p}_n^{(r)}$, $\forall n$ by (3.4), (3.23)
9:      Get $\mathbf{s}_{\mathrm{I/P}}^{(r)}$, $\rho^{(r)}$ by Algorithm 2
10:      Update $\mathbf{w}_{\mathrm{I/P},n}^{(r)}$, $\forall n$ by (3.22)
11:      Compute $z^{(r)}$ by (3.25)
12: **Until** $|z^{(r)} - z^{(r-1)}| \leq \epsilon$
13: Set $\boldsymbol{\theta}^{\star} \leftarrow \boldsymbol{\theta}^{(r)}$, $\mathbf{w}_{\mathrm{I/P}}^{\star} \leftarrow \mathbf{w}_{\mathrm{I/P}}^{(r)}$, $\rho^{\star} \leftarrow \rho^{(r)}$
14: **Output** $\boldsymbol{\theta}^{\star}$, $\mathbf{w}_{\mathrm{I}}^{\star}$, $\mathbf{w}_{\mathrm{P}}^{\star}$, $\rho^{\star}$

Algorithm 5 LC-BCD: Waveform and Beamforming.

1: **Input** β_2, β_4, $\mathbf{h}_{\mathrm{D},n}$, $\mathbf{V}_n$, P, σ_n, δ, ρ, ϵ, $\forall n$
2: **Initialize** $i \leftarrow 0$, $\boldsymbol{\theta}^{(0)}$, $\mathbf{p}_{\mathrm{I/P},n}^{(0)}$, $\mathbf{s}_{\mathrm{I/P}}^{(0)}$, $\forall n$
3: Set $\mathbf{w}_{\mathrm{I/P},n}^{(0)}$, $\forall n$ by (3.22)
4: Compute $R^{(0)}$, $z^{(0)}$ by (3.24), (3.25)
5: **Repeat**
6:      $i \leftarrow i + 1$
7:      Get $\boldsymbol{\theta}^{(r)}$ based on $\mathbf{w}_{\mathrm{I/P}}^{(r-1)}$ by Algorithm 3
8:      Update $\mathbf{h}_n^{(r)}$, $\mathbf{p}_n^{(r)}$, $\forall n$ by (3.4), (3.23)
9:      Update $\mathbf{s}_{\mathrm{I}}^{(r)}$, $\mathbf{s}_{\mathrm{P}}^{(r)}$ by (3.35), (3.36)
10:      Update $\mathbf{w}_{\mathrm{I/P},n}^{(r)}$, $\forall n$ by (3.22)
11:      Compute $R^{(r)}$, $z^{(r)}$ by (3.24), (3.25)
12:      **If** $\rho = 0$
13:          $\Delta \leftarrow R^{(r)} - R^{(r-1)}$
14:      **Else**
15:          $\Delta \leftarrow z^{(r)} - z^{(r-1)}$
16:      **End If**
17: **Until** $|\Delta| \leq \epsilon$
18: Set $\boldsymbol{\theta}^{\star} \leftarrow \boldsymbol{\theta}^{(r)}$, $\mathbf{w}_{\mathrm{I/P}}^{\star} \leftarrow \mathbf{w}_{\mathrm{I/P}}^{(r)}$
19: **Output** $\boldsymbol{\theta}^{\star}$, $\mathbf{w}_{\mathrm{I}}^{\star}$, $\mathbf{w}_{\mathrm{P}}^{\star}$
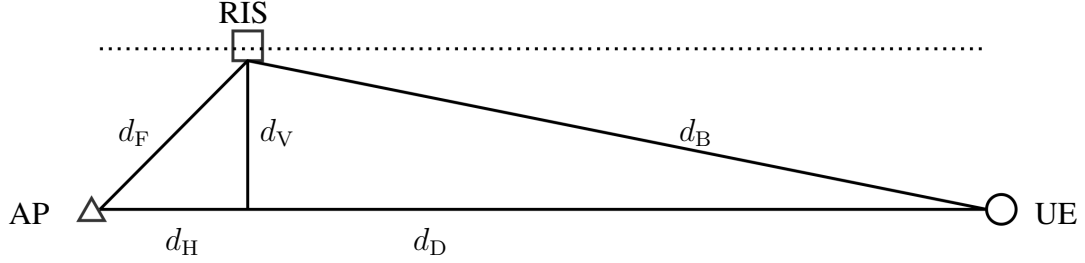
3.4   Performance Evaluations

Fig. 3.3 System layout in simulation.

To evaluate the proposed RIS-aided SWIPT system, we consider the layout in Fig. 3.3 where the RIS moves along a line parallel to the AP-UE path. Let d_H, d_V be the horizontal and vertical distances from the AP to the RIS, and denote respectively d_D, $d_\mathrm{F} = \sqrt{d_\mathrm{H}^2 + d_\mathrm{V}^2}$, $d_\mathrm{B} = \sqrt{(d_\mathrm{D} - d_\mathrm{H})^2 + d_\mathrm{V}^2}$ as the distance of direct, forward and backward links. Set $d_\mathrm{D} = 12\,\mathrm{m}$ and $d_\mathrm{H} = d_\mathrm{V} = 2\,\mathrm{m}$ as reference. The path loss of direct, forward and backward links are denoted by Λ_D, Λ_F and Λ_B, respectively. We consider a large open space Wi-Fi-like environment at center frequency $2.4\,\mathrm{GHz}$ where the channel follows IEEE TGn channel model D [130]. Specifically, the path loss exponent is 2 (i.e., free-space model) up to $10\,\mathrm{m}$, and 3.5 onwards to penalize the potential blockage. All fadings are modeled as NLoS with tap delays and powers specified in model D, and the tap gains are modeled as i.i.d. CSCG variables. Rectenna parameters are set to $k_2 = 0.0034$, $k_4 = 0.3829$, $R_\mathrm{A} = 50\,\Omega$ [63] such that $\beta_2 = 0.17$ and $\beta_4 = 957.25$. We also choose the average Effective Isotropic Radiated Power (EIRP) as $P = 40\,\mathrm{dBm}$, the receive antenna gain as $3\,\mathrm{dBi}$, the scaling ratio as $\alpha = 2$, and the tolerance as $\epsilon = 10^{-8}$. To further reduce the complexity, we assume $\delta = \rho$ and perform a one-dimensional search for the LC-BCD algorithm. Each R-E point is averaged over 200 channel realizations, and the x-axis is normalized to per-subband rate R/N.
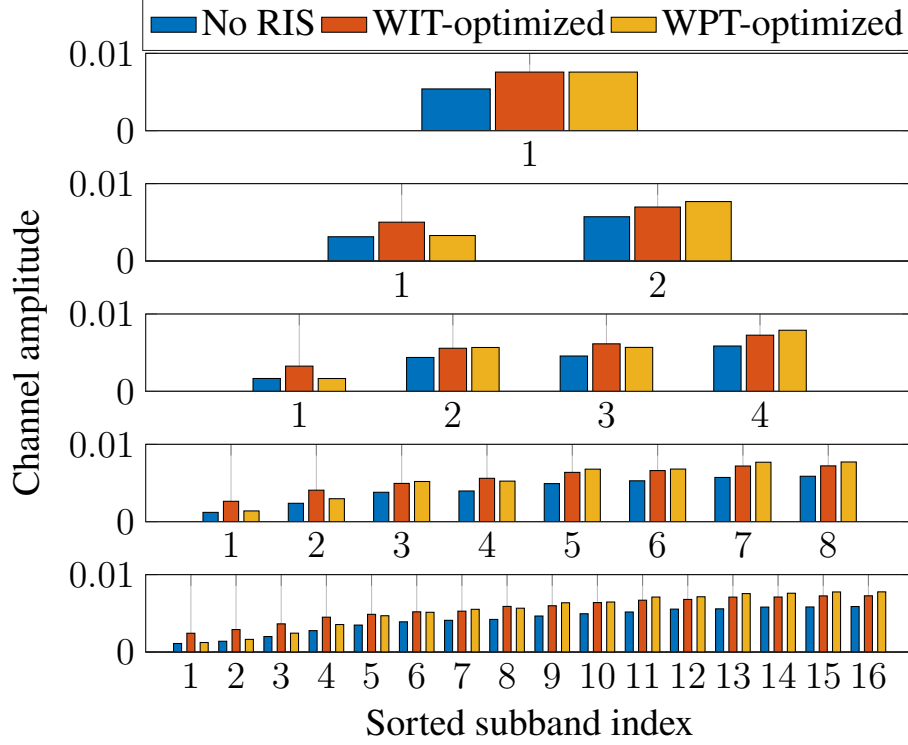
3.4.1 Subchannel Manipulation

Fig. 3.4 Sorted equivalent subchannel amplitude with and without RIS versus N for $M = 1$, $L = 100$, $\sigma_n^2 = -40\,\text{dBm}$, $B = 10\,\text{MHz}$ and $d_\text{H} = d_\text{V} = 2\,\text{m}$.

Fig. 3.4 reveals how RIS influences the sorted equivalent subchannel amplitude for one channel realization. Due to the flexible subchannel design enabled by passive beamforming, the optimal amplitude distribution for WIT and WPT are dissimilar. Under the specified configuration, the WPT-optimized RIS aligns the strong subbands to exploit the rectifier nonlinearity. On the other hand, the WIT-optimized RIS provides a fair gain over all subchannels when L is sufficiently large. This is reminiscent of the WF scheme at high SNR, but is realized by channel alignment by RIS instead of resource allocation by transmitter.

3.4.2 R-E Region Characterization
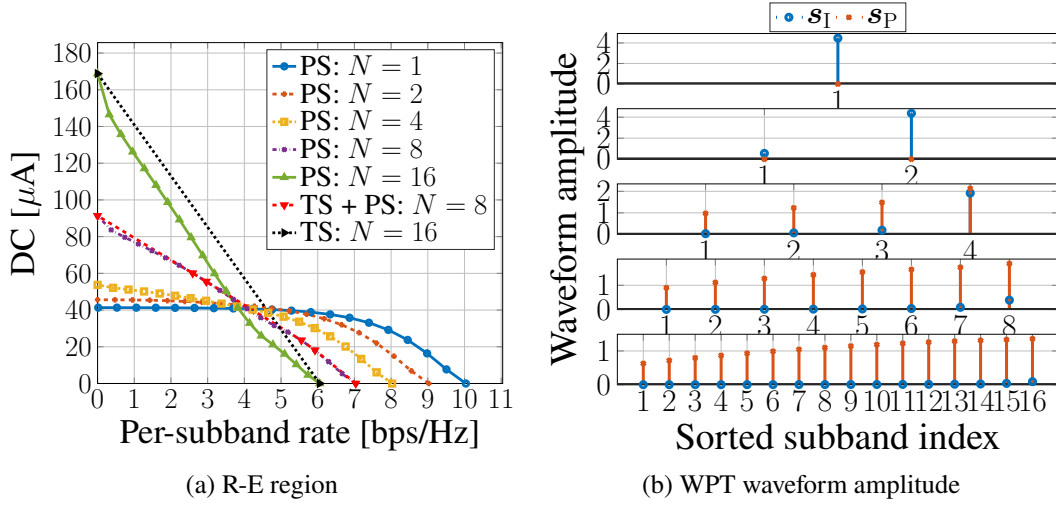
3.4.2.1 Number of Subbands

(a) R-E region

(b) WPT waveform amplitude

Fig. 3.5 Average R-E region and WPT waveform amplitude versus N for $M = 1$, $L = 20$, $\sigma_n^2 = -40\,\mathrm{dBm}$, $B = 1\,\mathrm{MHz}$ and $d_{\mathrm{H}} = d_{\mathrm{V}} = 2\,\mathrm{m}$.

Fig. 3.5(a) illustrates the average R-E region versus the number of subband N. First, it is observed that increasing N reduces the per-subband rate but boosts the harvested energy. This is because less power is allocated to each subband but more balanced DC terms are introduced by frequency coupling to boost the harvested energy. On the other hand, Fig. 3.5(b) presents the sorted modulated/multisine amplitude $\mathbf{s}_{\mathrm{I/P}}$ for WPT. It demonstrates that a dedicated multisine waveform is unnecessary for a small N but is required for a large N. This observation origins from the rectifier nonlinearity. Although both waveforms have equivalent second-order DC terms (3.9a) and (3.9c), for the fourth-order terms (3.9b) and (3.9d), the modulated waveform has N^2 monomials with a modulation gain of 2, while the multisine has $(2N^3 + N)/3$ monomials as the components of different frequencies compensate and produce DC. Second, the R-E region is convex for $N \in \{2, 4\}$ and concave-convex for $N \in \{8, 16\}$, such that PS outperforms TS for a small N and is outperformed for a large N. When N is in between, the optimal strategy is a combination of both, i.e., a time sharing between the WPT point and the saddle PS SWIPT point (as denoted by the red curve in Fig. 3.5(a)). When N is relatively small, only modulated waveform is used at both WIT and WPT points, and one can infer that no multisine waveform is needed for the entire R-E region. It aligns with the conclusion based on the conventional linear harvester model, namely the R-E region is convex, PS outperforms TS, and dedicated power waveform is unnecessary. As N becomes

sufficiently large, the multisine waveform further boosts WPT and creates some concavity in the high-power region, which accounts for the superiority of TS under the nonlinear harvester model. Therefore, we conclude that the rectifier nonlinearity enlarges the R-E region by favoring a different waveform and receiving mode, both heavily depending on N.
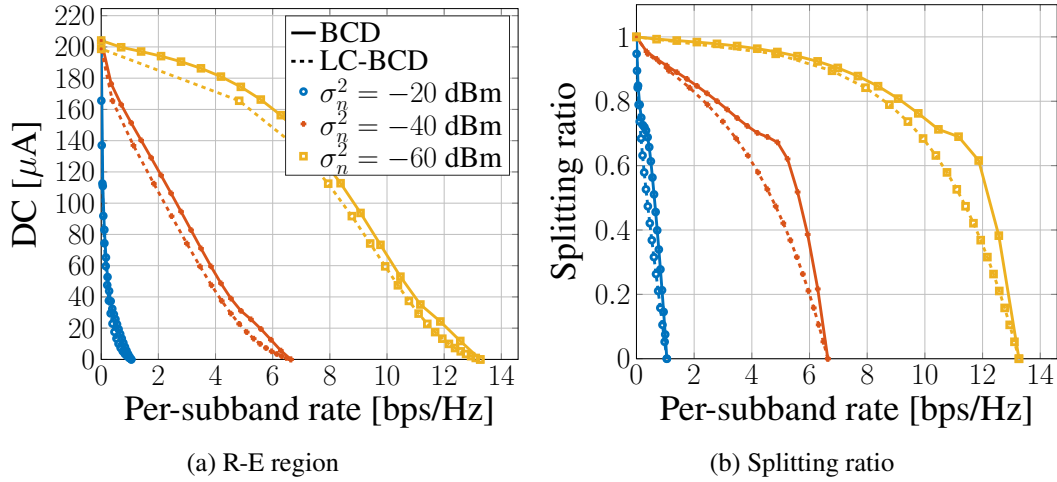
3.4.2.2 Average Noise Power

(a) R-E region   (b) Splitting ratio

Fig. 3.6 Average R-E region and splitting ratio versus σ_n^2 for $M = 1$, $N = 16$, $L = 20$, $B = 1\,\mathrm{MHz}$ and $d_\mathrm{H} = d_\mathrm{V} = 2\,\mathrm{m}$.

The average noise power influences the R-E region as shown in Fig. 3.6(a). First, we note that the R-E region is roughly concave/convex at low/high SNR such that TS/PS are preferred correspondingly. At low SNR, the power is allocated to the modulated waveform on a few strongest subbands to achieve a high rate. As the rate constraint $\bar{R}$ decreases, Algorithm 2 activates more subbands that further boosts the harvested DC power because of frequency coupling and harvester nonlinearity. Second, there exists a turning point in the R-E region, especially for a low noise level ($\sigma_n^2 \leq -40\,\mathrm{dBm}$). The reason is that when $\bar{R}$ departs slightly from the maximum value, the algorithm tends to adjust the splitting ratio ρ rather than allocate more power to the multisine waveform, since a small amplitude multisine could be inefficient for energy purpose. As $\bar{R}$ further decreases, thanks to the advantage of multisine, a superposed waveform with a small ρ can outperform a modulated waveform with a large ρ. The result proves the benefit of superposed waveform and the necessity of joint waveform and splitting ratio optimization. Besides, the LC-BCD algorithm achieves a good balance between performance and complexity even if one-dimensional search is considered for $\delta = \rho$ from 0 to 1.
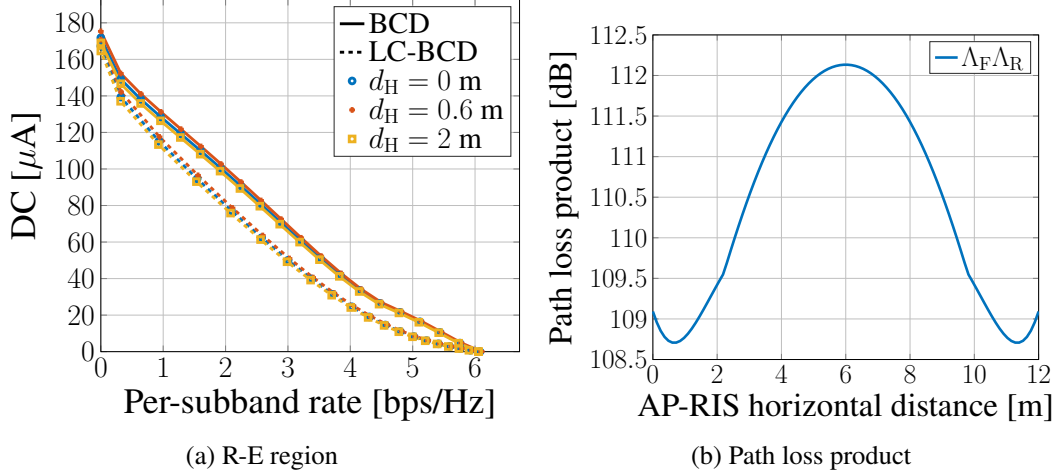
3.4.2.3 RIS Development

(a) R-E region

(b) Path loss product

Fig. 3.7 Average R-E region and path loss versus d_H for $M = 1$, $N = 16$, $L = 20$, $\sigma_n^2 = -40\,\text{dBm}$, $B = 1\,\text{MHz}$ and $d_V = 2\,\text{m}$.

In Fig. 3.7(a), we compare the average R-E region achieved by different AP-RIS horizontal distance d_H. Different from the active AF relay that favors midpoint development [131], the RIS should be placed close to either the AP or the UE based on the product path loss model that applies to finite-size element reflection [45, 132]. Moreover, there exist two optimal RIS coordinates around $d_H = 0.6$ and $11.4\,\text{m}$ that minimize the path loss product $\Lambda_F \Lambda_R$ and maximize the R-E trade-off. It suggests that equipping the AP with a RIS can potentially extend the operation range of SWIPT systems.

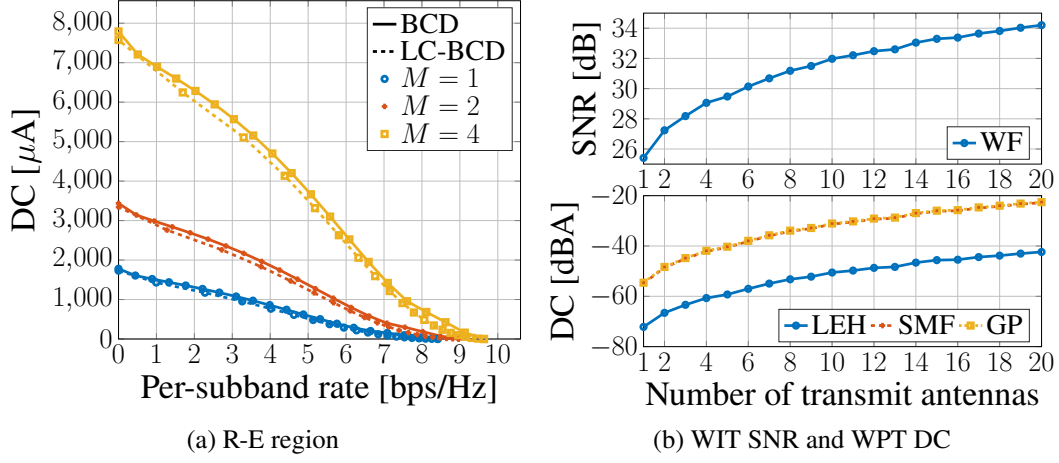### 3.4.2.4   Number of Transmit Antennas and RIS Elements

(a) R-E region   (b) WIT SNR and WPT DC

Fig. 3.8 Average R-E region, WIT SNR and WPT DC versus M for $N = 16$, $L = 20$, $\sigma_n^2 = -40\,\text{dBm}$, $B = 1\,\text{MHz}$, $d_{\text{H}} = d_{\text{V}} = 0.2\,\text{m}$.

(a) R-E region   (b) WIT SNR and WPT DC
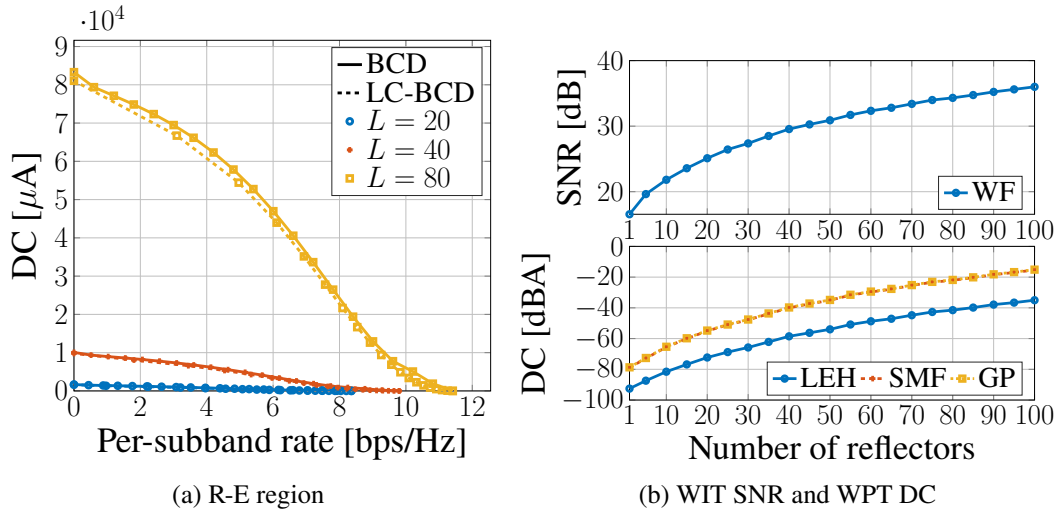
Fig. 3.9 Average R-E region, WIT SNR and WPT DC versus L for $M = 1$, $N = 16$, $\sigma_n^2 = -40\,\text{dBm}$, $B = 1\,\text{MHz}$ and $d_{\text{H}} = d_{\text{V}} = 0.2\,\text{m}$.

The impacts of the number of transmit antennas M and the RIS elements L on the R-E behavior are revealed in Figs. 3.8(a) and 3.9(a). First, it is observed that adding either active or passive elements can improve the equivalent SNR, which produces a nearly concave R-E region and favors the PS receiver. Second, the conventional Linear Energy Harvester (LEH) model leads to a power-inefficient design. To investigate the performance loss, we truncate the DC objective function (3.7) at $n_0 = 2$ such that (i) in the passive beamforming problem,

$z(\bar{\boldsymbol{\Theta}}) = \beta_2 \rho(t_{\mathrm{I},0} + t_{\mathrm{P},0})/2$ and no SCA is required; (ii) in the waveform design problem, the WPT-optimal strategy is the adaptive single sinewave that allocates all power to the multisine at the strongest subband [63]. As shown in Figs. 3.8(b) and 3.9(b), those conventional designs do not exploit the harvester nonlinearity and end up with a nearly $20\,\mathrm{dBA}$ gap compared to the nonlinear model-based SMF and GP designs. Third, doubling M brings a $3\,\mathrm{dB}$ gain at the output SNR and a $12\,\mathrm{dBA}$ increase at the harvested DC, which verified that active beamforming has an array gain of M [127] with power scaling order M^2 under the truncated nonlinear harvester model [63, 72]. Fourth, when the RIS is very close to the AP or UE, doubling L can bring a $6\,\mathrm{dB}$ gain at the output SNR and a $24\,\mathrm{dBA}$ increase at the harvested DC. From the perspective of WIT, it suggests that passive beamforming can reach an array gain of L^2, as indicated by [14]. An interpretation is that the RIS coherently combines the incoming signal with a receive array gain L, then performs an equal gain reflection with a transmit array gain L. From the perspective of WPT, it suggests that passive beamforming comes with a power scaling order L^4 under the truncated nonlinear harvester model. We then verify this novel observation in a simplified case where the power is uniformly allocated over multisine, all channels are frequency-flat, and L is sufficiently large such that the direct channel becomes negligible. Let X be the cascaded small-scale fading coefficient. The DC in such case reduces to

$$z = \beta_2 \Lambda_{\mathrm{B}}^2 \Lambda_{\mathrm{F}}^2 |X|^2 L^2 P + \beta_4 \frac{2N^2 + 1}{2N} \Lambda_{\mathrm{B}}^4 \Lambda_{\mathrm{F}}^4 |X|^4 L^4 P^2, \qquad (3.37)$$

which scales quartically with L. Compared with active antennas, RIS elements achieve higher array gain and power scaling order, but a very large L is required to compensate the double fading of the auxiliary link. These observations demonstrate the R-E benefit of passive beamforming and emphasize the importance of accounting for the harvester nonlinearity in the waveform and beamforming design.
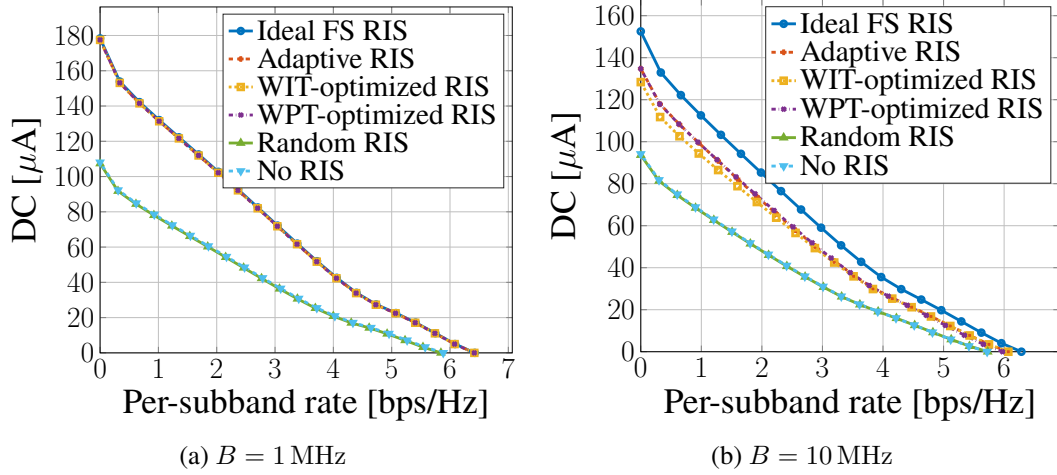
3.4.2.5 Bandwidth

(a) $B = 1\,\text{MHz}$

(b) $B = 10\,\text{MHz}$

Fig. 3.10 Average R-E region for ideal, adaptive, fixed and no RIS versus B for $M = 1$, $N = 16$, $L = 20$, $\sigma_n^2 = -40\,\text{dBm}$ and $d_\text{H} = d_\text{V} = 2\,\text{m}$.

Figs. 3.10(a) and 3.10(b) explore the R-E region with different RIS strategies for narrowband and broadband SWIPT. The ideal Frequency-Selective (FS) RIS assumes the reflection coefficient of each element is independent and controllable at different frequencies. The adaptive RIS adjusts the passive beamforming for different R-E points by Algorithm 1. The WIT/WPT-optimized RIS is retrieved by Algorithm 3 then fixed for the whole R-E region. The random RIS models the phase shift of all elements as i.i.d. uniform random variables over $[0, 2\pi)$. First, random RIS and no RIS perform worse than other schemes since no passive beamforming is exploited. Their R-E boundaries coincide as the antenna mode reflection of the random RIS is canceled out after averaging. Second, when the bandwidth is small, the performance of ideal, adaptive, and WIT/WPT-optimized RIS are similar; when the bandwidth is large, the adaptive RIS outperforms the WIT/WPT-optimized RIS but is outperformed by the ideal FS RIS. In the former case, the subband responses are close to each other such that the trade-off in Remark 2 becomes insignificant, and the auxiliary link can be roughly maximized at all subbands. It suggests that for narrowband SWIPT, the optimal passive beamforming for any R-E point is optimal for the whole R-E region, and the corresponding equivalent channel and active precoder are also optimal for the whole R-E region. Hence, the achievable R-E region is obtained by optimizing the waveform amplitude and splitting ratio. On the other hand, since the channel frequency selectivity affects the performance of the information decoder and energy harvester differently, the optimal RIS reflection coefficient varies at different R-E trade-offs points for broadband SWIPT. As shown in Fig. 3.4, the subchannel amplification can be either spread evenly to improve the rate at

high SNR, or focused on a few strongest subbands to boost the output DC, thanks to adaptive passive beamforming.
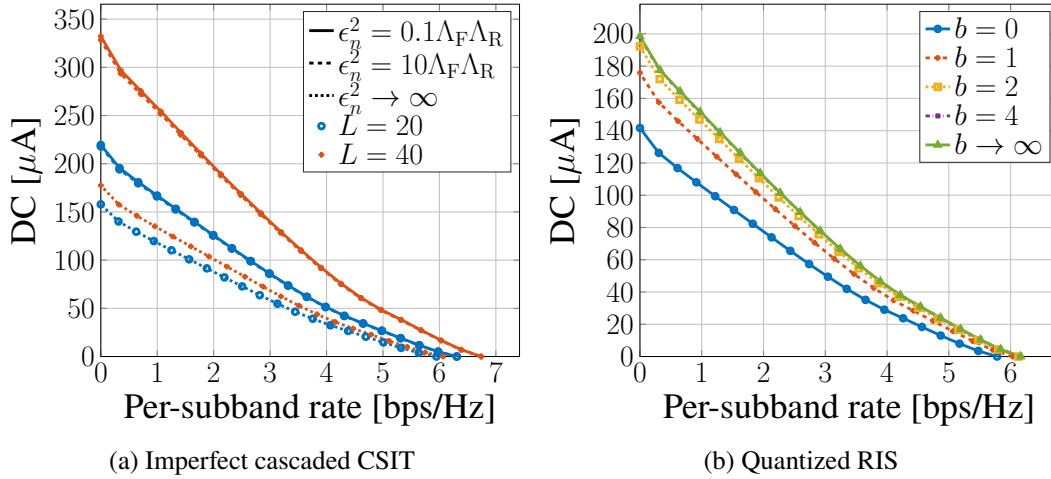
3.4.2.6 Imperfect CSIT

(a) Imperfect cascaded CSIT

(b) Quantized RIS

Fig. 3.11 Average R-E region with imperfect cascaded CSIT and quantized RIS for $M = 1$, $N = 16$, $L = 20$, $\sigma_n^2 = -40\,\text{dBm}$, $B = 10\,\text{MHz}$ and $d_{\text{H}} = d_{\text{V}} = 2\,\text{m}$. $\epsilon_n = 0$ and $\epsilon_n = \infty$ correspond respectively to perfect CSIT and no CSIT (and random RIS); $b = 0$ and $b \to \infty$ correspond respectively to no RIS and continuous RIS.

We then explore the impacts of imperfect cascaded CSIT and quantized RIS on the R-E performance. Due to the general lack of RF-chains at the RIS, it can be challenging to acquire accurate cascaded CSIT on a short-term basis. We assume the cascaded channel at subband n is

$$\mathbf{V}_n = \hat{\mathbf{V}}_n + \tilde{\mathbf{V}}_n, \tag{3.38}$$

where $\hat{\mathbf{V}}_n$ is the estimated cascaded CSIT and $\tilde{\mathbf{V}}_n$ is the estimation error with entries following i.i.d. CSCG distribution $\mathcal{CN}(0, \epsilon_n^2)$.[2] Figure 3.11(a) shows that the proposed passive beamforming Algorithm 1 is robust to cascaded CSIT inaccuracy for broadband SWIPT with different L. On the other hand, since the practical reflection coefficient depends on the available element impedances, we consider a discrete RIS codebook $\mathcal{C}_\phi = \{e^{j2\pi i/2^b} \mid i = 1, \ldots, 2^b\}$ and uniformly quantize the continuous reflection coefficients obtained by Algorithm 4 to reduce the circuit complexity and control overhead. This relax-then-quantize approach can bring notable performance loss compared with direct optimization over the discrete phase shift set, especially for a small b (i.e., low-resolution RIS) [133]. Figure 3.11(b) suggests that

---

[2]Note that the subchannel responses are correlated but the estimations can be independent.

even $b = 1$ (i.e., two-state reflection) brings considerable R-E gain over the benchmark scheme without RIS, and the performance gap between $b = 4$ and continuous RIS is negligible. These observations demonstrate the advantage of the proposed joint waveform, active and passive beamforming design in practical RIS-aided SWIPT systems.

3.5   Conclusion and Future Works

This chapter investigated the R-E trade-off of a single user employing practical receiving strategies in a RIS-aided multi-carrier MISO SWIPT system. Uniquely, we considered the joint waveform, active and passive beamforming design under rectifier nonlinearity to maximize the achievable R-E region. A three-stage BCD algorithm was proposed to solve the problem. In the first stage, the RIS phase shift was obtained by the SCA technique and eigen decomposition. In the second and third stages, the active precoder was derived in closed form, and the waveform amplitude and splitting ratio were optimized by the GP method. We also proposed and combined closed-form adaptive waveform schemes with a modified passive beamforming strategy to formulate a low-complexity BCD algorithm that achieves a good balance between performance and complexity. Numerical results revealed significant R-E gains by modeling harvester nonlinearity in the RIS-aided SWIPT design. Unlike active antennas, RIS elements cannot be designed independently across frequencies, but can integrate coherent combining and equal gain transmission to enable constructive reflection and flexible subchannel design. Compared to the conventional no-RIS system, the RIS mainly affects the effective channel instead of the waveform design.

One particular unanswered question of this chapter is how to design waveform, active and passive beamforming in a multi-user multi-carrier RIS-aided SWIPT system. Also, harvester saturation effect and practical RIS models with amplitude-phase coupling [47], angle-dependent reflection [132], frequency-dependent reflection, and/or partially/fully-connected architecture [2] could be considered in future works.

Chapter 4

Appendix

4.1 Proofs for Chapter 1

4.1.1 Proof of Proposition 1

For any feasible $\bar{\Theta}$ to problem (3.21), $\text{tr}(\bar{\Theta}) = L + 1$ always holds because of the modulus constraint (3.21c). Therefore, problem (3.21) can be recast as

$$\max_{\bar{\Theta}} \quad \tilde{z}(\bar{\Theta}) - \text{tr}(\bar{\Theta}) \tag{4.1a}$$

$$\text{s.t.} \quad R(\bar{\Theta}) \geq \bar{R}, \tag{4.1b}$$

$$\text{diag}^{-1}(\bar{\Theta}) = \mathbf{1}, \tag{4.1c}$$

$$\bar{\Theta} \succeq \mathbf{0}, \tag{4.1d}$$

$$\text{rank}(\bar{\Theta}) = 1. \tag{4.1e}$$

It is straightforward to verify the convex problem (4.1a)–(4.1d) satisfies the Slater's condition and strong duality holds [134]. The corresponding Lagrangian function at iteration r is

$$
\begin{aligned}
\mathcal{L} = {} & \mathrm{tr}\left(\bar{\boldsymbol{\Theta}}^{(r)}\right) - \frac{1}{2}\beta_2\rho\,\mathrm{tr}\left((\mathbf{C}_{\mathrm{I},0} + \mathbf{C}_{\mathrm{P},0})\bar{\boldsymbol{\Theta}}^{(r)}\right) \\
& - \frac{3}{4}\beta_4\rho^2\left(2t_{\mathrm{I},0}^{(r-1)}\mathrm{tr}\left(\mathbf{C}_{\mathrm{I},0}\bar{\boldsymbol{\Theta}}^{(r)}\right) + \sum_{k=-N+1}^{N-1}(t_{\mathrm{P},k}^{(r-1)})^*\mathrm{tr}\left(\mathbf{C}_{\mathrm{P},k}\bar{\boldsymbol{\Theta}}^{(r)}\right)\right. \\
& \left. + 2t_{\mathrm{P},0}^{(r-1)}\mathrm{tr}\left(\mathbf{C}_{\mathrm{I},0}\bar{\boldsymbol{\Theta}}^{(r)}\right) + 2t_{\mathrm{I},0}^{(r-1)}\mathrm{tr}\left(\mathbf{C}_{\mathrm{P},0}\bar{\boldsymbol{\Theta}}^{(r)}\right)\right) \\
& + \mu\left(2^{\bar{R}} - \prod_{n=1}^{N}\left(1 + \frac{(1-\rho)\mathrm{tr}\left(\mathbf{C}_n\bar{\boldsymbol{\Theta}}^{(r)}\right)}{\sigma_n^2}\right)\right) \\
& + \mathrm{tr}\left(\mathrm{diag}(\nu)\odot\left(\bar{\boldsymbol{\Theta}}^{(r)}\odot\mathbf{I} - \mathbf{I}\right)\right) - \mathrm{tr}\left(\boldsymbol{\Upsilon}\bar{\boldsymbol{\Theta}}^{(r)}\right) + \zeta,
\end{aligned}
\tag{4.2}
$$

where μ, ν, $\boldsymbol{\Upsilon}$ denote respectively the scalar, vector and matrix Lagrange multiplier associated with constraint (4.1b), (4.1c) and (4.1d), and ζ collects all terms irrelevant to $\bar{\boldsymbol{\Theta}}^{(r)}$. The Karush-Kuhn-Tucker (KKT) conditions on the primal and dual solutions are

$$
\mu^\star \geq 0,\ \boldsymbol{\Upsilon}^\star \succeq \mathbf{0},
\tag{4.3a}
$$

$$
\nu^\star \odot \mathrm{diag}^{-1}(\bar{\boldsymbol{\Theta}}^\star) = \mathbf{0},\ \boldsymbol{\Upsilon}^\star\bar{\boldsymbol{\Theta}}^\star = \mathbf{0},
\tag{4.3b}
$$

$$
\nabla_{\bar{\boldsymbol{\Theta}}^\star}\mathcal{L} = 0.
\tag{4.3c}
$$

We then express (4.3c) explicitly as $\boldsymbol{\Upsilon}^\star = \mathbf{I} - \boldsymbol{\Delta}^\star$, where

$$
\begin{aligned}
\boldsymbol{\Delta}^\star = {} & \frac{1}{2}\beta_2\rho(\mathbf{C}_{\mathrm{I},0} + \mathbf{C}_{\mathrm{P},0}) \\
& + \frac{3}{4}\beta_4\rho^2\left(2t_{\mathrm{I},0}^{(r-1)}\mathbf{C}_{\mathrm{I},0} + \sum_{k=-N+1}^{N-1}(t_{\mathrm{P},k}^{(r-1)})^*\mathbf{C}_{\mathrm{P},k} + 2t_{\mathrm{P},0}^{(r-1)}\mathbf{C}_{\mathrm{I},0} + 2t_{\mathrm{I},0}^{(r-1)}\mathbf{C}_{\mathrm{P},0}\right) \\
& + \mu^\star\sum_{n=1}^{N}\frac{(1-\rho)\mathbf{C}_n}{\sigma_n^2}\prod_{n'=1,n'\neq n}^{N}\left(1 + \frac{(1-\rho)\mathrm{tr}\left(\mathbf{C}_{n'}\bar{\boldsymbol{\Theta}}^\star\right)}{\sigma_{n'}^2}\right) - \mathrm{diag}(\nu^\star).
\end{aligned}
\tag{4.4}
$$

Note that (4.3b) suggests $\mathrm{rank}(\boldsymbol{\Upsilon}^\star) + \mathrm{rank}(\bar{\boldsymbol{\Theta}}^\star) \leq L + 1$. By reusing the proof in [135, Appendix A], we conclude $\mathrm{rank}(\boldsymbol{\Upsilon}^\star) \geq L$. On the other hand, $\bar{\boldsymbol{\Theta}}^\star$ cannot be $\mathbf{0}$ and $\mathrm{rank}(\bar{\boldsymbol{\Theta}}^\star) \geq 1$. Therefore, any optimal solution $\bar{\boldsymbol{\Theta}}^\star$ to the relaxed problem (4.1) must be rank-1. Due to the equivalence between (3.21a) and (4.1a), $\bar{\boldsymbol{\Theta}}^\star$ is also optimal to the relaxed problem (3.21). The proof is completed.

4.1.2 Proof of Proposition 2

The objective function (3.21a) is non-decreasing over iterations because the solution to (3.21a)–(3.21d) at iteration $r-1$ is still feasible at iteration r. As $r \to \infty$, $\tilde{z}(\bar{\Theta}^{(r)})$ is bounded above because of the unit-modulus constraint (3.21c). Thus, Algorithm 1 is guaranteed to converge. Besides, we notice that Algorithm 1 is an inner approximation algorithm [136], because $\tilde{z}(\bar{\Theta}) \leq z(\bar{\Theta})$, $\partial \tilde{z}(\bar{\Theta}^{(r)})/\partial\bar{\Theta} = \partial z(\bar{\Theta}^{(r)})/\partial\bar{\Theta}$ and the approximation (3.16)–(3.18) are asymptotically tight as $r \to \infty$ [137]. Therefore, it is guaranteed to provide a local optimal $\bar{\Theta}^{\star}$ to the relaxed passive beamforming problem. According to Proposition 1, $\bar{\Theta}^{\star}$ is rank-1 such that $\theta^{\star}$ can be extracted without performance loss and the local optimality inherits to the original problem (3.11).

4.1.3 Proof of Proposition 3

From the perspective of WIT, the MRT precoder (3.23) maximizes $|\mathbf{h}_n^{\mathsf{H}}\mathbf{w}_{\mathrm{I},n}| = \|\mathbf{h}_n\|s_{\mathrm{I},n}$ and thus the rate (3.6). From the perspective of WPT, the MRT precoder (3.23) maximizes $(\mathbf{h}_n^{\mathsf{H}}\mathbf{w}_{\mathrm{I/P},n})(\mathbf{h}_n^{\mathsf{H}}\mathbf{w}_{\mathrm{I/P},n})^* = \|\mathbf{h}_n\|^2 s_{\mathrm{I/P},n}^2$ and thus the second and fourth order DC terms (3.9a)–(3.9d). Therefore, the global optimal information and power precoders coincide at MRT.

References

[1] Q. Wu and R. Zhang, "Towards smart and reconfigurable environment: Intelligent reflecting surface aided wireless network," *IEEE Communications Magazine*, vol. 58, pp. 106–112, 1 2020.

[2] S. Shen, B. Clerckx, and R. Murch, "Modeling and architecture design of reconfigurable intelligent surfaces using scattering parameter network analysis," *IEEE Transactions on Wireless Communications*, pp. 1–1, Nov. 2021.

[3] C. E. Shannon, "A mathematical theory of communication," *Bell System Technical Journal*, vol. 27, pp. 379–423, Jul 1948.

[4] F. Tariq, M. R. A. Khandaker, K.-K. Wong, M. A. Imran, M. Bennis, and M. Debbah, "A speculative study on 6g," *IEEE Wireless Communications*, vol. 27, pp. 118–125, 8 2020.

[5] D. Georgiev, "Internet of things statistics, facts & predictions [2024's update]," https://review42.com/resources/internet-of-things-stats/, accessed: 2024-03-13.

[6] M. Shafi, A. F. Molisch, P. J. Smith, T. Haustein, P. Zhu, P. D. Silva, F. Tufvesson, A. Benjebbour, and G. Wunder, "5g: A tutorial overview of standards, trials, challenges, deployment, and practice," *IEEE Journal on Selected Areas in Communications*, vol. 35, pp. 1201–1221, 6 2017.

[7] H. Tataria, M. Shafi, A. F. Molisch, M. Dohler, H. Sjoland, and F. Tufvesson, "6g wireless systems: Vision, requirements, challenges, insights, and opportunities," *Proceedings of the IEEE*, vol. 109, pp. 1166–1199, 7 2021.

[8] M. Alsabah, M. A. Naser, B. M. Mahmmod, S. H. Abdulhussain, M. R. Eissa, A. Al-Baidhani, N. K. Noordin, S. M. Sait, K. A. Al-Utaibi, and F. Hashim, "6g wireless communications networks: A comprehensive survey," *IEEE Access*, vol. 9, pp. 148 191–148 243, 2021.

[9] W. Jiang, B. Han, M. A. Habibi, and H. D. Schotten, "The road towards 6g: A comprehensive survey," *IEEE Open Journal of the Communications Society*, vol. 2, pp. 334–366, 2021.

[10] L. Dai, B. Wang, M. Wang, X. Yang, J. Tan, S. Bi, S. Xu, F. Yang, Z. Chen, M. D. Renzo, C.-B. Chae, and L. Hanzo, "Reconfigurable intelligent surface-based wireless communications: Antenna design, prototyping, and experimental results," *IEEE Access*, vol. 8, pp. 45 913–45 923, 2020.

[11] P. Nayeri, F. Yang, and A. Z. Elsherbeni, *Reflectarray Antennas: Theory, Designs, and Applications.* Wiley, 2 2018.

[12] R. Anwar, L. Mao, and H. Ning, "Frequency selective surfaces: A review," *Applied Sciences*, vol. 8, no. 9, p. 1689, Sep. 2018.

[13] Q. Wu, X. Zhou, and R. Schober, "IRS-assisted wireless powered NOMA: Do we really need different phase shifts in DL and UL?" *IEEE Wireless Communications Letters*, vol. 10, pp. 1493–1497, Jul 2021.

[14] Q. Wu and R. Zhang, "Intelligent reflecting surface enhanced wireless network via joint active and passive beamforming," *IEEE Transactions on Wireless Communications*, vol. 18, pp. 5394–5409, Nov 2019.

[15] T. Jiang and W. Yu, "Interference nulling using reconfigurable intelligent surface," *IEEE Journal on Selected Areas in Communications*, vol. 40, pp. 1392–1406, 5 2022.

[16] G. Ghatak, V. Malik, S. S. Kalamkar, and A. K. Gupta, "Where to deploy reconfigurable intelligent surfaces in the presence of blockages?" vol. 2021-September. IEEE, 9 2021, pp. 1419–1424.

[17] S. Zeng, H. Zhang, B. Di, Z. Han, and L. Song, "Reconfigurable intelligent surface (ris) assisted wireless coverage extension: Ris orientation and location optimization," *IEEE Communications Letters*, vol. 25, pp. 269–273, 1 2021.

[18] A. Almohamad, A. M. Tahir, A. Al-Kababji, H. M. Furqan, T. Khattab, M. O. Hasna, and H. Arslan, "Smart and secure wireless communications via reflecting intelligent surfaces: A short survey," *IEEE Open Journal of the Communications Society*, vol. 1, pp. 1442–1456, 2020.

[19] J. Ye, S. Guo, S. Dang, B. Shihada, and M.-S. Alouini, "On the capacity of reconfigurable intelligent surface assisted mimo symbiotic communications," *IEEE Transactions on Wireless Communications*, vol. 21, pp. 1943–1959, 3 2022.

[20] E. Basar, "Reconfigurable intelligent surfaces for doppler effect and multipath fading mitigation," *Frontiers in Communications and Networks*, vol. 2, 5 2021.

[21] E. Arslan, I. Yildirim, F. Kilinc, and E. Basar, "Over-the-air equalization with reconfigurable intelligent surfaces," *IET Communications*, vol. 16, pp. 1486–1497, 8 2022.

[22] O. Ozdogan, E. Bjornson, and E. G. Larsson, "Using intelligent reflecting surfaces for rank improvement in mimo communications." IEEE, 5 2020, pp. 9160–9164.

[23] Y. Yang, B. Zheng, S. Zhang, and R. Zhang, "Intelligent reflecting surface meets ofdm: Protocol design and rate maximization," *IEEE Transactions on Communications*, vol. 68, pp. 4522–4535, 7 2020.

[24] G. Chen and Q. Wu, "Fundamental limits of intelligent reflecting surface aided multiuser broadcast channel," *IEEE Transactions on Communications*, vol. 71, pp. 5904–5919, 10 2023.

[25] R. Liu, Q. Wu, M. D. Renzo, and Y. Yuan, "A path to smart radio environments: An industrial viewpoint on reconfigurable intelligent surfaces," *IEEE Wireless Communications*, vol. 29, pp. 202–208, 2 2022.

[26] R. Alliance, "Reconfigurable intelligent surface technology white paper," 2023.

[27] ITU-R, "Future technology trends of terrestrial international mobile telecommunications systems towards 2030 and beyond," Report ITU-R M.2516-0, 2022.

[28] Y. Zhao, B. Clerckx, and Z. Feng, "IRS-aided SWIPT: Joint waveform, active and passive beamforming design under nonlinear harvester model," *IEEE Transactions on Communications*, vol. 70, pp. 1345–1359, 2022.

[29] Y. Zhao and B. Clerckx, "Riscatter: Unifying backscatter communication and reconfigurable intelligent surface," 12 2022.

[30] ——, *RIS in Wireless Information and Power Transfer*. John Wiley & Sons, Ltd, 2023, pp. 271–295.

[31] Y. Zhao, H. Li, M. Franceschetti, and B. Clerckx, "Channel shaping using reconfigurable intelligent surfaces: From diagonal to beyond," *To be submitted to IEEE Transactions on Wireless Communications*.

[32] V. G. Veselago, "The electrodynamics of substances with negative ϵ and μ," *Soviet Physics Uspekhi*, vol. 10, pp. 509–514, 4 1968.

[33] J. Pendry, A. Holden, D. Robbins, and W. Stewart, "Magnetism from conductors and enhanced nonlinear phenomena," *IEEE Transactions on Microwave Theory and Techniques*, vol. 47, pp. 2075–2084, 1999.

[34] N. Yu, P. Genevet, M. A. Kats, F. Aieta, J.-P. Tetienne, F. Capasso, and Z. Gaburro, "Light propagation with phase discontinuities: Generalized laws of reflection and refraction," *Science*, vol. 334, pp. 333–337, 10 2011.

[35] J. Pendry, "Negative refraction," *Contemporary Physics*, vol. 45, pp. 191–202, 5 2004.

[36] T. J. Cui, M. Q. Qi, X. Wan, J. Zhao, and Q. Cheng, "Coding metamaterials, digital metamaterials and programmable metamaterials," *Light: Science & Applications*, vol. 3, no. 10, pp. e218–e218, Oct. 2014.

[37] Q. Ma, G. D. Bai, H. B. Jing, C. Yang, L. Li, and T. J. Cui, "Smart metasurface with self-adaptively reprogrammable functions," *Light: Science & Applications*, vol. 8, p. 98, 10 2019.

[38] W. J. Padilla, D. N. Basov, and D. R. Smith, "Negative refractive index metamaterials," *Materials Today*, vol. 9, pp. 28–35, 7 2006.

[39] M. Poulakis, "6g's metamaterials solution: There's plenty of bandwidth available if we use reconfigurable intelligent surfaces," *IEEE Spectrum*, vol. 59, pp. 40–45, 11 2022.

[40] Y. C. Liang, Q. Zhang, J. Wang, R. Long, H. Zhou, and G. Yang, "Backscatter communication assisted by reconfigurable intelligent surfaces," *Proceedings of the IEEE*, 2022.

[41] R. Hansen, "Relationships between antennas as scatterers and as radiators," *Proceedings of the IEEE*, vol. 77, pp. 659–662, May 1989.

[42] S. J. Thomas and M. S. Reynolds, "A 96 mbit/sec, 15.5 pj/bit 16-qam modulator for uhf backscatter communication." IEEE, Apr 2012, pp. 185–190.

[43] Y.-C. Liang, Q. Zhang, E. G. Larsson, and G. Y. Li, "Symbiotic radio: Cognitive backscattering communications for future wireless networks," *IEEE Transactions on Cognitive Communications and Networking*, vol. 6, pp. 1242–1255, Dec 2020.

[44] C. Boyer and S. Roy, "Backscatter communication and RFID: Coding, energy, and MIMO analysis," *IEEE Transactions on Communications*, vol. 62, pp. 770–785, Mar 2014.

[45] O. Ozdogan, E. Bjornson, and E. G. Larsson, "Intelligent reflecting surfaces: Physics, propagation, and pathloss modeling," *IEEE Wireless Communications Letters*, vol. 9, no. 5, pp. 581–585, May 2020.

[46] M. Najafi, V. Jamali, R. Schober, and H. V. Poor, "Physics-based modeling and scalable optimization of large intelligent reflecting surfaces," *IEEE Transactions on Communications*, vol. 69, pp. 2673–2691, 4 2021.

[47] S. Abeywickrama, R. Zhang, and C. Yuen, "Intelligent reflecting surface: Practical phase shift model and beamforming optimization," in *ICC 2020 - 2020 IEEE International Conference on Communications (ICC)*. IEEE, Jun. 2020, pp. 1–6.

[48] Q. Wu and R. Zhang, "Intelligent reflecting surface enhanced wireless network: Joint active and passive beamforming design," vol. 18. IEEE, Dec 2018, pp. 1–6.

[49] M. T. Ivrlac and J. A. Nossek, "Toward a circuit theory of communication," *IEEE Transactions on Circuits and Systems I: Regular Papers*, vol. 57, pp. 1663–1683, 7 2010.

[50] H.-R. Ahn, *Asymmetric Passive Components in Microwave Integrated Circuits*. Wiley, 2006.

[51] M. Nerini, S. Shen, H. Li, and B. Clerckx, "Beyond diagonal reconfigurable intelligent surfaces utilizing graph theory: Modeling, architecture design, and optimization," 5 2023.

[52] X. Mu, Y. Liu, L. Guo, J. Lin, and R. Schober, "Simultaneously transmitting and reflecting (star) ris aided wireless communications," *IEEE Transactions on Wireless Communications*, vol. 21, pp. 3083–3098, 5 2022.

[53] Y. Liu, X. Mu, J. Xu, R. Schober, Y. Hao, H. V. Poor, and L. Hanzo, "Star: Simultaneous transmission and reflection for 360° coverage by intelligent surfaces," *IEEE Wireless Communications*, vol. 28, pp. 102–109, 12 2021.

[54] H. Li, S. Shen, and B. Clerckx, "Beyond diagonal reconfigurable intelligent surfaces: A multi-sector mode enabling highly directional full-space wireless coverage," *IEEE Journal on Selected Areas in Communications*, vol. 41, pp. 2446–2460, 8 2023.

[55] J. Koomey, S. Berard, M. Sanchez, and H. Wong, "Implications of historical trends in the electrical efficiency of computing," *IEEE Annals of the History of Computing*, vol. 33, pp. 46–54, 3 2011.

[56] J. Huang, Y. Zhou, Z. Ning, and H. Gharavi, "Wireless power transfer and energy harvesting: Current status and future prospects," *IEEE Wireless Communications*, vol. 26, pp. 163–169, 8 2019.

[57] X. Hao, H. Zhang, Z. Shen, Z. Liu, L. Zhang, H. Jiang, J. Liu, and H. Liao, "A 43.2 μW 2.4 ghz 64-qam pseudo-backscatter modulator based on integrated directional coupler." IEEE, 5 2018, pp. 1–5.

[58] R. Correia and N. B. Carvalho, "Ultrafast backscatter modulator with low-power consumption and wireless power transmission capabilities," *IEEE Microwave and Wireless Components Letters*, vol. 27, pp. 1152–1154, 12 2017.

[59] J. Zhou, P. Zhang, J. Han, L. Li, and Y. Huang, "Metamaterials and metasurfaces for wireless power transfer and energy harvesting," *Proceedings of the IEEE*, vol. 110, pp. 31–55, 1 2022.

[60] J. Joung, C. K. Ho, K. Adachi, and S. Sun, "A survey on power-amplifier-centric techniques for spectrum- and energy-efficient wireless communications," *IEEE Communications Surveys & Tutorials*, vol. 17, pp. 315–333, 1 2015.

[61] A. Alizadeh, S. Hassanzadehyamchi, A. Medi, and S. Kiaei, "An x-band class-j power amplifier with active load modulation to boost drain efficiency," *IEEE Transactions on Circuits and Systems I: Regular Papers*, vol. 67, pp. 3364–3377, 10 2020.

[62] N. M. L. Tan, T. Abe, and H. Akagi, "Design and performance of a bidirectional isolated dc-dc converter for a battery energy storage system," *IEEE Transactions on Power Electronics*, vol. 27, pp. 1237–1248, 3 2012.

[63] B. Clerckx and E. Bayguzina, "Waveform design for wireless power transfer," *IEEE Transactions on Signal Processing*, vol. 64, no. 23, pp. 6313–6328, Dec. 2016.

[64] C. R. Valenta and G. D. Durgin, "Harvesting wireless power: Survey of energy-harvester conversion efficiency in far-field, wireless power transfer systems," *IEEE Microwave Magazine*, vol. 15, pp. 108–120, 6 2014.

[65] S. A. Rotenberg, S. K. Podilchak, P. D. H. Re, C. Mateo-Segura, G. Goussetis, and J. Lee, "Efficient rectifier for wireless power transmission systems," *IEEE Transactions on Microwave Theory and Techniques*, vol. 68, pp. 1921–1932, 5 2020.

[66] E. Boshkovska, D. W. K. Ng, N. Zlatanov, and R. Schober, "Practical non-linear energy harvesting model and resource allocation for swipt systems," *IEEE Communications Letters*, vol. 19, pp. 2082–2085, 12 2015.

[67] Y. Zeng, B. Clerckx, and R. Zhang, "Communications and signals design for wireless power transmission," *IEEE Transactions on Communications*, vol. 65, pp. 2264–2290, 5 2017.

[68] M. D. Prete, A. Costanzo, M. Magno, D. Masotti, and L. Benini, "Optimum excitations for a dual-band microwatt wake-up radio," *IEEE Transactions on Microwave Theory and Techniques*, vol. 64, pp. 4731–4739, 12 2016.

[69] Y. Huang and B. Clerckx, "Large-scale multiantenna multisine wireless power transfer," *IEEE Transactions on Signal Processing*, vol. 65, pp. 5812–5827, 11 2017.

[70] S. Shen and B. Clerckx, "Beamforming optimization for mimo wireless power transfer with nonlinear energy harvesting: Rf combining versus dc combining," *IEEE Transactions on Wireless Communications*, vol. 20, pp. 199–213, 1 2021.

[71] L. R. Varshney, "Transporting information and energy simultaneously," in *2008 IEEE International Symposium on Information Theory*. IEEE, Jul. 2008, pp. 1612–1616.

[72] B. Clerckx, "Wireless information and power transfer: Nonlinearity, waveform design, and rate-energy tradeoff," *IEEE Transactions on Signal Processing*, vol. 66, no. 4, pp. 847–862, Feb. 2018.

[73] B. Clerckx, R. Zhang, R. Schober, D. W. K. Ng, D. I. Kim, and H. V. Poor, "Fundamentals of wireless information and power transfer: From RF energy harvester models to signal and system designs," *IEEE Journal on Selected Areas in Communications*, vol. 37, no. 1, pp. 4–33, Jan. 2019.

[74] T. M. Cover and J. A. Thomas, *Elements of Information Theory*. Wiley, 9 2005.

[75] M. Trotter, J. Griffin, and G. Durgin, "Power-optimized waveforms for improving the range and reliability of RFID systems," in *2009 IEEE International Conference on RFID*. IEEE, Apr. 2009, pp. 80–87.

[76] Q. Wu, X. Guan, and R. Zhang, "Intelligent reflecting surface-aided wireless energy and information transmission: An overview," *Proceedings of the IEEE*, vol. 110, pp. 150–170, 1 2022.

[77] X. Lu, P. Wang, D. Niyato, D. I. Kim, and Z. Han, "Wireless networks with rf energy harvesting: A contemporary survey," *IEEE Communications Surveys & Tutorials*, vol. 17, pp. 757–789, 2015.

[78] B. Clerckx, J. Kim, K. W. Choi, and D. I. Kim, "Foundations of wireless information and power transfer: Theory, prototypes, and experiments," *Proceedings of the IEEE*, vol. 110, pp. 8–30, 1 2022.

[79] J. Kim and B. Clerckx, "Wireless information and power transfer for IoT: Pulse position modulation, integrated receiver, and experimental validation," *IEEE Internet of Things Journal*, vol. 9, pp. 12 378–12 394, Jul 2022.

[80] H. Stockman, "Communication by means of reflected power," *Proceedings of the IRE*, vol. 36, pp. 1196–1204, 10 1948.

[81] J. Landt, "The history of RFID," *IEEE Potentials*, vol. 24, pp. 8–11, Oct 2005.

[82] Q. H. Abbasi, H. T. Abbas, A. Alomainy, and M. A. Imran, *Backscattering and RF Sensing for Future Wireless Communication*. Wiley, 6 2021.

[83] G. Yang, C. K. Ho, and Y. L. Guan, "Multi-antenna wireless energy transfer for backscatter communication systems," *IEEE Journal on Selected Areas in Communications*, vol. 33, pp. 2974–2987, Dec 2015.

[84] C. Chen, G. Wang, H. Guan, Y.-C. Liang, and C. Tellambura, "Transceiver design and signal detection in backscatter communication systems with multiple-antenna tags," *IEEE Transactions on Wireless Communications*, vol. 19, pp. 3273–3288, 5 2020.

[85] E. Goudeli, C. Psomas, and I. Krikidis, "Spatial-modulation-based techniques for backscatter communication systems," *IEEE Internet of Things Journal*, vol. 7, pp. 10 623–10 634, 10 2020.

[86] W. Liu, S. Shen, D. H. K. Tsang, and R. Murch, "Enhancing ambient backscatter communication utilizing coherent and non-coherent space-time codes," *IEEE Transactions on Wireless Communications*, vol. 20, pp. 6884–6897, 10 2021.

[87] C. He, S. Chen, H. Luan, X. Chen, and Z. J. Wang, "Monostatic mimo backscatter communications," *IEEE Journal on Selected Areas in Communications*, vol. 38, pp. 1896–1909, 8 2020.

[88] X. Wang, H. Yigitler, R. Duan, E. Y. Menta, and R. Jantti, "Coherent multi-antenna receiver for bpsk-modulated ambient backscatter tags," *IEEE Internet of Things Journal*, vol. 4662, pp. 1–1, 2021.

[89] J. K. Devineni and H. S. Dhillon, "Non-coherent detection and bit error rate for an ambient backscatter link in time-selective fading," *IEEE Transactions on Communications*, vol. 69, pp. 602–618, 1 2021.

[90] S. J. Thomas, E. Wheeler, J. Teizer, and M. S. Reynolds, "Quadrature amplitude modulated backscatter in passive and semipassive UHF RFID systems," *IEEE Transactions on Microwave Theory and Techniques*, vol. 60, pp. 1175–1182, Apr 2012.

[91] P. Zhang, D. Bharadia, K. Joshi, and S. Katti, "Hitchhike: Practical backscatter using commodity wifi." ACM, 11 2016, pp. 259–271.

[92] V. Iyer, V. Talla, B. Kellogg, S. Gollakota, and J. Smith, "Inter-technology backscatter: Towards internet connectivity for implanted devices vikram." ACM, 8 2016, pp. 356–369.

[93] B. Kellogg, V. Talla, J. R. Smith, and S. Gollakot, "Passive wi-fi: Bringing low power to wi-fi transmissions," *GetMobile: Mobile Computing and Communications*, vol. 20, pp. 38–41, 1 2017.

[94] J. F. Ensworth and M. S. Reynolds, "Ble-backscatter: Ultralow-power iot nodes compatible with bluetooth 4.0 low energy (ble) smartphones and tablets," *IEEE Transactions on Microwave Theory and Techniques*, vol. 65, pp. 3360–3368, 9 2017.

[95] V. Talla, M. Hessar, B. Kellogg, A. Najafi, J. R. Smith, and S. Gollakota, "Lora backscatter: Enabling the vision of ubiquitous connectivity," *Proceedings of the ACM on Interactive, Mobile, Wearable and Ubiquitous Technologies*, vol. 1, pp. 1–24, 9 2017.

[96] D. T. Hoang, D. Niyato, D. I. Kim, T. Kim, N. V. Huynh, and S. Gong, *Ambient Backscatter Communication Networks*. Cambridge University Press, 2020.

[97] V. Liu, A. Parks, V. Talla, S. Gollakota, D. Wetherall, and J. R. Smith, "Ambient backscatter: Wireless communication out of thin air," *ACM SIGCOMM Computer Communication Review*, vol. 43, pp. 39–50, Sep 2013.

[98] H. Guo, Y.-C. Liang, R. Long, and Q. Zhang, "Cooperative ambient backscatter system: A symbiotic radio paradigm for passive IoT," *IEEE Wireless Communications Letters*, vol. 8, pp. 1191–1194, Aug 2019.

[99] X. Zhou, R. Zhang, and C. K. Ho, "Wireless information and power transfer: Architecture design and rate-energy tradeoff," *IEEE Transactions on Communications*, vol. 61, no. 11, pp. 4754–4767, Nov. 2013.

[100] R. Zhang and C. K. Ho, "MIMO broadcasting for simultaneous wireless information and power transfer," *IEEE Transactions on Wireless Communications*, vol. 12, no. 5, pp. 1989–2001, May 2013.

[101] J. Park and B. Clerckx, "Joint wireless information and energy transfer in a k-user MIMO interference channel," *IEEE Transactions on Wireless Communications*, vol. 13, no. 10, pp. 5781–5796, Oct. 2014.

[102] B. Clerckx and J. Kim, "On the beneficial roles of fading and transmit diversity in wireless power transfer with nonlinear energy harvesting," *IEEE Transactions on Wireless Communications*, vol. 17, no. 11, pp. 7731–7743, Nov. 2018.

[103] J. Kim, B. Clerckx, and P. D. Mitcheson, "Experimental analysis of harvested energy and throughput trade-off in a realistic SWIPT system," in *2019 IEEE Wireless Power Transfer Conference (WPTC)*. IEEE, Jun. 2019, pp. 1–5.

[104] ——, "Signal and system design for wireless power transfer: Prototype, experiment and validation," *IEEE Transactions on Wireless Communications*, vol. 19, no. 11, pp. 7453–7469, Nov. 2020.

[105] J. Kim and B. Clerckx, "Range expansion for wireless power transfer using joint beamforming and waveform architecture: An experimental study in indoor environment," *IEEE Wireless Communications Letters*, vol. 10, no. 6, pp. 1237–1241, Jun. 2021.

[106] B. Clerckx and E. Bayguzina, "Low-complexity adaptive multisine waveform design for wireless power transfer," *IEEE Antennas and Wireless Propagation Letters*, vol. 16, no. 1, pp. 2207–2210, 2017.

[107] J. Kim, B. Clerckx, and P. D. Mitcheson, "Prototyping and experimentation of a closed-loop wireless power transmission with channel acquisition and waveform optimization," in *2017 IEEE Wireless Power Transfer Conference (WPTC)*. IEEE, May 2017, pp. 1–4.

[108] M. Varasteh, B. Rassouli, and B. Clerckx, "On capacity-achieving distributions for complex AWGN channels under nonlinear power constraints and their applications to SWIPT," *IEEE Transactions on Information Theory*, vol. 66, no. 10, pp. 6488–6508, Oct. 2020.

[109] ——, "SWIPT signaling over frequency-selective channels with a nonlinear energy harvester: Non-zero mean and asymmetric inputs," *IEEE Transactions on Communications*, vol. 67, no. 10, pp. 7195–7210, Oct. 2019.

[110] M. Varasteh, J. Hoydis, and B. Clerckx, "Learning to communicate and energize: Modulation, coding, and multiple access designs for wireless information-power transmission," *IEEE Transactions on Communications*, vol. 68, no. 11, pp. 6822–6839, Nov. 2020.

[111] C. Liaskos, S. Nie, A. Tsioliaridou, A. Pitsillides, S. Ioannidis, and I. Akyildiz, "Realizing wireless communication through software-defined hypersurface environments," in *2018 IEEE 19th International Symposium on "A World of Wireless, Mobile and Multimedia Networks" (WoWMoM)*. IEEE, Jun. 2018, pp. 14–15.

[112] Q. Wu and R. Zhang, "Beamforming optimization for intelligent reflecting surface with discrete phase shifts," in *ICASSP 2019 - 2019 IEEE International Conference on Acoustics, Speech and Signal Processing (ICASSP)*. IEEE, May 2019, pp. 7830–7833.

[113] Q.-U.-A. Nadeem, A. Kammoun, A. Chaaban, M. Debbah, and M.-S. Alouini, "Intelligent reflecting surface assisted wireless communication: Modeling and channel estimation," *arXiv:1906.02360*, pp. 1–7, Jun. 2019.

[114] C. You, B. Zheng, and R. Zhang, "Intelligent reflecting surface with discrete phase shifts: Channel estimation and passive beamforming." IEEE, Jun 2020, pp. 1–6.

[115] J.-M. Kang, "Intelligent reflecting surface: Joint optimal training sequence and refection pattern," *IEEE Communications Letters*, vol. 24, no. 8, pp. 1784–1788, Aug. 2020.

[116] P. Wang, J. Fang, H. Duan, and H. Li, "Compressed channel estimation for intelligent reflecting surface-assisted millimeter wave systems," *IEEE Signal Processing Letters*, vol. 27, pp. 905–909, 2020.

[117] Q. Wu and R. Zhang, "Weighted sum power maximization for intelligent reflecting surface aided SWIPT," *IEEE Wireless Communications Letters*, vol. 9, no. 5, pp. 586–590, May 2020.

[118] Y. Tang, G. Ma, H. Xie, J. Xu, and X. Han, "Joint transmit and reflective beamforming design for IRS-assisted multiuser MISO SWIPT systems," in *ICC 2020 - 2020 IEEE International Conference on Communications (ICC)*. IEEE, Jun. 2020, pp. 1–6.

[119] Q. Wu and R. Zhang, "Joint active and passive beamforming optimization for intelligent reflecting surface assisted SWIPT under QoS constraints," *IEEE Journal on Selected Areas in Communications*, vol. 38, no. 8, pp. 1735–1748, Aug. 2020.

[120] D. Xu, X. Yu, V. Jamali, D. W. K. Ng, and R. Schober, "Resource allocation for large IRS-assisted SWIPT systems with non-linear energy harvesting model," in *2021 IEEE Wireless Communications and Networking Conference (WCNC)*. IEEE, Mar. 2021, pp. 1–7.

[121] T. Adali and S. Haykin, Eds., *Adaptive Signal Processing: Next Generation Solutions*. Hoboken, NJ, USA: Wiley, Mar. 2010.

[122] G. H. Golub and C. F. Van Loan, *Matrix Computations*. Baltimore, MD, USA: Johns Hopkins University Press, 2013.

[123] Z.-q. Luo, W.-k. Ma, A. So, Y. Ye, and S. Zhang, "Semidefinite relaxation of quadratic optimization problems," *IEEE Signal Processing Magazine*, vol. 27, no. 3, pp. 20–34, May 2010.

[124] M. Grant, S. Boyd, and Y. Ye, "CVX: MATLAB software for disciplined convex programming," 2016.

[125] S. Boyd, S.-J. Kim, L. Vandenberghe, and A. Hassibi, "A tutorial on geometric programming," *Optimization and Engineering*, vol. 8, no. 1, pp. 67–127, May 2007.

[126] M. Chiang, *Geometric Programming for Communication Systems*. Boston, MA: Now, 2005.

[127] D. Tse and P. Viswanath, *Fundamentals of Wireless Communication*. Cambridge University Press, May 2005.

[128] B. Clerckx and C. Oestges, *MIMO Wireless Networks: Channels, Techniques and Standards for Multi-Antenna, Multi-User and Multi-Cell Systems*. Elsevier Science, 2013.

[129] L. Grippo and M. Sciandrone, "On the convergence of the block nonlinear gauss-seidel method under convex constraints," *Operations Research Letters*, vol. 26, no. 3, pp. 127–136, Apr. 2000.

[130] V. Erceg, L. Schumacher, P. Kyritsi, A. Molisch, D. S. Baum, A. Y. Gorokhov, C. Oestges, Q. Li, K. Yu, N. Tal, B. Dijkstra, A. Jagannatham, C. Lanzl, V. J. Rhodes, J. Medbo, D. Michelson, M. Webster, E. Jacobsen, D. Cheung, C. Prettie, M. Ho, S. Howard, B. Bjerke, L. Jengx, H. Sampath, S. Catreux, S. Valle, A. Poloni, A. Forenza, and R. W. Heath, "IEEE P802.11 wireless LANs TGn channel models," *IEEE 802.11-03/940r4*, 2004.

[131] S. Li, K. Yang, M. Zhou, J. Wu, L. Song, Y. Li, and H. Li, "Full-duplex amplify-and-forward relaying: Power and location optimization," *IEEE Transactions on Vehicular Technology*, vol. 66, no. 9, pp. 8458–8468, Sep. 2017.

[132] W. Tang, M. Z. Chen, X. Chen, J. Y. Dai, Y. Han, M. Di Renzo, Y. Zeng, S. Jin, Q. Cheng, and T. J. Cui, "Wireless communications with reconfigurable intelligent surface: Path loss modeling and experimental measurement," *IEEE Transactions on Wireless Communications*, vol. 20, no. 1, pp. 421–439, Jan. 2021.

[133] Q. Wu and R. Zhang, "Beamforming optimization for wireless network aided by intelligent reflecting surface with discrete phase shifts," *IEEE Transactions on Communications*, vol. 68, no. 3, pp. 1838–1851, Mar. 2020.

[134] S. Boyd and L. Vandenberghe, *Convex Optimization*. Cambridge University Press, Mar 2004.

[135] D. Xu, X. Yu, Y. Sun, D. W. K. Ng, and R. Schober, "Resource allocation for IRS-assisted full-duplex cognitive radio systems," *IEEE Transactions on Communications*, vol. 68, no. 12, pp. 7376–7394, Dec. 2020.

[136] B. R. Marks and G. P. Wright, "A general inner approximation algorithm for nonconvex mathematical programs," *Operations Research*, vol. 26, no. 4, pp. 681–683, Aug. 1978.

[137] W.-C. Li, T.-H. Chang, C. Lin, and C.-Y. Chi, "Coordinated beamforming for multiuser MISO interference channel under rate outage constraints," *IEEE Transactions on Signal Processing*, vol. 61, no. 5, pp. 1087–1103, Mar. 2013.